Extraction and Analysis of Nuclear Fuel Fragments from the Chernobyl Exclusion Zone

---

Von der Fakultät für Mathematik und Physik

der Gottfried Wilhelm Leibniz Universität Hannover

---

zur Erlangung des Grades
Doktor der Naturwissenschaften
- Dr. rer. nat. -

genehmigte Dissertation von
M. Sc. Martin Weiß

2022

Referent:	Prof. Dr. Clemens Walther
Koreferent:	Prof. Dr. Georg Steinhauser
Koreferent:	Prof. Dr. Gareth Law
Tag der Promotion:	22. April 2022

Abstract

To this day, the radioactive fallout from the Chernobyl Nuclear Power Plant accident contaminates the Chernobyl Exclusion Zone (CEZ) in the form of spent fuel fragments, so called *hot particles*. For precise prediction of particle leaching and subsequent mobilization of radio-ecologically relevant radionuclides, such as U, Pu, ^{137}Cs, ^{90}Sr or ^{241}Am, in-depth knowledge about these particle's nature needs to be gathered.

This work consists of several parts. First, methods for particle separation from soil and sediment samples are tested and developed into an optimized routine sequence, which is then used to identify a number of hot particles.

In the following step, a Scanning Electron Microscopy (SEM)-based micromanipulation technique is applied to image and extract single micron-sized particles. Individual specimen are glued to fine tungsten needles for easier and safer handling. Using such separately mounted particles, a range of non-destructive analytical techniques is applied to achieve a wide set of data for each particle. These techniques include SEM imaging and Energy Dispersive X-ray Spectroscopy (EDS) analysis and γ spectrometry for quantification of ^{137}Cs, ^{241}Am and ^{154}Eu in single particles. To analyze isotopic ratios with lateral resolution, static Time Of Flight Secondary Ion Mass Spectrometry (TOF-SIMS) is applied, which can also be used to image the isotope distribution on a particle's surface. General feasibility and capability of resonant Laser-Secondary Neutral Mass Spectrometry (SNMS) analysis on individual particles is demonstrated.

To investigate uranium speciation non-destructively within the samples, three particles were analyzed at the Swiss Light Source (SLS) beamline at the Paul Scherrer Institut (PSI) in Switzerland. Here, μ-focus X-ray Fluorescence (μ-XRF), μ-focus X-ray Absorption Near Edge Spectroscopy (μ-XANES) and finally μ-focus X-ray Diffraction (μ-XRD) were applied to yield extensive data about oxidation states of uranium and the internal structure of the particles.

Finally, an incremental dissolution sequence was tested for feasibility. A single tungsten needle-mounted particle was subsequently exposed to increasingly aggressive acidic leaching steps. After each step, the leaching progress was monitored by measuring the leachant with γ spectrometry and Inductively Coupled Plasma Mass Spectrometry (ICP-MS) for ^{137}Cs and plutonium quantification as well as particle SEM imaging after each step.

Keywords: Hot Particles, Chernobyl, particle analysis

Declaration of Authenticity

I hereby declare...

1. ... to comply with the applicable rules of the common regulations for the doctorate Doctor of natural sciences (Dr. rer. nat.) at the Gottfried Wilhelm Leibniz University of Hanover and to have complied with them, as well as to agree to an examination according to the regulations of the to be in agreement with the doctoral regulations,

2. ... that the present dissertation was written by me independently, whereby no sections of text from third parties or my own examination papers have been taken over without citation. All used aids and sources were indicated in the thesis,

3. ... that this work has not been acquired or procured in whole or in part from third parties in return for payment or other compensation,

4. ... that this dissertation has not been submitted for another examination,

5. ... that neither the same nor substantially similar work has been submitted elsewhere as a dissertation to another faculty or university,

6. ... to agree that this dissertation will be subjected to a review of compliance with generally accepted scientific standards.

Martin Weiß

Contents

Lists   **117**

Bibliography   **125**

A   Acknowledgments / Danksagung   **135**

B   Appendix   **137**

1 Introduction

1.1 The Chernobyl Nuclear Power Plant Accident

As the most catastrophic nuclear accident to this point, "Chernobyl" is the basis and motivation for this work. The entire course of events is well documented in literature, from the reactor explosion to the following open-air graphite fire.[IAEA 1992][Adamov et al. 1996][Smith et al. 2005] During these events, large amounts of radionuclides were expelled into the environment, several times more than during the 2011 Fukushima accident.[Steinhauser et al. 2014] A significant part of the nuclear fuel inventory from the reactor core was ejected into the surrounding environment,[deCort 1998] a part of which was in the form of particles.[Bogatov et al. 1990][Kashparov et al. 2003] Very fast disintegration due to weathering in the environment has been predicted,[Konoplev et al. 2000] however to this day particles can be found in soil and litter samples.[Hamann 2017] To investigate the effects of radionuclide exposure on fauna, flora and especially health and safety of people,[UNSCEAR 2000] the fate of radionuclides and especially particles in the environment needs to be analyzed in detail. Results from these investigations can yield valuable lessons for potential future accidents.[Balonov 2013]

1.2 Hot Particle Background

The Chernobyl accident is not the only source of hot particles in the environment.[Salbu 2009] Other sources are for example accidents with nuclear weapons,[Lind et al. 2007] nuclear weapons testing[Cook et al. 2021] or the use of uranium-based ammunition.[Danesi et al. 2003][IAEA 2011]
The nuclear fuel-based particles this work concentrates on are made up mostly of enriched uranium in various states of burnup. They can be distinguished from naturally occurring uranium for example by analyzing their isotope signature, as their ^{235}U concentration is higher than natural.[Boulyga et al. 2008] Much more relevant and obvious to detect however is the content of plutonium and many other minor actinides and fission products. Hot Particles therefore have much higher specific activities when compared with natural uranium minerals. After being deposited in the environment, such particles are exposed to natural weathering effects, like rain, air, microbial activity and pH or redox condition changes. These conditions over

time will lead to mobilization of the radionuclides contained within. Mobilization can take several pathways, for example leaching of individual radionuclides like ^{137}Csor disintegration of the entire particle structure. The exact chemical behavior of any single particle is strongly dependent on these external factors as well as the speciation of uranium and the minor components of the particle.[Batuk et al. 2015] In the case of Chernobyl, three main particle types have been described:[Kashparov et al. 2003][Kashparov et al. 2012]

- **relatively reduced particles:** Composed mostly of a UO_2 matrix, being chemically relatively stable[Salbu et al. 2001]
- **relatively oxidized particles:** A uranium oxide matrix containing higher oxygen ($UO_{[2+x]}$) which are chemically unstable[Kashparov et al. 1996]
- **stable particles:** Particles that formed during the reactor core meltdown and annealed with the zirconium cladding material.[Bugai et al. 2002] Due to the zirconium oxide content, these particles are chemically extraordinary stable

1.3 Motivation for this Work

The prediction of radionuclide mobilization from spent nuclear fuel is a highly complex challenge due to the many influence factors. To understand the environmental behavior of individual particles, it is not sufficient to gather data about its radionuclide inventory, its uranium isotope ratio and speciation or its morphology. Ideally, all these factors are analyzed and gathered in a database like the one published by ZHURBA ET AL..[Zhurba et al. 2009] Often such analysis is performed on more macroscopic fuel samples and by destructive methods, for example dissolution and subsequent α spectrometry, γ spectrometry and mass spectrometric analysis.[Makarova et al. 2008][Veliscek-Carolan 2016] The drawback of such methods is the loss of all information on morphology and speciation after dissolution. A different approach is speciation selective, subsequent dissolution, mostly of bulk sample material.[Kashparov et al. 2019] This way however, resulting data are averaged over a range of different particles, whereby individual speciation information is lost.

Separation and analysis of individual particles of interest generally is not a new idea and different approaches have been published before. Particles were extracted by radiometric selection and ashing of air filters[Boulyga et al. 1997]. Other techniques used radiometric selection in combination with flotation in heavy liquids to separate particles from soil samples[Burakov et al.] and mounting in acrylic blocks[Pöml et al. 2017]. A similar process of particle extraction with a micromanipulator and tungsten needles has been described[Esaka et al. 2007] and a comprehensive summary of search and extraction techniques has been given by the IAEA[IAEA 2011]. Such processes however are rarely used to analyze *individual* particles. Hence, the aim of this work is the development, testing and optimization of a sequence of nondestructive techniques and methods to analyze all of the mentioned characteristics for individual, separated particles from Chernobyl environmental samples. To achieve this, first a reliable method of finding and extracting individual particles from environmental samples is developed. It starts with α Track Detection (ATD) for particle localization, followed by imaging in optical and electron microscopes and finally particle extraction via micromanipulation. For speciation of uranium and plutonium, beamline methods are tested and γ spectrometry is used to quantify individual radionuclides within a single particle. Eventually a method for subsequent dissolution of an individually extracted particle is tested for its feasibility to analyze individual radionuclide leaching behavior in increasingly aggressive solvents.

2 Background: Methods and Instruments

A variety of analytical techniques and methods has been used during this work. This chapter will give a short overview of the basics of each method and instrument. Details about the instruments, materials and chemicals used within this work can be found in the respective section *List of Instruments and Materials*.

Among the described methods are ATD, which was used mainly for the location of α-emitting particles. Scanning Electron Microscopy (SEM) was used for particle imaging and extraction, and additionally to identify uranium or zirconium content in particles using the equipped Energy Dispersive X-ray Spectroscopy (EDS) detector. For further analysis, Secondary Ion Mass Spectrometry (SIMS) was briefly used, its variant Secondary Neutral Mass Spectrometry (SNMS) is also introduced. For radionuclide quantification, γ-spectrometry was used and several X-ray Absorption Spectroscopy (XAS) techniques yielded speciation data about individual particles.

2.1 α Track Detection

ATD is used to measure α activity and works by tracking the traces of mechanical damage, that α particles cause in a smooth plastic surface. Because it visualizes only mechanical damage, the technique is impervious to β or γ radiation.[Mi-Net Technology Ltd].

The detector material used in this work, is CR-39 (poly allyl diglycol carbonate), a transparent polymer used in the form of sheets of about 1 mm thickness. When this material is exposed to sources of α radiation, such as radon in the air, surface deposited α emitters or spent nuclear fuel particles, α particles can penetrate the polymer's surface and leave a trail of damaged material. The size of this trail is in the range of nm, with its exact size dependent on the α radiation energy. To render such trails visible, the detector is etched with concentrated NaOH at elevated temperatures. Damaged material is etched more effectively than the intact polymer, increasing the size of the trails depending on NaOH concentration, temperature and etching time. The resulting α tracks can then be evaluated by optical microscopy.

A general experimental process in ATD is as follows:

1. (Optional): Short etching of detector for background reduction

2. Exposure of detector to α radiation from the air, a surface, a particle, ...

3. Detector etching (depending on detector material) to render damaged areas visible

4. Evaluation of visible spots by optical microscopy. Automated scanning and track counting is possible for dose estimations

Figure 2.1 shows a sketch of the detection principle. The small area of initial incident is shown in light gray around the α ray. The larger visible area after etching is indicated as a white dotted line. The actual shape of the α track is dependent on incident angle and etching time, and can vary from a drop-like form to a featureless sphere.[Bondarenko et al. 1996],[Fleischer et al. 1980]
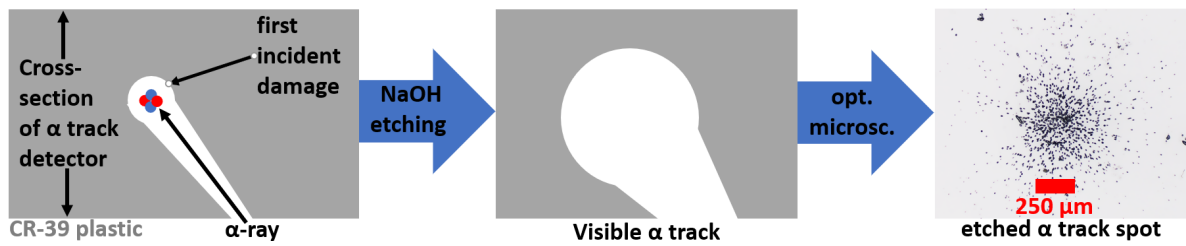
Fig. 2.1   Illustration of the α track detection basic principle:
**0.** (Optional) Short etching of detector for background reduction.
1. Exposure of detector to α radiation from the air, a surface, a particle, ... leads to first incident damage in the detector material.
2. Detector etching to enlarge α track damage and enhance visibility.
3. Evaluation of visible spots by optical microscopy. Manual or automated scanning and track counting for dose estimations.

2.2 **γ-Spectrometry**

γ-Spectrometry is a method to measure γ-radiation both qualitatively and quantitatively. In contrast to basic measuring activity with a Geiger counter for example, γ-Spectrometry yields spectra which draw a counted intensity against a calibrated energy. This allows differentiation between distinct and specific γ-energy lines and hence the identification of one or more γ-emitting radionuclides. Provided a reproducible geometry and adequate calibration, the measured intensities can be used to quantify each γ-emitting radionuclide present in the sample. A strong advantage of this technique is that a basic qualitative measurement needs little to no sample preparation. It was rarely used during this work, which is why the theoretical background is described only briefly.

A source of γ-radiation is the β-decay of radionuclides like ^{137}Cs into meta-stable daughters like ^{137m}Ba. Such nuclides then release their excitation energy by emitting γ-photons. Figure 2.2 shows a decay scheme for ^{137}Cs as a prominent example.
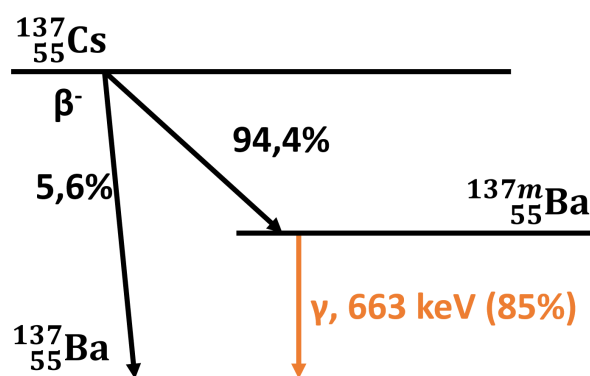
Fig. 2.2   The decay process of ^{137}Cs:
A short decay scheme to display the source of γ radiation, with ^{137}Cs as a relevant example. Only 5.6 % of the ^{137}Cs decays directly to ^{137}Ba whilst 94.4 % decay to the excited state ^{137m}Ba, which again undergoes a relaxation process and releases its excess energy via several γ lines. The most prominent one - and the one mostly used for ^{137}Cs quantification - is the one at 663 keV. All values taken from the Karlsruher Nuclide Chart.[Nucleonica GmbH 2017]

Such γ photons can then be detected by a suitable detector. To achieve high energy resolution and sensitivity, High Purity (HP)-Ge detectors are commonly used in combination with sufficient shielding by lead for background suppression. Radionuclide quantification requires precise energy and efficiency calibration, using reference materials that match the sample's geometry as well as its matrix for highest accuracy.[Knoll 2000]

2.3 Electron Microscopy

The term *electron microscopy* summarizes an array of techniques, which involve imaging based on a continuously focused electron beam in varying degrees of vacuum quality. For this work, only Scanning Electron Microscopy (SEM) and its variation Environmental Scanning Electron Microscopy (ESEM) are of relevance.

The main component of an SEM is the electron gun. Several types of electron sources are possible, for example field emission guns or the LaB_6-type cathode. Most common is the tungsten filament cathode, which was used in this work. To create the focused electron beam, the W filament is heated in vacuum ($p < 10^{-4}$ mbar). The emitted electrons are accelerated and focused by a WEHNELT cap, followed by a column of lenses and apertures. The setup is illustrated in figure 2.3.
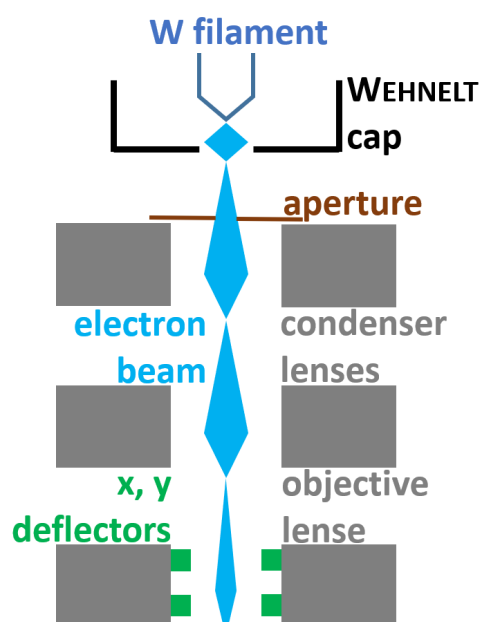
Fig. 2.3 Schematic of the SEM beam gun and focusing column:
The electron beam, depicted in blue, is created and accelerated within a WEHNELT setup and focused through a number of lenses and apertures. At the lower end of the SEM column, deflectors divert the beam in two dimensions to scan the beam spot over the sample surface. The spot size is the major contributor to imaging resolution and itself is greatly dependent on the acceleration voltage (usually 0.2 kV to 30 kV) and settings for the apertures.

Imaging is usually done with electron beam energies between 0.2 keV and 30 keV. Given a precise tuning of the apertures, beam spot sizes of less than 1 nm are achieved on the sample surface. Under normal conditions, the process is fully non-destructive, which made the technique especially valuable for this project.

Several kinds of interactions between primary electron beam and sample can be measured

and, because the primary electron beam is scanned over the surface, composed into images. Based on their individual physical effects, different signals (beam - matter interactions) yield varying types of information in addition to imaging. Each type of signal requires special detectors with a specific geometric arrangement. A basic detector setup within a SEM is shown in figure 2.4. Each detector and its specific use is described in the following individual subsections. This list only includes methods used within this thesis.
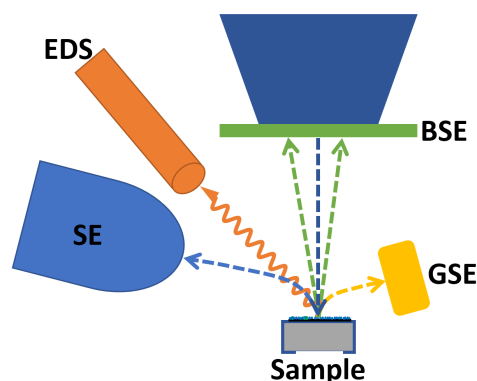
Fig. 2.4   A schematic of the SEM internal setup of detectors and their respective signals:
Different kinds of electron beam - sample interaction generate different kinds of signal that require individual detector setups for analysis:
SE and GSE: Both measure Secondary Electrons (SEs), which leave the sample surface with low energy in the eV range. Both detectors are located in an angle relative to the electron beam.
BSE: Backscattered Electrons (BSEs) leave the surface with close to their initial energy typically at an angle of around 180°. Its corresponding detector is therefore placed in a (segmented) ring around the bottom of the column.
EDS: The Energy Dispersive X-ray Spectroscopy (EDS) detector measures characteristic X-rays emitted by recombination after secondary electron generation. It can be used to identify main elements within the sample and also to create compositional mappings of the surface.

Vacuum and Charge Compensation   One important factor in electron microscopy is the vacuum applied in the sample chamber. The primary electron beam can only be created in High Vacuum (HV) ($p < 1.4 \times 10^{-4}$ mbar for this instrument), and analytes therefore have to be vacuum compatible. Additionally, some kind of charge compensation has to be applied to avoid charge buildup which in turn would disturb primary electrons and Secondary Electrons (SEs) and could damage the sample. For electrically conductive samples, the surface charge is simply channeled off and does not pose any interference with the measurement. If one intended to analyze insulating samples however - for example uranium oxide particles - charge buildup has to be avoided. A way to increase surface conductivity would be to coat samples with a conductive material, for example C or Au. When this is not an option, an ESEM can be used. In such a setup, only the column for primary electron beam generation is in HV, whilst the analytical chamber is kept at Low Vacuum (LV) of 0.1 mbar to 1 mbar. The residual atmosphere then compensates for local charge buildup, but also absorbs part of the SEs, which is why a Gaseous Secondary Electron (GSE) detector has to be used.

2.3.1 SE and GSE

When an electron that is part of the electronic shell of an atom is hit by another electron with an energy higher than its own binding energy, it can leave its position with some residual kinetic energy. In the case of electron microscopy, the incoming electron originates from the primary electron beam and the previously bound one is a Secondary Electron (SE). The primary electrons only transfer a part of their initial energy, and therefore SEs leave their atoms with only some eV of energy. Because of this low energy, they are easily absorbed in surrounding material and can only be detected when their energy is sufficient to leave the sample surface. SE signal depth is only in the nm range, as shown in figure 2.5, and is mostly used for surface imaging. Local signal intensity is dependent on a range of factors: emitting material, individual bonding energies and a number of contrast mechanisms. For the EVERHART-THORNLEY-detector setup used in this work, the main contrast mechanism is the sample topography. As it is positioned sideways of the sample surface, areas that are angled towards the detector seem brighter than others. The SE contrast is mostly used to create surface images with high spatial resolution.

When using the LV mode of the SEM, the standard SE detector is positioned too far away from the sample, so that the SEs cannot reach the detector through the gaseous atmosphere. Hence, the signal is heavily dampened. To compensate for SE absorption in LV mode, a Gaseous Secondary Electron (GSE) detector is installed closer to the sample. In contrast to the normal SE detector, the GSE is not an EVERHART-THORNLEY-setup, more prone to noise background and because of its positioning also sensitive to BSE background. Its imaging quality is therefore inferior to SE in HV mode.

2.3.2 BSE

Primary electrons entering solid sample material are generally scattered into all directions by interaction with the sample atoms. In some cases they are scattered in angles around 180°, sending them back out of the sample surface. Such Backscattered Electrons (BSEs) have kinetic energies in the keV range, much higher than SEs, giving them enough velocity to pass the attracting field of the SE detector without being diverted. A scintillation or semiconductor detector in the shape of a (sometimes segmented) ring around the primary electron beam can therefore be used to selectively analyze these BSEs. Their signal strength still depends on surface topography, but even more so on the sample material: Elements with higher electron density (here often referred to as heavy elements) in the atom shell have increased chances of generating BSEs than those with lower electron density, creating a material contrast.

Because of their higher energy, BSEs can leave the sample from greater depths than SEs (in the µm range) and, based on scattering effects, also from an area larger than the original beam

diameter. Hence the BSE contrast does not usually reach the high resolution of the SE contrast. The affected volume is utilized in figure 2.5, which shows an excitation bulb for the primary electron beam. The shape is typical, the actual size of the bulb however is strongly dependent on the sample material and the acceleration voltage of the primary electron beam.

Combination Contrasts: Since SE and BSE can be measured simultaneously, both signals can be combined in an additive or subtractive manner, to create special combinations of contrasts. Subtracting the BSE image from the SE image can be used as background correction, since a small portion of BSEs are scattered directly into the SE detector and increase the imaging depth. An image corrected in that way (SE-BSE) gives a strong *surface contrast*. An additive combination of both images (SE + BSE) yields enhanced contrast and can combine strong material contrasts (for example for uranium oxide particles) with higher resolution imaging.
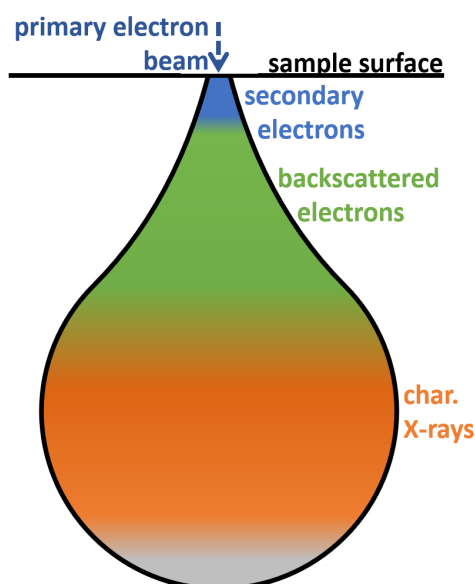
Fig. 2.5   The SEM excitation bulb displaying signal depths:
Depending on their initial energy, primary electrons can penetrate the sample surface into a depth of up to several µm. Due to scattering interactions with the solid material, the focus point of the beam is in the first atom layers and the beam widens with increasing penetration depth. The volume of primary-electron-interaction is called an *excitation bulb*, which can be used to display the area of effect for the different SEM signals. The actual size of the excitation bulb is dependent on the material and especially on the primary electron energy.

2.3.3 EDS

A secondary effect of the generation of SEs is the creation of an *electron hole* within the atomic shell the SE originated from. A higher energy electron from the same atom shell can then fill this hole, thereby relaxing into a lower energy state. The resulting emitted X-ray photon has

an energy equivalent to the energy gap of the two involved states. The process is shown in figure 2.6.

(a) Electron hole creation

(b) Recombination
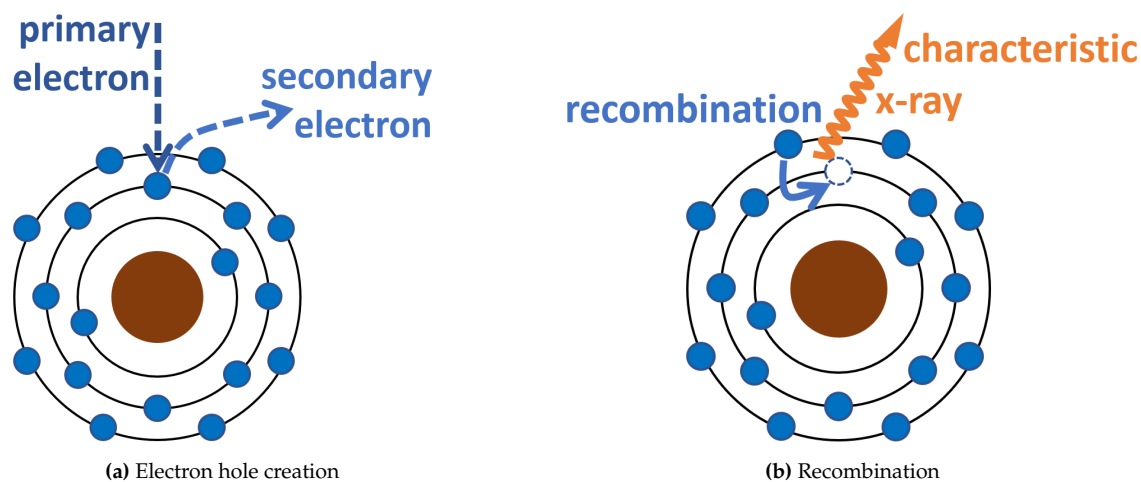
Fig. 2.6   Schematic of the source of characteristic X-rays in a SEM:
(a) A primary electron with sufficient energy can hit a secondary electron out of its place within an atom shell, creating a gap.
(b) An electron from a higher atom shell can drop down to fill the gap left by the secondary electron. The energy difference leaves the atom as a characteristic X-ray photon.

The energies of emitted photons correspond to the discrete energy levels in the atom shell and hence can be used to identify the underlying elements, for example with an Energy Dispersive X-ray Spectroscopy (EDS) detector. Depending on the excitation energy (e.g. the energy of the primary electron), several electron shell transitions can be detected as patterns, which is especially useful in the case of overlapping signals due to the limited energy resolution of the detector. This can, however, also lead to an overlap of major and minor component's signals. Due to this effect, it is not possible to detect Pu in the particles analyzed here.

Figure 2.7 illustrates the origin of several emission lines and the respective naming scheme. Emission line designations consist of the shell that the excited electron emerged from (K, L, M, ...) and usually an α or β as suffix, depending on the relaxing electron transition. For example, an electron hole in the L shell being filled by an electron from one shell higher leads to the emission of a $L\alpha$ line. A $K\beta$ line is the result of an electron hole in the K shell being filled by an electron from the M shell.
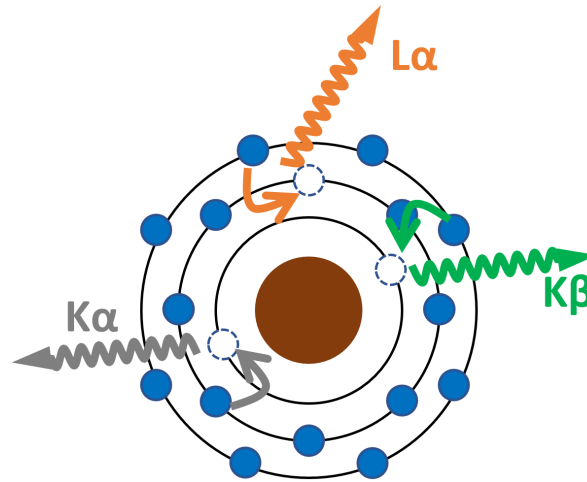
Fig. 2.7   Schematic illustration of different x-ray emission lines' origin:
The emission lines' naming scheme depends on the electron transition. In an EDS spectrum, several lines can be visible and the patterns are characteristic for each element.

The EDS method can reliably be used to identify main components of samples, however it is not sensitive enough to detect trace elements, for example fission products within a spent fuel uranium matrix.

2.3.4 Micromanipulator

In order to separate individual particles from the sample matrix, a micromanipulator was used with the SEM. It essentially is a robotic arm, compatible with various tools, that is built into the SEM vacuum chamber and around the sample stage. It is controlled either by software or a remote control. Figure 2.8 shows a photo taken of the micromanipulator before setup within the vacuum chamber, equipped with a specialized adapter and a fine tungsten needle.
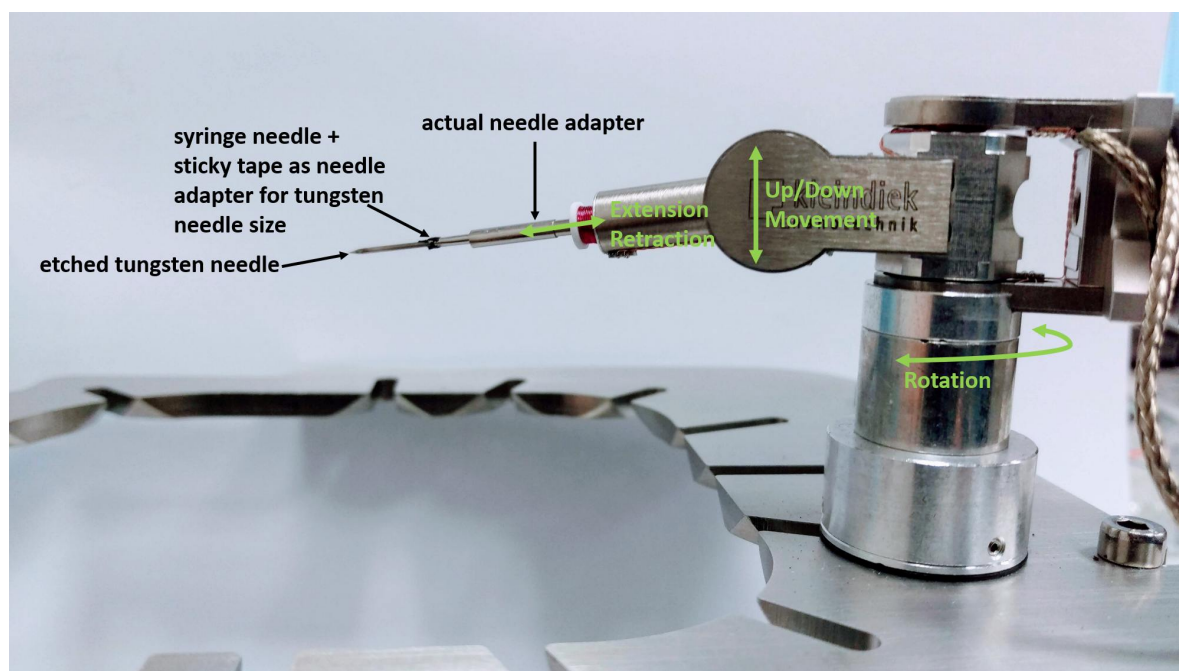
Fig. 2.8   Photo of the micromanipulator:
A photo taken of the micromanipulator (*MM3A-EM* by *Kleindiek Nanotechnik GmbH*) before setting it up inside the SEM. The manipulator itself can rotate horizontally, lift and lower vertically as well as extend and retract the tip. Originally, the manipulator came with several different sized adapters for needles. However, since custom made needles etched from tungsten wire were used in this work, a workaround involving sticky tape and a syringe needle was crafted to adapt for needle diameters.

For this work, only tungsten needles in combination with a vacuum compatible glue (*SEMglu*™) were used as tools. Using the micromanipulator, a needle tip can be moved with nm precision within the SEM during live imaging. The needle is mounted at a fixed height, but can be moved around in three dimensions.

The *SEMglu* stays liquid (although highly viscous) during manipulation with a needle and withstands the low-focused electron beam. When focusing the beam and adjusting the apertures to increase the beam current to a maximum however, the glue quickly cures within minutes.

For W needles, commercial products can be used, which usually consist of an extremely

fine tungsten wire mounted onto a thicker rod of another metal. Such products reach tip diameters in the nm range and can be used to interact with accordingly small structures. Another option is to use chemical etching to create needles out of a tungsten wire. This has been successfully done within an affiliated B.Sc. thesis and the resulting needles were mostly larger in diameter compared to the commercial ones, but at the same time more mechanically stable.[Hanemann 2019]

2.4 SIMS

Time-Of-Flight (TOF) Secondary Ion Mass Spectrometry (SIMS) is a specialized method for solid surface mass spectrometry, that allows the analysis of solid samples without special pre-treatment and leaves the sample mostly intact after measurements. It is comprised of an ionization system, that uses a Liquid Metal Ion Gun (LMIG) to accelerate a pulsed Primary Ion (PI) beam (here: bismuth in packages) onto the samples surface in Ultra High Vacuum (UHV). PIs impacting the sample disrupt the surface and sputter atoms as well as intact molecules out into the vacuum. A small percentage of the sputtered material is ionized in the process. Secondary Ions (SIs) generated this way are attracted by electric fields of the extractor and accelerated into a TOF mass analyzer. The process is illustrated in figure 2.9
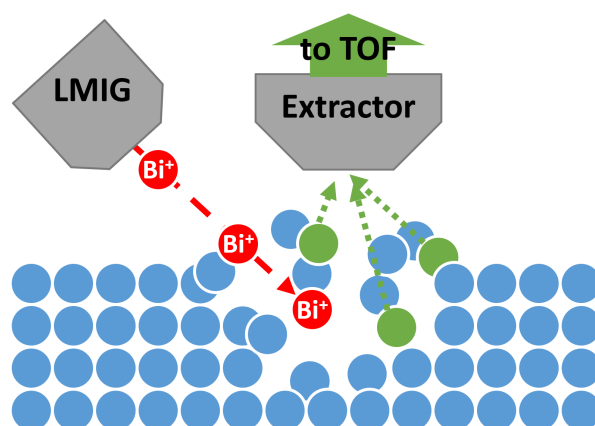
Fig. 2.9 **The ionization process of SIMS:**
The pulsed LMIG accelerates bursts of Bi^+-ions into a sample (here displayed in blue), disrupting the surface and sputtering material into the vacuum. Such Secondary Ions (SIs) are accelerated by the extractor via electric fields and inserted into the TOF mass analyzer. Because the PI beam is pulsed instead of continuous, the method is considered *quasi-non-destructive*.

The main difference between *static* SIMS and *dynamic* SIMS is the pulsed PI beam. The PI beam is only active during a small fraction of the actual measurement time, hence the sputtering of material is kept to a minimum, affecting only the topmost atom layers of the sample surface. An advantage of this method compared to dynamic SIMS techniques with continuous ion

beams is, that it is almost non-destructive and leaves the sample intact for further experiments. However, this also leaves the technique sensitive to surface contamination, for example by adsorbed air molecules or plasticizer from sample storage in plastic containers. Since the method is so close to being non-invasive, actual sample signal can be blocked by even few nm of contaminants. Solutions to such problems are either extended measurement times or the use of additional sputter guns.

Another specialty of the SIMS technique is the PI beam scanning over the surface, thus mapping two-dimensional areas whilst creating full mass spectra per individual sputter spot, e.g. pixel. This allows imaging similar to EDS mapping, although instead of elements, maps based on analyte mass-to-charge ratio m/z can be created.

2.5 SNMS

The Secondary Neutral Mass Spectrometry (SNMS), or resonant laser-SNMS is a variation of the described TOF-SIMS. It uses the same sputtering process and analytical array, but instead of analyzing the SIs created initially by the PI beam, these are suppressed by electric fields, pushing them back onto the sample or into the vacuum. This only affects ionized species, leaving all sputtered neutral atoms and molecules as an expanding cloud. In resonant laser-SNMS, another ionization process now substitutes the ion beam ionization:

A combination of two to three laser beams is focused into the expanding cloud of sputtered neutral species. Each individual laser is tuned to an atom resonance of the target element, that corresponds to a single step within a multi-step excitation ladder of a specific element. With all lasers crossing the cloud of neutrals simultaneously, atoms of the element to which the excitation ladder corresponds are selectively ionized, leaving most of the sputtered material in a neutral state. The analyzer is then activated and only the ionized species are taken into the mass spectrometer.

The advantage of this method is the combination of a *mass-selective analysis* (TOF mass spectrometry) with an *element-selective ionization* technique. This allows a pre-selection of an element to analyze and suppresses background signal including isobaric interferences by several orders of magnitude.[Franzmann et al. 2018] This ideally results in suppression of isobaric interferences and hence in the possibility to measure for example ^{238}Pu besides ^{238}U. Also ^{239}Pu besides ^{238}UH and ^{241}Pu besides ^{241}Am can be measured within the same sample and without previous chemical separation of the isobars - for example on a particle picked out of the Chernobyl Exclusion Zone (CEZ) environment. Additionally, it allows detection and measurement of isotopic ratios even for trace elements like Sr as well as mass-specific mapping, as with the original SIMS technique.[Franzmann et al. 2017][Bosco 2020]
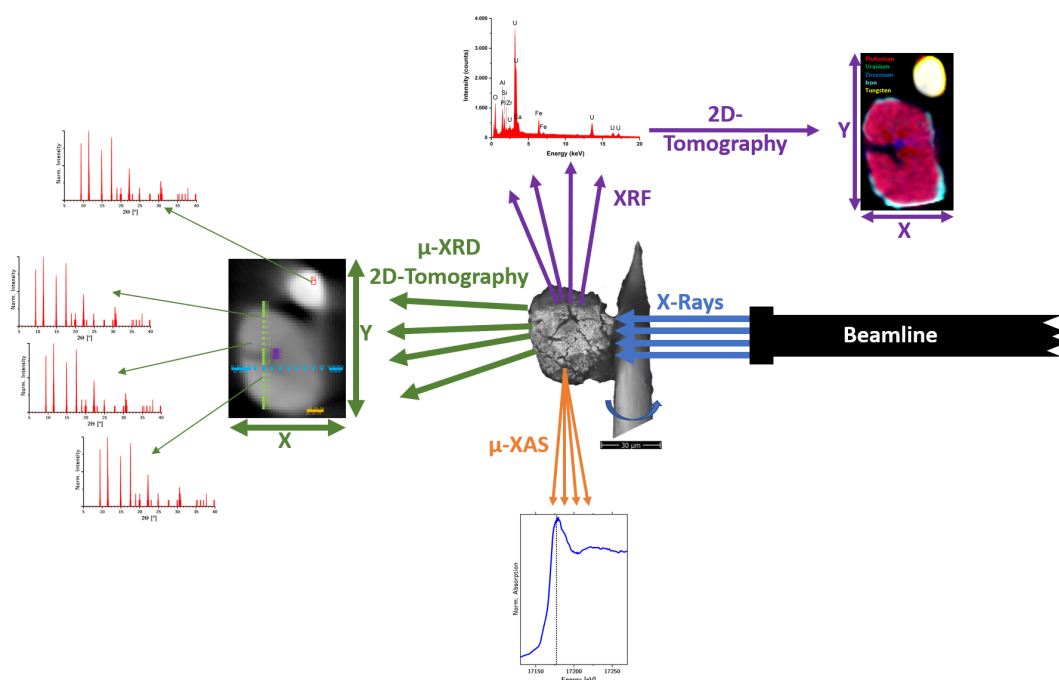
2.6 Beamline Methods

Beamline: Beamlines are specialized laboratories, that are directly connected to a larger synchrotron facility. They utilize the high-brilliance X-ray light emitted from the accelerator ring and refine it for use in a wide variety of experiments, whereby usually individual beamlines are specially built for specific kinds of research. For this work, the μ-XAS beamline of the Swiss Light Source (SLS) at the Paul Scherrer Institut (PSI) in Villigen, Switzerland was used.[PSI 2009]

Motivation for Beamline Analysis: The sum of analytical techniques so far does yield an extensive amount of data whilst leaving the sample intact. These data include the main elemental composition, imaging (SEM, EDS and SIMS/SNMS), mass spectrometry and analyses of several γ emitting radionuclides. One aspect however is still missing: None of the described techniques is capable of analyzing chemical speciation. However, the solubility and mobility of uranium and plutonium is highly dependent on their oxidation states and chemical speciation: The higher oxidized forms are much more soluble and therefore mobile than their respective tetravalent dioxides.

Some widely used techniques for *non-destructive* speciation analysis are X-ray Absorption Spectroscopy (XAS) and X-ray Diffraction (XRD) methods.Yano et al. 2009 For this work, a synchrotron-based beamline with micro-focus equipment was necessary due to the small analyte sizes of max. 50 μm in diameter.

The three beamline-based techniques used for this work were X-ray Fluorescence (XRF) for tomographic imaging, X-ray Absorption Near Edge Spectroscopy (XANES) for the oxidation state identification of U and Pu as well as X-ray Diffraction (XRD) for crystallographic analysis. All methods can be used on the particle without extensive modifications of the experimental setup in between. Figure 2.10 shows an illustration of the setup and their respective results.

Fig. 2.10 Overview of beamline analysis methods:
Whilst the particle and detectors can be moved and turned, the incoming X-ray beam remains constant in direction. Measurements are performed in transmission or fluorescence mode, 2-dimensional tomography is possible for μ-XRD and μ-XAS.

2.6.1 XRF

XRF is based on the same principles that are described in the EDS section. The key difference is the energy source for electron excitation: Whilst the SEM-based EDS uses accelerated electrons, the excitation energy for XRF is introduced by X-rays. Since X-rays have a higher penetration depth into solid matter compared to an electron beam, XRF can be used for tomographic mapping of elements. By using a micro-focus beamline as an energy source, a spatial resolution in the range of single μm can be achieved. Due to the high beam intensity and the lack of background caused by bremsstrahlung, it also allows a lower Limit Of Detection (LOD) for trace elements.

As with EDS, it is unsuitable for speciation analysis, as its signal is only based on the absorbing and fluorescing elements. To measure XRF, a high energy excitation wavelength is chosen and the entire fluorescence spectrum is measured.

2.6.2 XANES

The energy levels of electrons in an atomic shell are discrete and element specific. Since they strongly depend on the interaction between positive core and negative electrons, a change in

oxidation state leads to slight shifts of only a few eV in the K shell of heavy elements. When using a monochromatic beam for excitation, the excitation energy can be scanned for example from −50 eV to 150 eV around the known energy level of an element in question. When the discrete level is reached, absorption (and hence fluorescence) increases rapidly, creating an *absorption edge*. The exact position of this edge and the shape of the curve immediately following it can be used to identify oxidation states for individual elements.[Calvin 2013] Similar to the X-ray emission lines described in the subsection about 2.3.3, these absorption edges are named based on the excited electron shell, though the suffix here is a number dependent on the absorbing electron orbital. For example, the L1-edge designates an excited 2s-electron, whilst L2 and L3 designate excited p-electrons from the L-shell. Figure 2.11 shows XANES spectra of U^{VI} and U^{IV}, measured at the L3-edge of uranium.
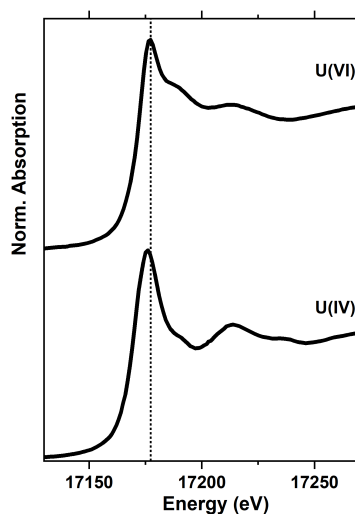
Fig. 2.11   An example for a XANES spectrum:
When the excitation energy is scanned in sub-eV steps, a rapid increase in energy absorption (and hence fluorescence intensity) is observed when the excitation energy reaches the absorption level.
The exact energy of a specific level is strongly dependent on the electronic configuration. Variations for example in the oxidation states hence influence the position and shape of the curve. Differences in oxidation states can vary betwenn single and many eV, which is why a monochromatic and finely tunable source like a beamline is needed for this kind of spectroscopy. The example shown here are the two reference spectra for U(VI) and U(IV) taken from literature[Bower et al. 2019], measured at the U L3 edge.

2.6.3 XRD

X-ray Diffraction (XRD) is a common technique for crystallographic analysis, based on elastic X-ray scattering within the crystal structure of a sample. Standard variations are powder- or single-crystal-XRD, that can be measured in laboratory scale instruments. Single crystal samples have to be turned to illuminate all planes of the crystal structure and to receive a complete *diffraction pattern* for the sample. In general, the reflection intensity based on the incident angle is measured, which in combination with chemical information about the sample can yield data about the sample's crystal structure. When analyzing particles, of known chemical composition (e.g. uranium oxide), crystallographic data obtained by XRD can additionally yield speciation information. Such data however are only obtainable for crystalline structures.

When using a micro-focus beamline as the monochromatic X-ray source, such data can not only be acquired for entire particles, but tomography-based XRD-maps can be created and used to track changes in crystal structure with μm spatial resolution.

3 Particle Search and Extraction

This chapter first describes the origin and initial state of the samples and the sample preparation process. After preparation, the bulk material is narrowed down further to search, isolate and finally extract individual hot particles. Several methods and experiments tested and optimized are presented here.

3.1 Samples

Samples from four different sampling locations around the Chernobyl reactor were analyzed as part of this project. These sampling sites were in the city of Prypjat, the Red Forest[Hamann 2017], the Cooling Pond next to the reactor and an agricultural area called Kopachi. All sampling locations are marked in figure 3.1 and the respective location coordinates are listed in table 3.1. Sample acronyms are mostly based on initial naming and kept here for consistency.

Red Forest (RW):   The Red Forest samples were also used previously by HAMANN[Hamann 2017] and were also collected during that project, together with the Prypjat samples. Initially being litter samples, they were dried and milled before entering the particle search process as outlined within this thesis.

Cooling Pond (CP):   Sediment samples from the Chernobyl Cooling Pond were collected during the BIOVESTRA project as well as the Kopachi samples as part of another thesis[Schulz 2020]. The material consisted of sandy sediment and shells with little organic content.

Kopachi (KOP):   An agricultural field in the area of Kopachi was a central part of another project[Schulz et al. 2019]. A sandy soil with high organic content in the form of roots and litter was received from here.

Prypjat (BK): As part of a previous thesis, an expedition to the Chernobyl exclusion zone analyzed asphalt areas in the city of Prypjat. Two spots of especially high surface activity were probed and taken as drillcores.[Hamann 2017] These were unmodified asphalt cores of ~2.5 cm diameter and only the surface part was analyzed in this work.

Fig. 3.1   The four sampling sites around the Chernobyl Power Plant:
Samples were collected in four different locations and varying distances and directions from the reactor. All four sampling sites - Prypjat, Red Forest, Kopachi and Cooling Pond - are marked and named in the map. The respective location coordinates are listed in table 3.1.

Tab. 3.1   Sampling location coordinates:
The coordinates of the four sampling locations are listed in this table. A graphical presentation is shown in figure 3.1.

Sampling location	Coordinates	Sample
Red Forest (RW)	N51°22′59″, E30°04′42″	Litter (milled)
Cooling Pond (CP)	N51°22′28″, E08°34′39″	Sediment (sand, shells)
Kopachi (KOP)	N51°20′54″, E30°07′41″	Soil
Prypjat (BK)	N51°24′21″, E30°03′29″	Asphalt (drillcore)

3.2 Sample Preparation

Several preparation steps have been utilized over the course of this project. However, the starting point for each new sample was the division of material into several parts to reduce the amount of inactive sample material:

Wet Sieving Since the bulk samples were mostly composed of unrefined sediment or soil, each whole sample was fractionated based on particle size, as the expected particle size was in the micrometer range. The simplest way to separate the smaller fractions from the sample was wet sieving using different mesh sized sieves. All samples were environmental material and exposed to water previously, hence no impact on the particles speciation could be expected from this procedure.

Fig. 3.2 The first step in sample preparation was fractionation for particle size. First, a slurry of sample material in Deionized Water (DI-water) was created to avoid whirling up dust. To break up potential particle agglomerates, the slurry was sonicated in an ultrasonic bath before filling the slurry into the first sieve. Here, four mesh sizes were used: 2000, 650, 200 and 65 µm. All sieves were stacked on top of each other, with a beaker underneath the bottom one to catch the resulting slurry with particle sizes <65 µm.

As illustrated in figure 3.2, the bulk sample was divided into five size fractions. Each fraction was collected individually, dried under a heatlamp (T <105 °C) and the resulting material inspected with a conventional contamination monitor. In the case of CEZ sediment, which was largely composed of sand and shells, all but the smallest fraction of <65 µm showed negligible specific activities. Therefore, only the smallest size fractions were used for the particle search. This was also adapted for other samples, although this result varied slightly for soil and litter samples, where small roots and other organic material showed relatively high specific activities.

Initial vs Final Process Figure 3.3 shows a scheme of the process from sample preparation to SIMS analysis. The forking into a *beginning* and a *final* process is a result of development over the time of this work: The start was based on HAMANNs work[Hamann 2017] and developed from there.
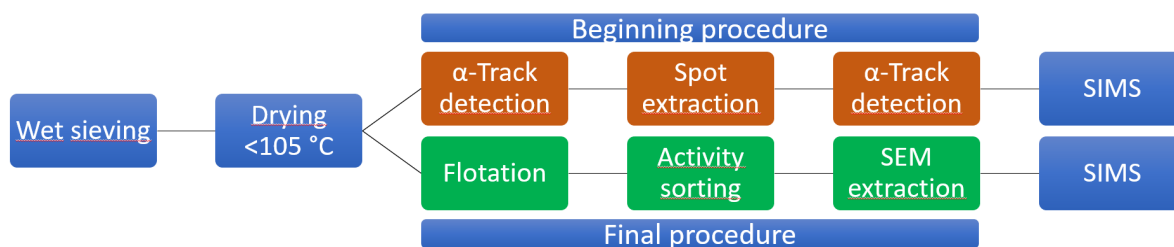
Fig. 3.3   A short Flowchart displaying the particle search procedure. The upper branch shows the process as it was done for the first few particles, still including α track detection and before a SEM was available. At that time, SIMS was used for the first location of the particle. The lower branch shows the final version of the process, skipping α track for the most part, instead including flotation and particle extraction. Here, SIMS is only used for analysis, as SEM is more suitable for the search and allows extraction.

At the beginning of this work, no SEM was available for further analysis. Therefore, a different approach was used to narrow down sample material onto hot particles: several iterations of ATD, followed by SIMS analysis to finally find and measure potential particles. Found particles were fixated in indium foil[Hamann 2017] (particle RW-001) or epoxy resin (particles CP-003 and CP-004), and could not be isolated from the sample material. This process was skipped in favor of flotation and SEM analysis, when these became available, which proved to be more efficient. Hence, the ATD process will be described only shortly in the following, with more emphasis on flotation and SEM. SIMS was later on used exclusively for analysis of extracted or otherwise localized particles and is therefore not part of this chapter.

3.3 ATD

As described in chapter *Background: Methods and Instruments*, the method of ATD for particle search is a time intensive process due to the elaborate sample preparation, exposure time and detector evaluation. However, it is not without potential for future use:
The final process of particle search implemented the search for particles via activity measurement using a standard Geiger counter. This yields results in much shorter time than ATD, but is limited to relatively large particles with high specific activities. To investigate the sample residuals for smaller particles or for samples with higher γ backgrounds, ATD would be superior since it is only sensitive to α radiation and exposure times can be extended for lower activities. Hence, the following process might be used in future investigation into environmental samples.
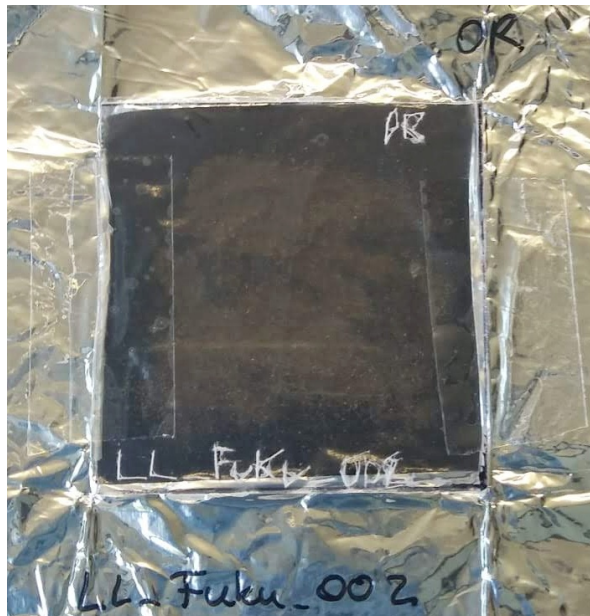
3.3.1 ATD Exposure

The following materials were prepared for one run:

Sample Material Sieved sediment or soil material of the smallest size fraction ($< 65\,\mu$m), to minimize problems with sample topography.

Detectors CR-39 material by various suppliers, cut into $5\,\text{cm} \times 5\,\text{cm}$ squares. Number depending on amount of sample material and available space. Each detector was engraved with a sample identification on the top side.

Support Material $5\,\text{cm} \times 5\,\text{cm}$ squares of double-sided carbon sticky tape, stuck to slightly larger sheets of Al foil, number and sample identification matching the detectors. Short wire pieces fixed to the sides of the tape as vertical spacers.

The sieved sample material was spread carefully over the square of carbon tape. Excess sample was removed mechanically, so that only material sticking to the tape remained. A detector (protective film removed) was then placed on top of the carbon tape, with the wire spacers in between. Figure 3.4 shows the setup, once the detector is fixed to the sample with sticky tape, to reduce the risk of detector movement relative to the sample.

Fig. 3.4 The finished preparation for ATD exposure:
Sample material (brown, here: from Fukushima, Japan) was spread thinly over the black carbon sticky tape, which itself was glued onto a larger piece of Al-foil for ease of handling. The detector was marked with the sample name and another mark (OR) for the upper right corner and then fixed to the sample with two strips of tape. This setup was repeated for each sample and then left for at least several days up to two weeks before etching.

All samples prepared in this way were then left for at least several days up to two weeks of exposure before etching, to acquire signal on the detectors even from very small particles. After this exposure time, all detectors were etched at the same time to reveal α tracks.

3.3.2 ATD Etching and Evaluation

With the exception of extremely high α activity, no tracks could be seen on the detector film directly after exposure. To make this signal visible, the detectors were etched with the following conditions:

Medium: NaOH, c = 6.25 mol/L
Temperature: T = 80 °C
Time: t = 3 h

Experiments were conducted to determine the optimum etching time of 3 h. Less time left α-tracks underdeveloped, whilst more time (up to 5 h were tested) resulted in large and round tracks, smearing the direction information.

Figure 3.5 shows the ATD detector etching setup, that was custom built during this work.

Fig. 3.5 The ATD etching setup:
A tall structure was manufactured out of PTFE material for chemical and thermal resistance, with notches to hold up to 10 detector plates (marked with white arrows). The beaker was then filled with 6.25 mol/L NaOH up to 1 cm above the highest detector, heated to 80 °C and stirred with a magnetic stirrer at the bottom.

A custom constructed PTFE structure was used to hold up to 10 detectors in place whilst covering them in NaOH and still allowing for the liquid to be stirred (figure 3.5). After about

3 h, the stack was taken out and rinsed with DI-water. Larger accumulations of α tracks were already visible as white spots on the material, as shown in figure 3.6a. However, since localization of single particles would not be feasible using SIMS on a 5 cm × 5 cm area, found spots were extracted from the sample using a biopsy punch (3 mm in diameter). The resulting sample discs were then fixed onto Al blocks and four triangulation marks were drawn around the discs with black ink. These blocks were then again used for ATD, to further increase the precision of particle localization preceding SIMS analysis (see images (3.6c) and (3.6d)).

(a) Etched

(b) Spots extracted

(c) Second ATD

(d) Second etching
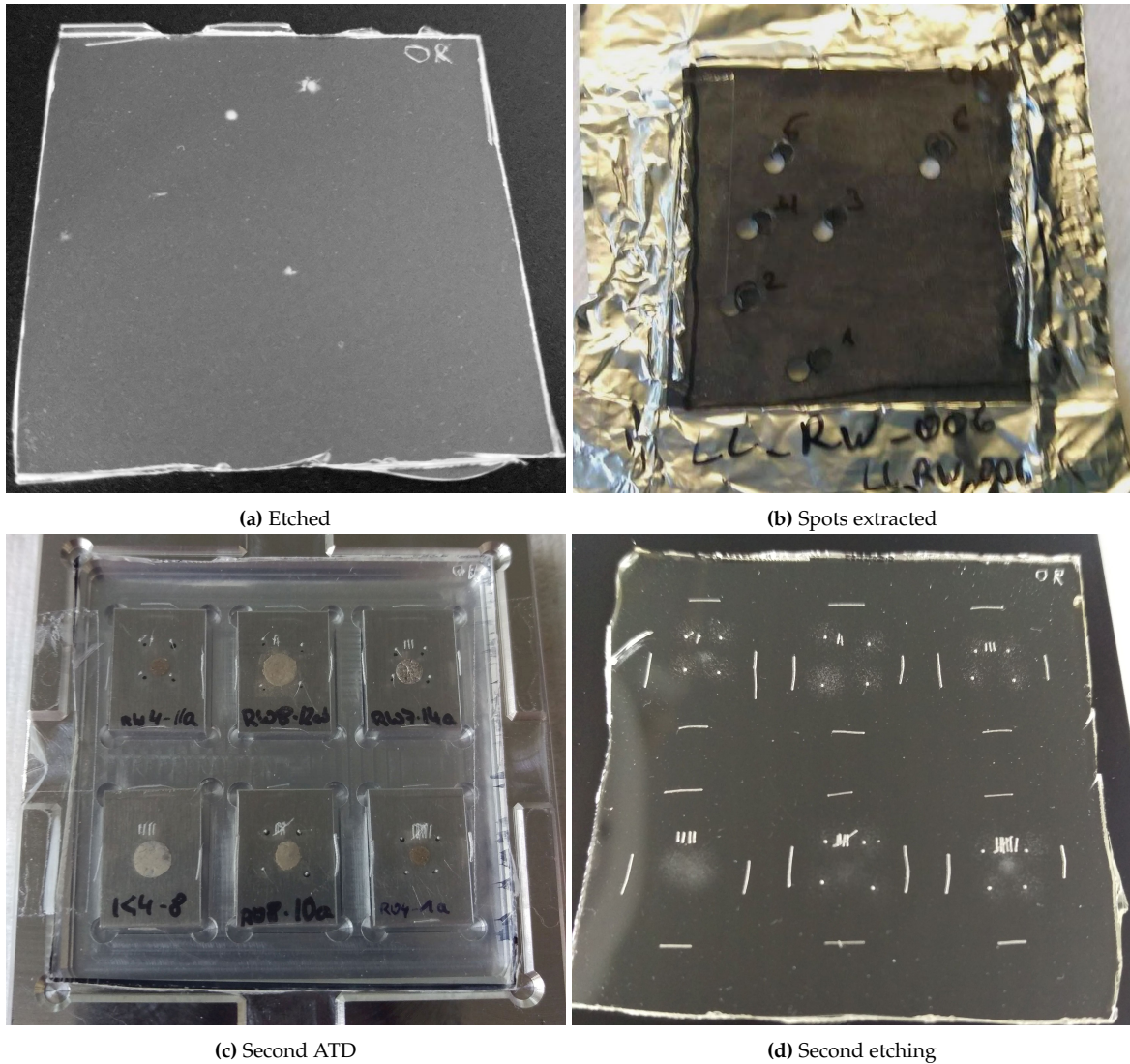
Fig. 3.6   Four images of different stages of 2-step ATD:
Larger accumulations of α tracks were visible as white spots on the etched detector. For the second step, these spots and the silhouette of the detector were marked on a transparent film as shown in (a). This film was then used to extract the respective spots from the sample sheet, using a biopsy punch of 3 mm diameter (see b), which were then transferred to individual Al blocks. Figure (c) shows these blocks in the setup for the second ATD run: Four spots marked around the sample disc, on the Al as well as on the detector for later triangulation of signal positions. The result of this second run is then shown in image (d): Spots were visible with the four markings around them, so in a next step, image editing software could be used to locate the α track sources on the sample discs.

Once the second ATD run was finished, detector and sample were mapped using an optical microscope. The image of the detector was cut and edited to create colored marks of the four triangulation points and the α tracks on a transparent background. The resulting template was then overlayed with the sample image, to locate the α source within a few μm margin, as shown in figure 3.7

(a) α track spot

(b) Overlay with sample
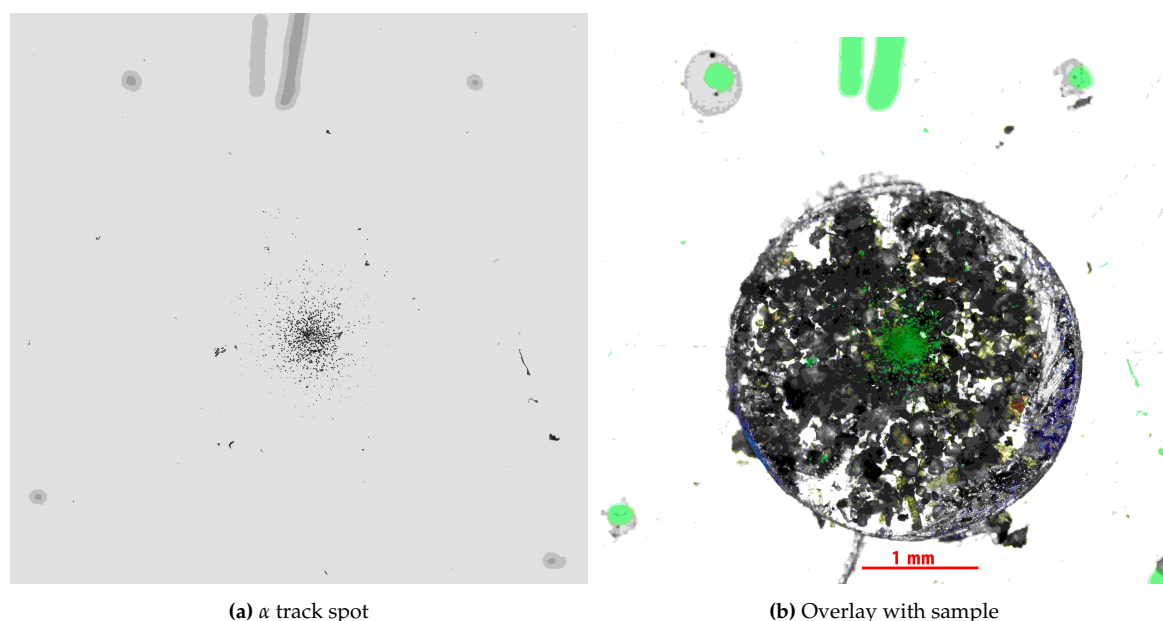
Fig. 3.7   First particle location:
(a) shows the result of mapping a spot on the α track detector with an optical microscope (several images stitched together). The markings on top and in the corners (lines and dots) were engraved into the detector before exposure for identification and later triangulation of the α spot. In the image, they are on the back side of the detector and hence less pronounced compared to the tracks.
(b) is the finished map of the sample. Image (a) was edited for transparent background and green coloring of tracks and marks, the four triangulation spots were then used to locate the spot on the sample. The particle was assumed to be in the center of the α spot, hence only a very small area of the sample had to be investigated by SIMS. The disc diameter was 3 mm.

Image 3.7b shows an overlay of ATD signal in green and the regarding sample image. The α tracks are spreading relatively homogeneously into all directions, indicating that no larger structure is blocking the particle and that it should be in the spot's center. This was an essential part of the procedure to ensure that time spent finding the particle with SIMS was minimal. Still, several days of sample preparation time were needed before this point was reached and the actual particle search could begin in the SIMS.

Later in the work, SEM analysis allowed for faster imaging without need for consideration of sample topography or distribution area, so that SIMS was only used for particle analysis. At that point, ATD was no longer used, because SEM proved faster and more reliable even with larger samples. It was also found that particles with a diameter of > 5 μm were usually detectable by a small window Geiger counter, which again was much faster than ATD, see section Particle Search.

3.4 Flotation

The flotation process is a physical method to separate materials based on their density. Solid material is mixed into a liquid of specific density and subsequently separates into two fractions: One fraction with lower density compared to the liquid, which floats on the surface, and a more dense fraction sedimenting to the bottom of the container.[Plewinsky.1984 Admon.]
In this case, a solution of sodium polytungstate ($Na_6H_2W_{12}O_{40} \cdot xH_2O$) in DI-water was created and adjusted to a density of at least $\rho = 3 \, g/mL$. This solution was then mixed with previously sieved and selected sample material with a volumetric ratio of at least 1:3 (sample:liquid) in centrifuge tubes. To ensure proper mixing and disintegration of agglomerates, the resulting slurry was then sonicated in an ultrasonic bath and finally either left overnight or centrifuged at about 3000 rpm for 15 and 30 min, depending on the centrifuge tubes. When testing for optimal centrifugation parameters, the unusually high density of the liquid had to be taken into account. Typical centrifugation tubes can be deformed or damaged at too high rpm. Figure 3.8 shows a graphic representation of the flotation process.

(a) Mixing   (b) Sonication   (c) Centrifugation   (d) Separation
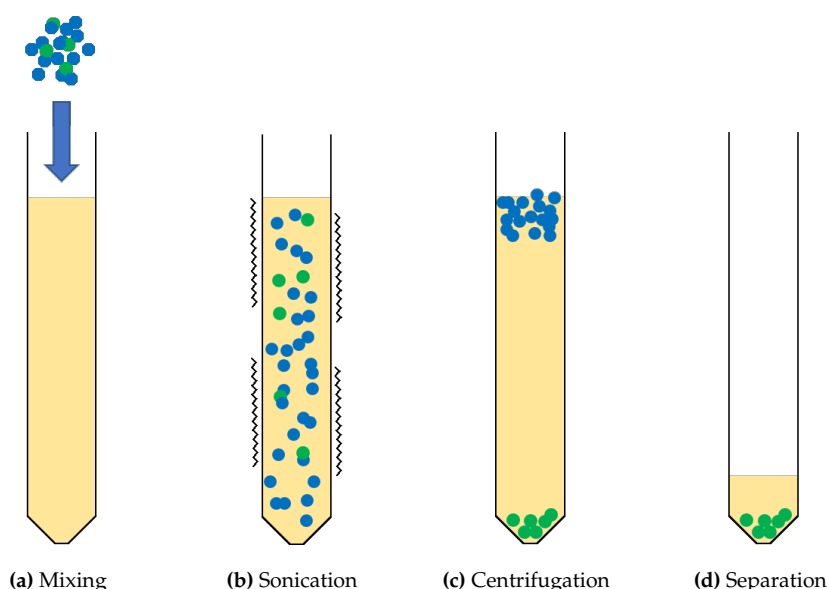
Fig. 3.8   A scheme of the individual flotation process steps:
(a): First a heavy liquid, made of polytungstate and DI-water, is mixed with sample material in a centrifuge tube.
(b): To break up agglomerates and for thorough mixing, the solution is treated in a sonication bath.
(c): After sedimentation over several hours or centrifugation, the density separation is finished.
(d): The lighter fraction ($\rho < 3 \, g/mL$) is separated.

After centrifugation, the solid material had divided into a comparatively small sedimented and a floating fraction, the latter containing most of the original sample material. With sufficient liquid in between the two fractions, the bottom of the centrifuge tube could be frozen in liquid nitrogen and the top material washed out with DI-water. Both fractions were

then individually vacuum filtrated over glass fiber filters with pore sizes < 1 μm and the resulting filters with the sample remains dried under heat lamps and subsequently stored in sealed Petri dishes. These two individual sample states are referred to as "heavy fraction" and "light fraction".

3.5 Particle Search

Both ways of sample preparation and narrowing down the sample material - ATD and flotation - still do not yield isolated spent nuclear fuel particles, which would facilitate further analysis. Instead, both result in a much smaller fraction of the original sample with a much higher ratio of fuel fragments to inactive soil or sediment particles. However, further analysis like SIMS or beamline methods proved to be highly inefficient or even not possible at all without extracting the particles. γ spectrometry of samples is much more feasible for single extracted particles than for bulk samples. The background level of the residual material, for example from adsorbed ^{137}Cs, is unknown in the latter and might interfere with the measurement. By isolating the particle in question, such background interference is removed entirely.

Since the fuel fragments in question are not distinguishable from the surrounding material by any optical means, other attributes have to be utilized to differentiate between fuel particles and sediment or soil. One attribute, the relatively high density of the uranium oxide compound, has been used in the flotation step to separate it from silicates- or alumosilicates and organic soil material. However, as seen later on, not all remaining particles are fuel fragments: The majority of the material is still made up of particles containing Zr, Fe, Ba and other heavier elements (based on individual EDS measurements). Instead of optical microscopy, which has no viable option of differentiation, electron microscopy is capable of delivering a contrast based on the electron density of analyzed particles' main constituents, as described in subsection BSE. Additionally, an EDS detector can identify main elements within analyzed particles, to confirm or rule out a high uranium content.

Samples resulting from the described ATD procedure can be directly analyzed by SEM, because the sample geometry matches the SEM requirements very well. The existence of a particle is now confirmed and its location is known within a small margin. Samples coming from the flotation without additional ATD analysis however, have to be processed further before being compatible with SEM analysis.

Filters of the heavy fraction can hide particles in between fiber structures and also still contain too much inactive material. Using an optical microscope, two pairs of tweezers and a small window Geiger counter, these filters were taken apart down to individual fibers, and detected activity carefully separated. Found spots of activity were then fixed to a carbon sticky tape

with minimal pressure to avoid pushing particles too deep into the tape. Figure 3.9 shows a schematic of the resulting sample holder. The carbon sticky tape sits on Al foil wrapped around an Al block to allow easy handling and reusability.
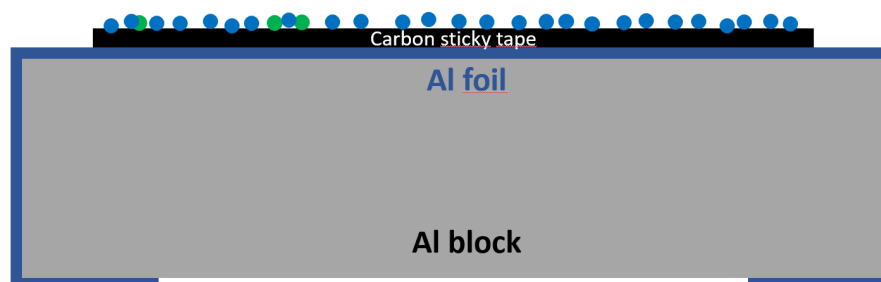
Fig. 3.9   A sketch of an SEM sample holder for particle search:
This shows the way filtrated sample material is mounted for SEM analysis after preselection by flotation and filter dissection. Separated sample material possibly containing hot particles is fixed on the glue surface of the carbon sticky tape. Everything except the sample is conductive to reduce potential surface charge buildup to a minimum. The extra Al foil wrap is used for easier reusability of the Al blocks. Dimensions of these blocks were 5 mm x 15 mm with 3 or 5 mm in height.

Such sample holders with measurable activity on the tape could then directly be introduced into the electron microscope for further analysis.

3.6 SEM

Introduction   The BSE contrast of an electron microscope is an ideal tool for identifying nuclear fuel particles. They can not be distinguished by color or morphology whilst mixed with large amounts of regular soil or sediment material, so optical microscopy or SE imaging are not useful. As explained earlier, SIMS is capable of identifying particles based on isotopic patterns of U^+, UO^+ and $UO_2{}^+$, but greatly suffers from sensitivity to single µm changes in topography and time consuming scans of larger areas in the mm^2 range. Additionally, since SIMS is a highly surface sensitive method, environmental contaminations in the nm range require intense sputtering before measurements, further increasing the time used for the particle search.

A SEM instead has a depth of field of several 10 µm and is capable of fast large area scans, depending on the magnification. In comparison to SIMS, where each single scan has to be evaluated to identify potential uranium signal, the BSE contrast depends greatly on the electron density of the imaged materials main components. Since U is one of the heaviest naturally occurring elements, the BSE contrast can be adjusted to show Si based particles in dark grey or black, Fe in a fading gray and elements with high atomic numbers like W and U in bright white. An example is given in figure 3.10.
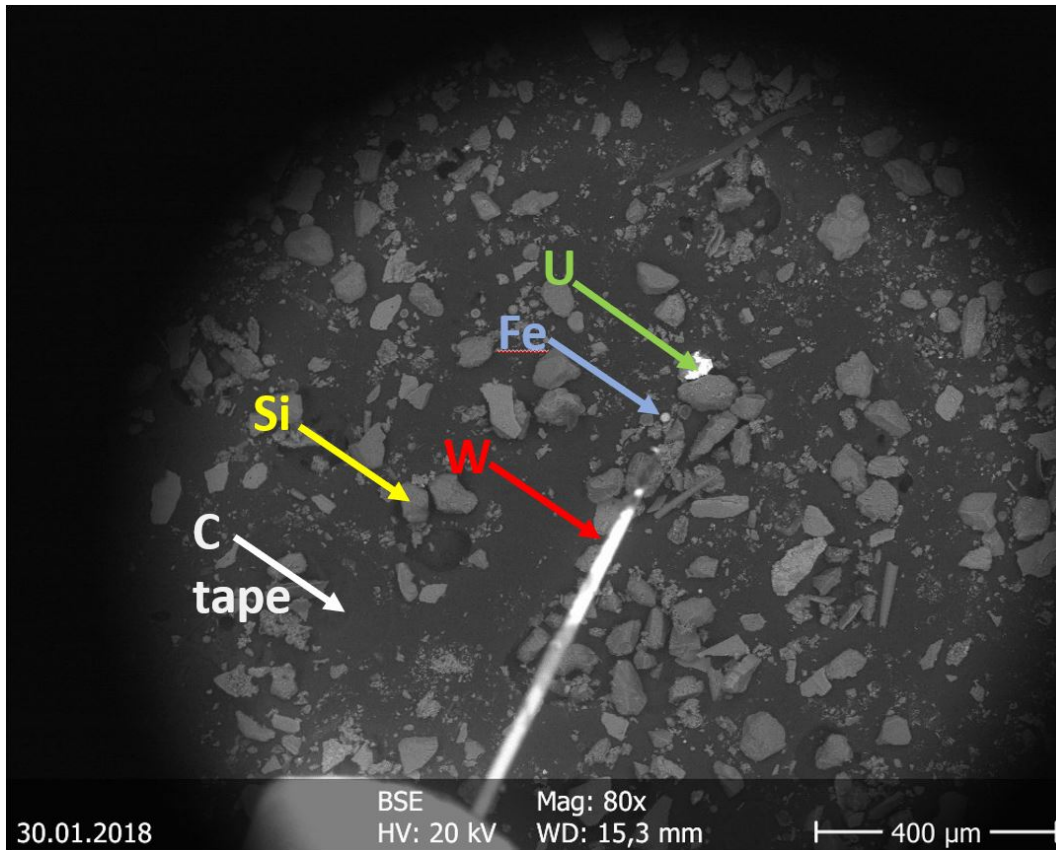
Fig. 3.10 Finding spent fuel particles with SEM:
The image shows an area of about $1\,mm^2$ with cooling pond sediment material from the CEZ in the BSE mode of the SEM. Most of the visible particles are naturally occurring sediment with Si as main element. Also often found in the sediment, even more so after flotation, are FeS particles, agglomerated to form a spherical shape (marked in the image as Fe). These appear brighter, although still less highlighted than a particle containing uranium or a tungsten needle.

Conditions   Since the particles in question were electrical insulators, one problem had to be compensated for:

Scanning such samples with an electron beam leads to charging effects on the surface. As a result, image distortions occurred, especially when using the SE detector. Their intensity varied, depending on acceleration voltage, beam current and magnification, whereby an increase in each individual parameter would enhance surface charge buildup. In extreme cases, imaging of samples became impossible even in BSE contrast, whilst too strong charging effects even lead to particles being pushed from the surface due to charge repulsion.

Two different techniques are commonly used to compensate for insulating samples: The first method is to sputter the sample surface with a conductive agent, usually Au or C. However, since later in this work the sample surface was the focus of interest, application of a surface coating was not an option. Instead, the second method was applied: The used electron microscope was equipped with a LV option and also a GSE detector.

By using the GSE and a LV at about 1 mbar, excess surface charge could be compensated by the residual atmosphere in the SEM chamber, and imaging became possible even on electric insulators. Instead of the SE detector, the GSE is used, which is less affected by the atmosphere, but instead is prone to a higher BSE background. Also, while using the GSE detector, care had to be taken with respect to the contrast setting: Too high voltages in this setting quickly led to electrical flashovers, especially in combination with high magnification. Additionally, imaging quality diminished for acceleration voltages below 15 kV and high magnifications. In conclusion, LV imaging was very useful for finding and extracting particles, however was not used for high quality imaging and EDS analysis, since charging effects were greatly reduced for extracted particles.

Contrast settings When first focusing on the sample material, the GSE was used, because it could work simultaneously with the SEM's internal camera. This camera was used for a first positioning of sample and micromanipulator needle, however operated with an InfraRed (IR) lamp, which again would interfere with the BSE and EDS detectors. Once the sample surface was in focus and the outer perimeters of the carbon tape were mapped, the detection mode was switched to BSE. Then brightness and contrast settings were adjusted in the SEM software, so that sediment particles were almost invisibly dark and the W needle of the micromanipulator was as bright as possible to achieve a wide range of contrast.

EDS Whilst a particle is clearly visible in figure 3.10 due to its high contrast, it also becomes clear that a differentiation between heavy elements like U and W is not feasible with BSE imaging alone. After flotation, the problem is mitigated slightly, as most of the remaining particles contain heavy elements like Fe from FeS or Ba from baryte type minerals. These can be used to adjust the BSE contrast more precisely to separate them visibly from U particles. However, this still only supports finding heavier particles, but cannot actually identify fuel fragments. A fast and safe way to identify fuel particles is the measurement of element specific X-ray emission with the built-in EDS detector. Within a few seconds, a spectrum like the one shown in figure 3.11b is acquired and reveals the presence of U, when the particle measured is a fuel fragment.

(a) BSE image of particle CP-001

(b) EDS spectrum of the particle
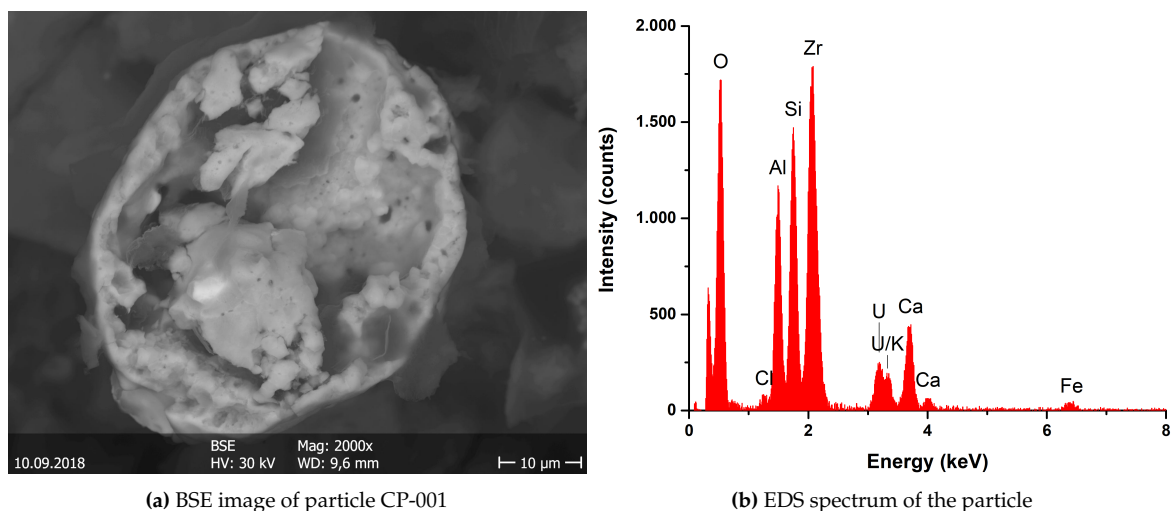
Fig. 3.11 Particle identification by EDS:
(a) The particle CP-001 was at first found by BSE imaging, where it was highlighted against the background. However, this highlighting was only an indication and only proved that it would contain heavy elements. It was impossible to know for sure whether this would be U or maybe W or Pb, as both had been found in samples before. To identify the main components, the EDS detector built into the SEM was used.
(b) This EDS spectrum shows the low energy range (0 and 8 keV) and identifies a number of elements. Of special interest are Zr, as that could be originating from a reactor, but even more the clear U signal. With U identified, it could be assumed that this particle originated from spent nuclear fuel and should therefore be further investigated. A safe distinction from natural uranium has to be given by isotopic ratio analysis via SIMS.

Measuring EDS is possible in LV or HV mode. However, as with imaging, higher quality and precision is achieved in HV mode. In both cases, the following settings have almost always been chosen:

Acceleration voltage > 20 kV to include the higher energy *L*-edges of U and Zr in the measurement for better identification

Spotsize = 5 slightly higher than for imaging. This increases the beam current on the surface and therefore boosts the signal, resulting in significantly higher counts per second (cps)

Measurement time: several minutes or until several 1000 counts were collected on the U signal

Distance: 10 mm The optimal working distance for the EDS detector (hardware defined). Not always possible to use when working with the micromanipulator.

Although an EDS mapping over a large imaging area was generally possible, this was never used for particle search. To achieve the necessary resolution, mapping would have taken much more time than searching for bright spots with BSE and subsequently acquiring EDS spectra from individual particles of interest.

In the next step, it was attempted to extract identified uranium-bearing particles for further analysis. As the direct contact to a W needle greatly increases the electrical conductivity of

extracted particles, techniques sensitive to surface charge buildup like SIMS and HV-SEM become more readily available and yield higher quality results. Additionally, γ spectrometry can be used to quantify radionuclides like ^{137}Cs, ^{241}Am and ^{154}Eu, since potential interference from surrounding sample matrix is no longer of concern. A time-consuming particle search with SIMS is no longer necessary.

3.7 Particle Extraction

Extracting a single nuclear fuel particle from the surrounding sample matrix was a multi-step procedure. The key moments are shown and explained in SEM images in figure 3.12.

(a) Check: Particle not obstructed?

(b) Check: Particle accessible?

(c) Contact particle and cure glue.
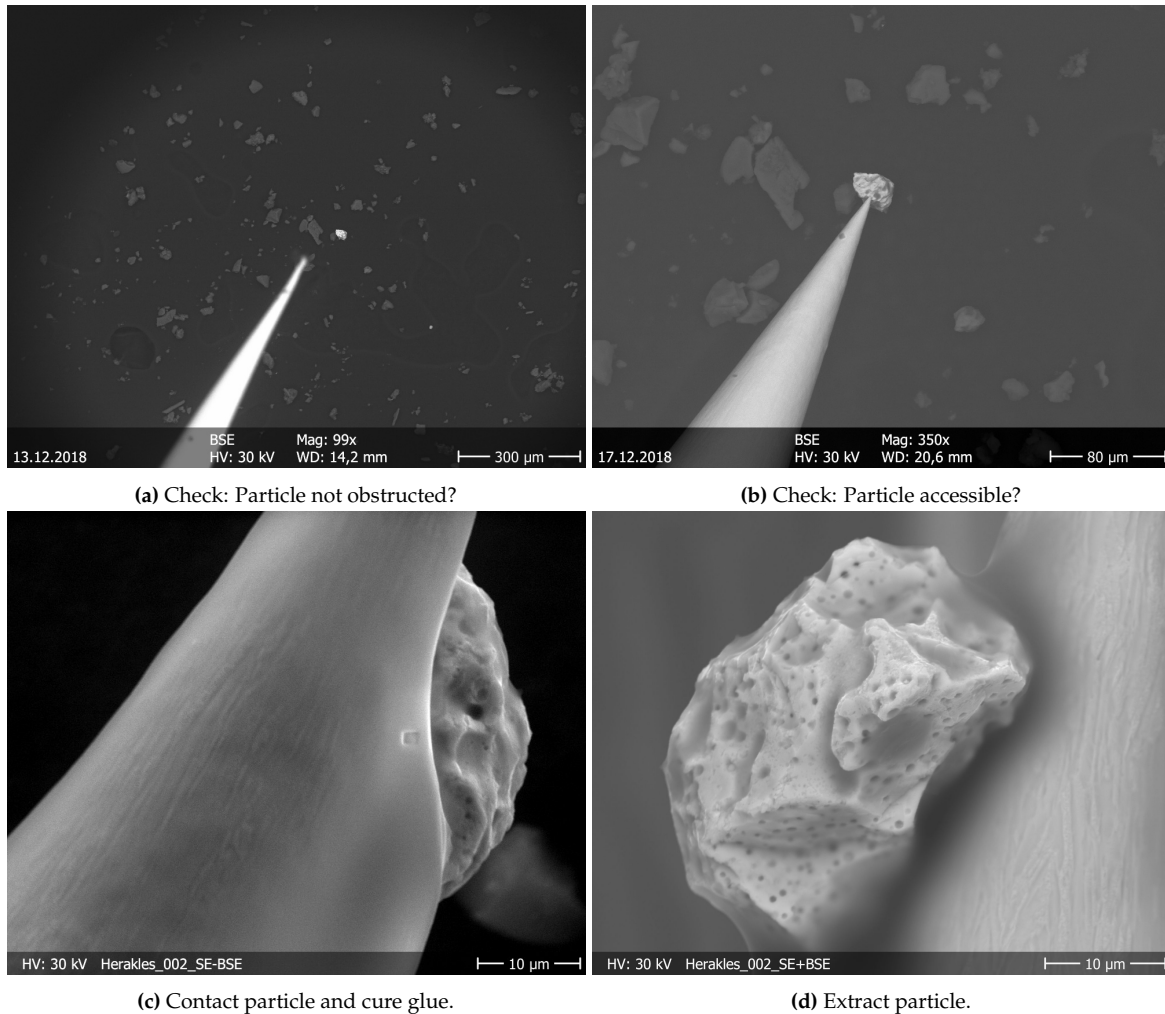
(d) Extract particle.

Fig. 3.12   Four images, exemplary for the process of particle extraction with the micro-manipulator:
(a) The particle before any attempts of manipulation. If the needle's access to the particle is obstructed by other particles, some preparation might be needed. This includes turning or tilting of the sample holder or relocation to a less crowded sample holder. The particle shown here is very well suited for extraction.
(b) A first contact is made to check the accessibility of the particle with the needle. A contact area as large as possible is ideal without exerting high pressure onto the particle. In case of problems, tilting of the sample holder proved helpful.
(c) After a short dip into the glue, where care should be taken to not use excessive amounts of glue, needle, glue and particle are brought into contact. Surface contrast imaging with SE or even SE-BSE is useful to monitor glue migration over the particle surface. The glue is then hardened by using high magnification, beam current and acceleration voltage. Small burn traces can become visible in the glue.
(d) Finally, the particle is extracted from the sample, mounted into an appropriate needle holder and turned into an angle that makes it accessible for imaging and SIMS.

After setting up the SEM with the micromanipulator, a fitting needle and the sample, two conditions have to be checked: First, the particle should be as unobstructed as possible (image 3.12a), to allow a clean extraction without interference of surrounding materials. Second, the particle had to be accessible for the tungsten needle (see figure 3.12b). This mostly was a problem of local topography and the shape of the needle, as it was important to prevent the needle from touching the carbon tape. Often, but not always could this be achieved by simply lowering the sample stage.

Once the conditions were set, the needle was moved over to the SEM stub with SEMglu™, carefully dipped into the glue and removed again, ideally taking up a thin layer of glue. Excess amounts of glue were wiped on the SEM stub to avoid covering large areas of the particle surface, as this could interfere with later analysis or even with the curing process. Then, needle, glue and particle were brought in contact and the glue cured by the focused electron beam (see figure 3.12c). Finally, the particle could be lifted out of the carbon tape by the micromanipulator and ended up sticking to the needle, extracted from the residual material. In the following, the individual steps are described in detail.

Setup: After locating a particle, the sample holder was fixed onto a SEM stub using carbon tape and placed in the middle of the SEM sample stage. The micromanipulator was set up within the SEM chamber with an attached W needle, as well as a regular SEM stub with a minimal amount of SEMglu™. Before closing the chamber, the needle tip was adjusted manually in close range to the sample. Next, the chamber was closed and set to LV at 1 mbar.

Check accessibility: Using SE or GSE imaging and the internal IR camera, the particle was brought into focus and the needle positioned close by. As a first step, the needle tip was lowered slowly onto the particle until it either touched, or was caught anywhere else. Potential obstructions were usually larger particles surrounding the spent fuel particle, or the sample holder and carbon tape themselves, when the tip of the needle came in at a very narrow angle. For sample material obstructing the hot particle of interest, in some cases the solution was a rotation of the stage into a direction without material blocking the access to the particle. If the problem was the needle itself, the only option was improving the attack angle of the micromanipulator. Since the manipulator could not be set to a higher position relative to the stage, the other option was to lower the sample stage. This however, led to reduced imaging quality and contrast, especially when using LV mode, and sometimes even lowering the stage to the minimum height was not enough to touch the particle with the needle tip. For such cases, the sample mounting was adapted, as described in figure 3.13.

(a) SEM stub with sample holder

(b) Particle (green) is blocked

(c) Tilted sample holder

(d) Needle can reach particle
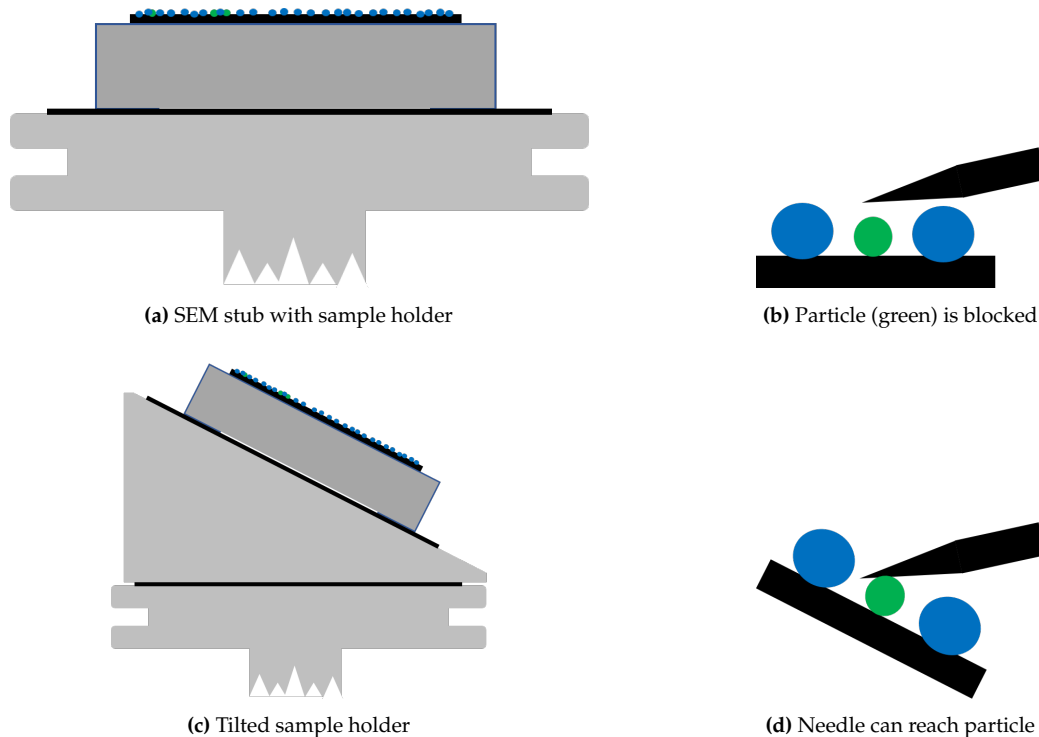
Fig. 3.13   Tilting the sample holder for easier access to obstructed particles:
(a) The general way a sample would be introduced into the SEM is fixing it onto a SEM stub with carbon tape. For sample holders based on Al blocks, the additional stub was not generally necessary, but useful to avoid sample movement when using the micromanipulator for extraction.
(b) In some cases, identified nuclear fuel particles are surrounded by other particles or located in an indentation within the carbon tape. Because the micromanipulator can only access the sample surface in a maximum angle, this can prevent the particle from being extracted. This issue could rarely be resolved by pushing away surrounding particles with the micromanipulator.
(c) A regularly used solution to the problem was to tilt the sample on the stub, using an Al angled block. This setup usually obstructed the EDS detector and the height difference required constant adjustment of the focus due to the limited depth of field when scanning the sample, whilst also complicating maneuvering the micromanipulator, which is why it was only used when needed.
(d) Particles on a tilted sample holder were more accessible to the needle, even though they remained obstructed by other materials.

Tilting the sample holder by around 45° not only allowed better access to obstructed particles, but also opened a way to prevent narrow needle angles, hence preventing the needle sticking to the carbon tape before touching the particle. At the same time, a working distance of about 10 mm to 15 mm could now be arranged without negatively interfering with the micromanipulator and its needle.

Drawbacks however, were obstructed sight with the in-chamber IR camera and in many cases greatly reduced efficiency of the EDS detector.

With now unhindered contact between needle and particle, the actual extraction could begin.

Glue: The SEMglu™ used in this work is a specialized product, suitable for HV usage and curing only in a highly focused electron beam at high beam currents. Hence it stayed perfectly liquid, when imaging it at low magnification. For extracting a particle, the sample stub with the glue was first adjusted into focus, then the needle maneuvered close to the surface, in cases of high differences in height just using the internal camera. Then, with as little magnification as possible (to avoid curing the glue) the needle tip was dipped into the liquid, slightly moved around and pulled to the top or side out of the glue. Ideally, the glue just covered the tip without creating large drops, that later on would cover the entire surface of the particle. Figure 3.14 shows particles CP-003 and CP-004 after extraction and demonstrates the difference between just enough (CP-004 on the right) and an excessive amount (CP-003 on the left) of glue.
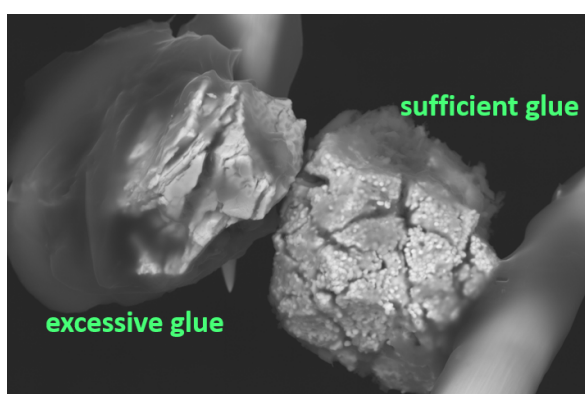
Fig. 3.14   Excessive vs sufficient amounts of SEMglu™ when extracting particles:
CP-003 (on the left) took several attempts at extraction and in the process became covered with a large amount of glue. The same could happen even at a single attempt when using too much glue, which could block the particle from being detected in the SIMS or potentially even from chemical leaching. Particle CP-004 - on the right - was extracted in the first attempt using a minimum amount of glue so as not to cover the particle, but which was enough to create a stable bond between particle and needle.

Too much glue on the particle can get in the way of subsequent forms of analysis. SIMS is especially sensitive to the surface and would not be able to detect the particle if the surface was covered in glue. When chemical leaching is applied, a full cover of the particle could possibly prevent contact between particle and leachant if the glue was more resistant to the latter. In cases with too much glue, the SIMS was used to sputter off the top layer. The particle was located by navigating along the needle's W ion signal and constant comparison with SEM images, and once found, a specialized ion gun of the SIMS, the Gas Cluster Ion Beam (GCIB), was used to sputter clean the surface area of glue and adsorbed contaminants. The GCIB creates a beam of Ar cluster ions, which are capable of sputtering large areas of softer material like adsorbed air molecules and organics.

Extraction: After the extraction of the particle was successful, the needle was taken out of the micromanipulator and carefully placed into a specialized sample holder. The final state of the needle is schematized in figure 3.15: An Al block with a 0.5 mm notch, in which the needle rested, secured by a spacer ring and screw at the end. For detailed descriptions of such sample holders, refer to BOSCO, WEISS, ET AL.[Bosco et al. 2020] and HANEMANN[Hanemann 2019].

Fig. 3.15   A schematic representation of the needle in a custom made needle holder:
It is comprised of an Al block with a notch 0.5 mm deep. A needle, with a particle glued to the tip, is inserted into the notch and fixed using a spacer ring and screw, then turned around until the particle rests on top. The needle holder has additional holes drilled into it, to allow safe mounting on the SIMS topmount sample holder. This setup can be used for SEM imaging and EDS analysis, SIMS and SNMS as well as for optical microscopy and γ spectrometry, without having to dismount the needle. For storage, a fitted cap was mounted over the needle tip for protection.

When set into this holder, the needle was turned before fastening the screw, so that the particle itself rested on top of the needle. This was necessary to allow the following methods of analysis, like SIMS, SNMS, γ spectrometry and also HV-SEM including EDS and in some cases EDS-mapping. Additionally, for most particles mounted this way, the issue of electrical isolation was minimized, due to the tungsten wire grounding the charge. Therefore, HV SEM imaging and EDS was easily possible, as well as SIMS without major charge compensation efforts, allowing more precise and longer measurements. Hence, once a needle had been mounted into such a sample holder, it could be handled much easier and with greatly increased safety. It only had to be dismounted for beamline analysis or chemical leaching experiments.

This sample mount was designed to be compatible with all mentioned analysis techniques: It could simply be set onto the stage inside the SEM and had special drill holes to match the grid of the SIMS topmount sample holder. For γ spectrometry, a specialized platform was constructed, to hold either the particle holder or a point source for calibration in the exact same reproducible place.

For storage, a specially fitted cap was mounted over the needle tip, also equipped with hollow space inside to avoid contact between cap and needle.[Bosco et al. 2020] The now sealed sample can then be stored in a custom constructed storage rack.

3.8 Particle Search Results and Discussion

3.8.1 Process Evaluation

Sample Sieving: This process was found to be the first step to finding a larger number of particles. As the average diameter of particles was found to be well below 63 µm, sieving of the whole sample material down to a small fraction significantly decreased the amount of soil or sediment that had to be investigated. Easy and fast to do without expensive equipment and without chemical influence on the samples, whilst saving a lot of time in the rest of the process, this was one of the most valuable steps.

For a superficial monitoring of the sample's activity, a common large area contamination monitor was used on each size fraction resulting from the sieving. The result was especially clear for the Chernobyl Cooling Pond sediment sample, where after sieving the count rates for every fraction larger than 63 µm reduced to a minimum, whilst the smallest fraction reached count rates similar to the initial ones. A more sophisticated version of this monitoring would involve using a γ detector to exactly monitor the activity distribution over all fractions, but was not deemed necessary for the purpose of finding particles. Since the activity detected this way was presumably mostly originating from ^{137}Cs, this monitoring worked well for the sediment, where the majority of Cs was bound in particles, but gave less clear indications for soil and litter samples from Kopachi and the Red Forest, which included organic material like roots and leaves which are prone to accumulate ^{137}Cs.

ATD: Before an electron microscope was available, ATD was essential for localizing particles within the samples. Since the use of BSE imaging in combination with an EDS detector sped up the search for particles however, ATD became quite redundant and was not used for the rest of this work.

The method still has its uses in particle search, for example for finding hot particles in high ^{137}Cs-background samples.

SIMS: As mentioned before, SIMS was used for locating particles only until a SEM became available. It had a wide variety of uses for analysis of already located and prepared particles, but was highly inefficient for particle search. The main problem was the high sensitivity for topography: If the ion beam focus was set only a few µm higher or lower than the particle's surface, the particle could not be detected. Also, the SIMS's LMIG was mounted in a 45° angle, which is diffent to the SEM, where the electron beam is aimed at the sample perpendicularly. Due to this angle, larger particles surrounding the uranium particle could block the ion beam. Although the SIMS was generally capable of scanning larger areas of up to 500 µm × 500 µm,

this could never be used for particle search, since the signals for U^+, UO^+ and UO_2^+, which were the most prominent for particles, would just vanish in the SI spectrum background. Additionally, a significant peak broadening resulted from the topography. In conclusion, only small areas of about $50\,\mu m \times 50\,\mu m$ could be scanned at once, and still needed long measurement times of up to $30\,min$ to get a good chance for identification of uranium signal. Ideally, these scans had to be repeated for several sample height settings. This whole process resulted in finding one particle in a preceding thesis[Hamann 2017] and two particles for this work: CP-001 and CP-002, although only through detailed examination and combination of ATD and optical microscopy and many SIMS scans, closing in on the particle by identifying surrounding shapes in the SI mappings. For comparison, later on finding the same particles in the SEM took only a few minutes on the first try whilst using the BSE contrast.

For the analysis of already extracted particles however, most of these problems were of no concern. Since the particle was fixed to a tungsten needle and turned to the upside, finding the particle was only a matter of following the W^+ signal until the particle came into focus, followed by height adjustment and short sputter-cleaning of the surface.

Flotation: After sieving the sample material, flotation was the second step in narrowing down the bulk. Preparing the high density liquid out of solid sodium polytungstate ($Na_6[H_2W_{12}O_{40}]$) proved fast and easy, as did the density adjustment. Creating a slurry of sieved sample material in the heavy liquid and the following centrifugation was realized within $1\,h$, the subsequent vacuum filtration and washing of the sample even faster. The flotation's results after separation of the sample into a heavy and a light fraction was similar to the results of sieving:

For the Cooling Pond sediment, the activity of the light fraction was barely measurable, whilst most of the previously measured activity was collected in the heavier fraction. This led to the assumption, that the small lighter fraction contained most of the particles, since these were presumably the main source of ^{137}Cs. As a result, it can be assumed that the whole method was very successful in increasing the chance of locating nuclear fuel particles.

Similar observations were not possible for Red Forest (RW) and Drillcore (BK) samples, as sieving for these was skipped due to their small sample sizes. Kopachi (KOP) samples however showed similar effects.

The second step here was to prepare the particles for SEM analysis. Simply touching the heavy fraction filter with a sample stub equipped with carbon sticky tape was the quick and easy approach. This was successful in a way, as particles could be retrieved from such stubs. However, the carbon tape was then also filled with inactive particles and fibers from the filter, which altogether interfered with the particle extraction. The more complicated way involved taking apart the filter almost fiber by fiber with tweezers and an optical microscope, closely monitoring activities with the small window Geiger counter. This process took a

comparatively long time, but resulted in very clean sample stubs, sometimes containing almost nothing apart from the particle in question, from which the following SEM extraction benefited greatly.

SEM: Finding and imaging particles via SEM was relatively fast and easy when using the EDS detector for confirmation. With the micromanipulator and a propped tungsten needle in the imaging range, the contrast could be adjusted from the beginning almost to an optimum and the surface of a sample could be scanned frame by frame. Depending on the particle size, this was relatively fast and in the end, many samples could be scanned per day.

It should be noted however, that without proper sample preparation like sieving and flotation, even SEM was futile in finding particles. For maximum efficiency, sieving, flotation and subsequent preparation with Geiger countering and tweezers would be highly advisable.

Extraction: The successful extraction of particles was a long process of learning and experience to find the optimum conditions. There was no standard protocol for this, as each single particle was an individual pick, depending greatly on the preceding preparation but also particle size, quality of the tungsten needle, proper setup in the SEM and many other factors. In conclusion, although the entire extraction process can take well upwards of a day and need experience to operate efficiently, the advantages are extensive. Extracting a particle opened the door to a vast number of analysis techniques afterwards. Without extraction, no reliable γ spectrometry would have been possible, SIMS and SNMS would have been much more complicated if not impossible. Extraction also was necessary for speciation methods like beamline analysis and single particle leaching.

At the end of this work, a sample preparation routine was created that set conditions for a successful extraction as close to an optimum as possible. Although each individual particle still remained a challenge, this step was certainly the most crucial down the line to single particle analysis and therefore well worth the effort.

3.8.2 List of Particles

A full list of particles is depicted in table 3.2. All particles listed there, with the exception of RW-001, were found as part of this thesis or related B.Sc. theses[Hanemann 2019],[Leifermann 2018]. Whether individual particles were extracted or whether subsequent analysis was done, strongly depended on several factors:

1. **The progress of this work, when the particle was found:**

   With growing experience and development of the methods, extraction became increasingly more feasible.

2. **Particle size:**

   Very small particles were much harder to extract, especially when trying to avoid covering them in glue. Also, larger particles were preferred, for better results in SIMS and γ spectrometry.

3. **Particle accessibility:**

   Some particles were blocked by larger amounts of surrounding material or just sunk into the carbon tape too deep for extraction. Particles CP-001 and CP-002 were fixed without carbon tape but instead with epoxy resin on Al foil, resulting from earlier experiments, and could not be extracted.

Tab. 3.2   A list of 58 particles found within the scope of the SIRIUS project:
All particles with the exception of RW-001 were found as part of this thesis or related B. Sc. theses. Extraction and subsequent analyses depended strongly on size and surroundings and method of fixation for individual particles.
Four different locations were investigated, which are indicated by the particle denomination:
BK: Drillcore from the city of Prypjat
CP: Sediment from the Chernobyl Cooling Pond
KOP: Soil from the Kopachi site
RW: Moss from the red forest area
* Particle found as part of the B.Sc. thesis of HANEMANN[Hanemann 2019]
** Particle found as part of the B.Sc. thesis of LEIFERMANN[Leifermann 2018]
*** Particle found as part of the PhD thesis of HAMANN[Hamann 2017]

Particle	Size [μm x μm]	Extracted	γ-Spec	SIMS	SNMS
BK-001*	35 x 20	×	×	×	×
BK-002*	25 x 20	×	×	×	×
BK-003	15 x 40	×	×	×	×
BK-004	8 x 10	×	×	×	×
BK-005	40 x 30	×	×	×	×
BK-006*	17 x 19	✓	✓	✓	×
BK-007*	20 x 30	✓	✓	✓	×
BK-008*	20 x 25	✓	✓	✓	×
CP-001	30 x 30	×	✓	✓	×
<td colspan="6" align="center">Continued on next page</td>					

Particle	Size [µm x µm]	Extracted	γ-Spec	SIMS	SNMS
CP-002	30 x 40	✕	✓	✓	✕
CP-003	20 x 40	✓	✓	✓	✓
CP-004	56 x 42	✓	✓	✓	✓
CP-005	25 x 30	✕	✕	✕	✕
CP-006	40 x 30	✓	✓	✓	✓
CP-007	30 x 30	✕	✕	✕	✕
CP-008	60 x 50	✕	✕	✕	✕
CP-009	29 x 33	✓	✓	✓	✕
CP-010*	6 x 12	✕	✕	✕	✕
CP-011**	15 x 12	✕	✕	✕	✕
CP-012**	15 x 15	✕	✕	✕	✕
CP-013	20 x 25	✕	✕	✕	✕
CP-014**	8 x 8	✕	✕	✕	✕
CP-015**	15 x 10	✕	✕	✕	✕
CP-016**	11 x 10	✕	✕	✕	✕
CP-017**	10 x 10	✕	✕	✕	✕
CP-018**	5 x 5	✕	✕	✕	✕
CP-019**	5 x 4	✕	✕	✕	✕
CP-020**	8 x 8	✕	✕	✕	✕
CP-021**	6 x 4	✕	✕	✕	✕
CP-022**	5 x 4	✕	✕	✕	✕
CP-023**	4 x 4	✕	✕	✕	✕
CP-024**	20 x 20	✕	✕	✕	✕
CP-025	37 x 39	✓	✓	✓	✓
CP-026	30 x 18	✓	✓	✓	✓
CP-027**	10 x 12	✕	✕	✕	✕
KOP-001	64 x 55	✓	✓	✓	✓
KOP-002	27 x 45	✓	✓	✓	✓
KOP-003	16 x 18	✕	✕	✕	✕
KOP-004	36 x 33	✓	✓	✓	✓
Continued on next page					

Particle	Size [μm x μm]	Extracted	γ-Spec	SIMS	SNMS
KOP-005	16 x 14	✗	✗	✗	✗
KOP-006	25 x 10	✗	✗	✗	✗
KOP-007	undefined	✗	✗	✗	✗
KOP-008	26 x 29	✓	✓	✓	✓
KOP-009	12 x 12	✗	✗	✗	✗
KOP-00X	7 x 8,7	✓	✗	✗	✗
KOP-010	49 x 43	✓	✓	✓	✓
KOP-011	32 x 30	✓	✓	✓	✓
RW-001***	12 x 8,7	✗	✗	✓	✓
RW-002**	15 x 15	✓	✗	✗	✗
RW-003**	10 x 10	✗	✗	✗	✗
RW-004**	6 x 6	✗	✗	✗	✗
RW-005**	4 x 4	✗	✗	✗	✗
RW-006**	4 x 4	✗	✗	✗	✗
RW-007**	12 x 12	✗	✗	✗	✗
RW-008**	2 x 2	✗	✗	✗	✗
RW-009**	5 x 5	✗	✗	✗	✗
RW-010**	10 x 10	✓	✓	✓	✗
RW-011**	4 x 6	✗	✗	✗	✗
RW-012**	4 x 4	✗	✗	✗	✗

In summary, 57 particles were found within the course of this work, of which 18 were extracted and mounted onto tungsten needles, being available for further analysis. Which methods were used on those particles however, depended on individual particle size and activity for SIMS and γ spectrometry and, in the case of beamline analysis, on the available measurement time.

3.8.3 Final Routine for Particle Search

As a result of the evaluation of all used methods, a general routine is suggested for finding and extracting nuclear fuel particles within solid samples. This should be independent of the sample's origin and be equally useful for sediment or soil samples as well as litter or ashed organic samples:

1. **Sieving:** Creation of a sample slurry, sonication and sieving into several size fractions, followed by gentle drying, for example by a heat lamp.

2. **Flotation:** Slurry of sieved sample and heavy liquid (polytungstate, $\rho = 3\,\text{g/mL}$). Volumetric ratio sample to liquid about 1:5. Centrifugation, vacuum filtration (mesh size $< 1\,\mu\text{m}$ or as small as possible), gentle drying of the filters.

3. **Filter Preparation:** Careful breakdown of the heavy fraction filter using a small window Geiger counter, tweezers and if necessary an optical microscope. Separation of local concentrations of activity that might be particles, preparation of SEM sample holders with conductive carbon tape. Ideal: Fixation of only a single nuclear fuel particle onto a sample holder, without further inactive particles or filter fibers. Careful not to press particles too deep into the carbon tape. Use tape as thin as possible.

4. **SEM:** Particle search in LV mode with BSE and EDS, whilst making use of the micromanipulator W needle for contrast adjustment. Quick scan over whole carbon tape with low magnification, repeat with increasing magnification until particle found. Take several images in different magnifications per particle, to allow better navigation based on such images for later analysis or extraction. If particle cannot be extracted, take HV images and EDS spectra for cataloging.

5. **Extraction:** Prepare sample holder in angled position, use LV mode for first contact. Choose a W needle suitable for the individual particle (mostly depending on size) and test particle accessibility. Cover needle tip in glue (as much as necessary, as little as possible), then create contact between particle and needle. Adjust *acceleration voltage* (30 kV) and electron beam *spot size* (Philips XL30: 6 to 7) for high beam currents.
Focus on the glue between particle and needle at high magnification, monitor changes in GSE mode. Scan over the glue for several minutes and/or until no further "movement" is visible in the glue, then extract the particle.

3.8.4 Particle Search Discussion

Including related B. Sc. theses, 57 uranium particles were identified by SEM and EDS, all of which coming from soil and sediment samples from different regions within the CEZ.

The combination of high uranium content and local origin suggests, that these particles are in fact spent nuclear fuel fragments from the destroyed reactor in Chernobyl. Up to this point though, this remains a only highly plausible assumption and further proof is needed. The exact particle search and identification process was constantly revised and developed during this work, until a final optimized routine was suggested. To allow thorough analysis of individual particles, 18 of the most promising ones were extracted and mounted to custom made tungsten needles.

Sample preparation in terms of reducing the sample size by sieving and flotation proved to be key in the final process, as it greatly increased the concentration of particles in the remaining material. With the sample size reduced this way, larger particles of $> 10\,\mu m$ can be directly searched for with the SEM. An intermediate step of scanning with a small window Geiger counter can further narrow down the SEM work necessary. This however is strongly dependent on particle and background activity.

If smaller particles of $< 10\,\mu m$ or even sub micron sized particles are of interest, or if the sample shows high γ or β background activity, searching with the small Geiger counter does not work. At this point, ATD returns to be of use. It is only sensitive to α radiation and hence can be used to identify particle locations in high background areas, for example in samples with high concentrations of organic material containing ^{137}Cs. For small and low activity particles, ATD exposure time can be extended to several days or even weeks to detect more tracks and narrow sample material for SEM search.

For particle extraction, several types of needles are usable. Commercial options are available with tip diameters down to a nm area, capable of handling smallest particles. These are often composed of an extremely fine tungsten wire stuck to a larger wire made of another material, that is used for handling the needle. In this work, custom needles were crafted out of a single piece of W wire by chemical etching.[Hanemann 2019] This resulted in sturdier needles, making it easier to handle larger particles. It also allowed using these in the later chemical leaching experiments, since the W material is capable of resisting even concentrated HNO_3 due to a passivizing oxide layer on the surface. With the larger needle tips however, a sparing utilization of the glue is crucial to avoid covering the particle with it.

In conclusion, the particle search and extraction process as presented here became efficient after much optimization. Finally, the particle extraction was the most crucial step in the process and necessitated the most thoroughness and carefulness.

Suggestions for Future Developments

Use thinner carbon tape Thinner carbon sticky tape could reduce the effect of particles sinking too deep into the glue layer of the tape, which sometimes leaves particles impossible to extract without also taking up large chunks of carbon tape.

Use liquid N$_2$ during flotation This has only been tested at the end of this thesis: when separating heavy and light fraction after the flotation and centrifugation, freezing the bottom of the centrifuge tube - and with it the heavy fraction - allows to simply flush out the light fraction with DI-water instead of scooping it out.

More precise sample preparation for SEM For example by using pieces of carbon tape as small as possible, which would reduce the amount of time used in SEM for particle search.

Optimize W needle etching The quality of used micromanipulator needles was a large factor in how easy the extraction of individual particles was.

4 Particle Analysis

This chapter is focused on more conventional methods of particle analysis that could be done on extracted particles without removing the needles from their designated sample holder. The speciation methods, in this work beamline techniques as well as chemical leaching, are presented in individual chapters, as the underlying processes require more detailed discussion. Furthermore, such methods were applied to a limited number of particles because of resource and time restrictions.

4.1 Experimental Process

The process of full particle analysis started with general imaging by LV-SEM and EDS after locating the particle. This was done for every single particle that was found and repeated in HV-mode after particle extraction for higher quality images. In some cases, an optical microscope was used to take photos of individual extracted particles.

All extracted particles were measured on a γ detector to quantify their contents of ^{137}Cs, ^{241}Am and ^{154}Eu. This was also tested on some unextracted particles, but less frequently because of the possibility of interference from other sources within the sample, for example organic materials or shell fragments.

To confirm that individual particles originated from the RBMK-1000 nuclear reactor in Chernobyl, mass spectrometric methods were used to measure the isotope ratios of uranium and plutonium. Since subsequent speciation analysis was intended for most particles, all methods of mass spectrometry had to be non-destructive. Hence, static TOF-SIMS and resonant laser SNMS were chosen for isotope ratio analysis. A scheme of the applied workflow of techniques is displayed in figure 4.1.

Fig. 4.1   A schematic of the non-destructive sample analysis scheme:

4.1.1 Imaging and EDS Analysis

Investigated particles were rated as fuel fragments or *hot particles* only after imaging by SEM and confirmation of U as a main component by means of EDS analysis. Figure 4.2 represents an example of electron microscopy results in the form of an image and an EDS spectrum, which proves the U content of the analyzed particle. The dimensions measured using this image were then used to estimate particles' diameter. Its volume could also only be estimated, as its exact shape and thickness was unknown.

(a) SEM Image of CP-004 (SE+BSE overlay)

(b) EDS spectrum for CP-004
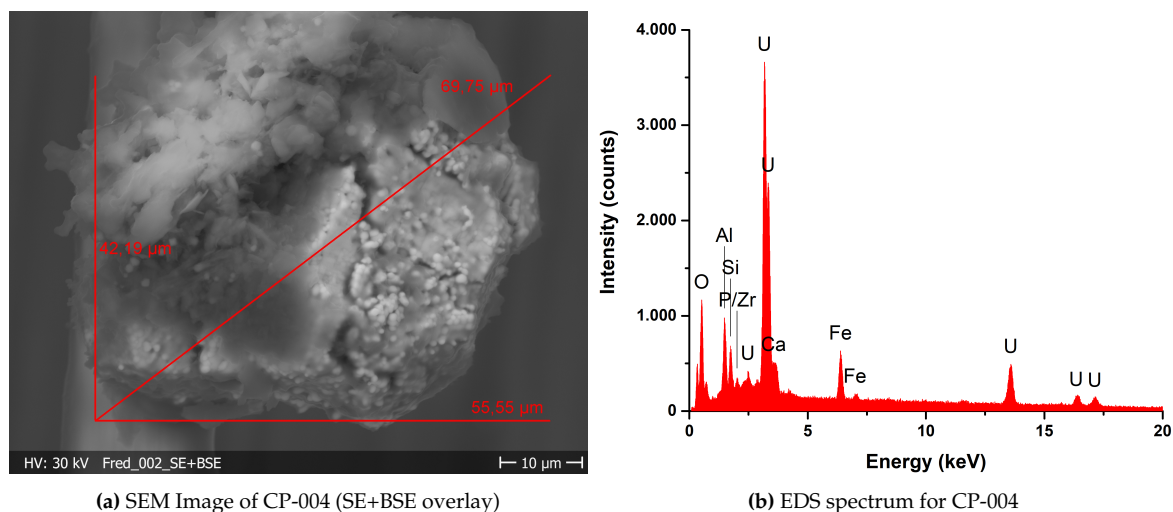
Fig. 4.2 CP-004 imaging and EDS analysis:
An exemplary image of an analyzed particle (CP-004). Subfigure 4.2a shows an SE+BSE addition image (for enhanced contrast) and includes size measurements. Subfigure 4.2b displays an EDS spectrum for the same particle, which proves U to be the main component of the particle. However, no Pu or other minor radionuclides can be identified using this method.

The uranium signal on its own only proves the presence of U, which is only an indicator, but not proof, for a nuclear fuel origin, since uranium is a naturally abundant element. To prove its origin, the isotopic composition has to be determined, which is not possible by means of EDS analysis.

4.1.2 γ-**Spectroscopy**

Each extracted particle was measured with a High Purity Germanium (HPGe) γ detector as part of the Ph.D. thesis of RAIWA[Raiwa 2021]. To ensure comparability of the results, a custom adapter was crafted[Bosco 2020], which could be fixed onto the Ge detector crystal with the needle holders mounted in a reproducible position, particles facing the detector in always the same distance. The adapter also featured an indentation to mount point-type calibration samples in the same position and height as the particle, to allow calibrations with reasonable margins of error. An example particle spectrum is given in figure 4.3:
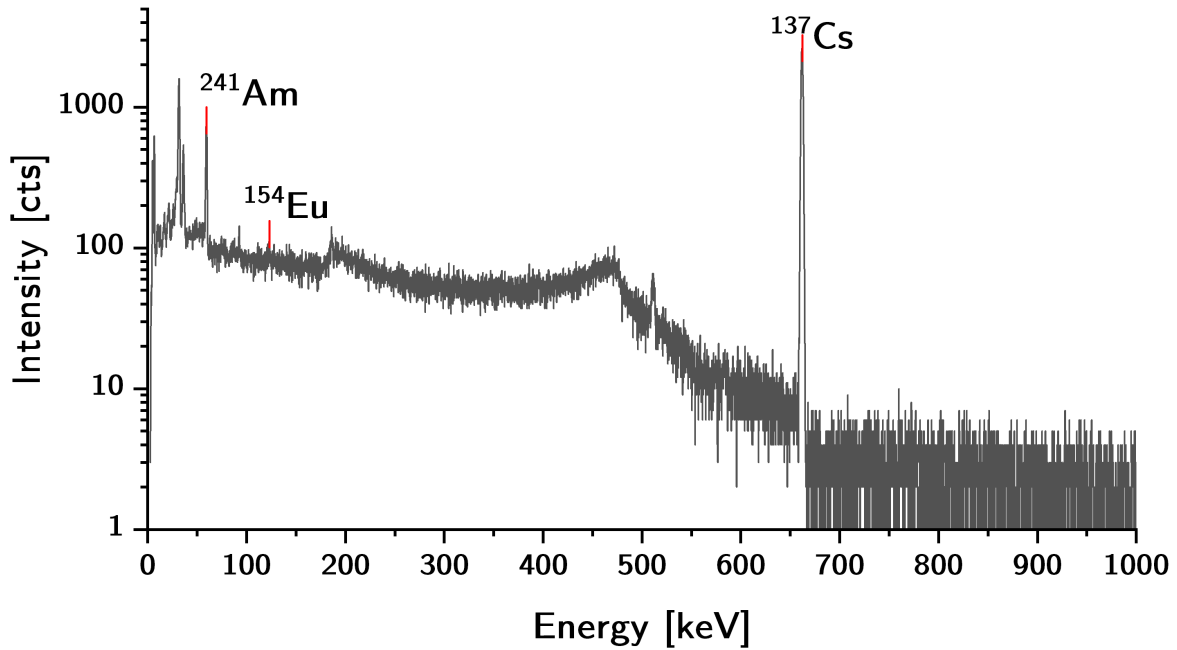
Fig. 4.3   Example particle γ spectrum:
Measured from the particle KOP-011 after dissolution, the red marks indicate the expected peak positions of the three γ relevant isotopes ^{241}Am, ^{154}Eu and ^{137}Cs. All three peaks are clearly visible and could be quantified.

This exemplary spectrum was measured as part of a later experimental series after dissolving the particle. During these experiments, several measurements were conducted, including the full particle before dissolution. The spectrum presented in figure 4.3 shows the same three isotopes that could be quantified within most particles: ^{241}Am, ^{154}Eu and ^{137}Cs. Calibration standards for particles were point-sources of the respective isotope provided by PTB. Solutions resulting from particle dissolution were calibrated using a multi-element liquid standard supplied by Eckert&Ziegler. The measured energies as well as data about the individual standards are summarized in table 4.1, the respective certificates are attached in the appendix. All development around particle γ spectrometry and more extensive results can be found in cooperating dissertations[Raiwa 2021],[Schulz 2020].

Tab. 4.1 γ **Spectrometry analysis data:**
Three major isotopes could be quantified in almost every particle, with ^{137}Cs as the main contributor to γ activity. Listed here are the utilized energy lines and standards for each isotope.

Nuclide	Energy	Standard
^{137}Cs	661.66 keV	PTB 569-81 Am241-07
^{241}Am	59.54 keV	PTB 246-83 Cs137-06
^{154}Eu	123.07 keV	PTB 228-94 Eu-152-03
Solution		7601ML (xQCY-13)

4.1.3 Mass Spectrometry

To investigate minor elements like plutonium, americium or strontium as well as isotopic ratios, mass spectrometric methods were necessary. Since non-destructiveness was mandatory, standard methods like Inductively Coupled Plasma Mass Spectrometry (ICP-MS) were not applicable. Of the available range of techniques, only Time Of Flight Secondary Ion Mass Spectrometry (TOF-SIMS) and its SNMS-variation could be applied.

During the beginning of this work, basic SIMS analysis and imaging was conducted on non-extracted particles still glued to some kind of solid surface. After electron microscopy and micromanipulation became available, the focus of the work shifted towards imaging and chemical speciation instead of mass spectrometric analysis, hence more research and in-depth results about SIMS and SNMS on particles can be found in related works[Bosco 2020][Raiwa 2021].

SIMS

The particle CP-001 was the first to be found and identified during this work. It was first located by ATD, via a combination of microscopic photos of the α track detector and the reduced sample (see section *Sample Preparation*, esp. figures 3.6 and 3.7). Microscopic imaging of the α tracks allowed a triangulation of the particle to a small area of only a few 100 μm, rendering a particle search via SIMS feasible. Being part of the early process of method development, the sample was glued to Al foil using a non-conductive epoxy resin, a round disk of 3 mm diameter of that sample containing the particle again was glued to a small Al block. This block was then mounted into a standard backmount sample holder of the SIMS and prepared for analysis.

Since a 3 mm disk is - in SIMS terms - a very large area that would take an excessive amount of time to scan completely, the analyzed area was confined to the previously narrowed-down area that should contain the particle. Navigating to this area within the SIMS was possible with the built-in camera, although relatively difficult since it is mounted at an angle to the vertical microscope that was used for triangulation.

In order to locate the particle, the instrument's *spectrometry* mode was used, which yields higher mass resolution and signal intensity, at the cost of lateral resolution. As the actual size of the particle was unknown, small scanning window sizes of about 50 μm to 100 μm were chosen, with around 100 scans per window to accumulate sufficient signal. From the only particle found in a preceding work[Hamann 2017], it was known that larger scan windows would bury the U^+ signal with high backgrounds. It was also known, that the oxides UO^+ and $UO_2{}^+$ should also be monitored, as they could provide an increased signal-to-background ratio

compared to the element.

Spectrometry mode: The spectrometry mode was the default analysis mode of the used SIMS instrument. It is optimized for high mass resolution and provides a lateral resolution in the few µm range. As a high mass resolution is necessary to distinguish between background and analyte signal, this mode was chosen for the initial particle search and for isotope ratio determination. It also provides relatively high signal intensity, so that individual scans could be measured reasonably fast. For the particle search, this was another necessity, as the horizontal location of the particle was roughly known, however due to the method's high sensitivity to topography, each scanning window had to be repeated in several sizes and vertical distances to close in on the particle.

To identify the particle, signals of $^{238}U^+$ at 238.1 m/z, $^{238}UO^+$ at 254.1 m/z and $^{238}UO_2^+$ at 270.1 m/z were monitored in the spectrum and at the same time in 2D mappings. Due to the mass-defect of heavy elements, the masses of the individual uranium isotopes are shifted slightly above the nominal masses (see figure 4.4). This effect allowed easier distinction from mostly organic backgrounds, which were highest on the nominal masses or shifted to the left.

For final analytical measurements, mass resolution, calibration as well as scanning window size and vertical position were optimized. In addition, a Region of Interest (RoI) was defined based on the $^{238}UO_2^+$ intensity, which included only the particle area despite the rectangular scanning window. Relevant measurement parameters for the final analytical measurements are summarized in table 4.2.

Fig. 4.4   SIMS spectrum - 238 U vs. background:
The uranium signal is shifted to the left of the nominal mass of 238 U and hence separated from the background.

Fast Imaging mode: In contrast to the spectrometry mode, Fast Imaging yields increased lateral resolution of down to 70 nm at the cost of mass resolution and signal intensity. Hence it was used after the particle was located exactly and optimized measurement windows and heights had been established. Spectrum quality was additionally improved by applying delayed extraction, no RoI was used. Measurements in this mode took longer due to higher pixel counts and lower signal yield, but allowed clear imaging of several elements, with focus on zirconium and uranium.

Tab. 4.2 Parameters of CP-001 SIMS analysis:
Listed parameters were used for the final SIMS measurements on particle CP-001. Further development and optimization of SIMS methods on fuel particles can be found in Raiwa 2021.

Parameter	Spectrometry	Fast Imaging
Species	Bi_3^+	Bi^+
Energy	30 keV	30 keV
FoV	60 μm × 60 μm	80 μm × 80 μm
Raster mode	random	random
Raster size	256 × 256 pixels	2048 × 2048 pixels
Polarity	positive	positive
Cycle time	100 μs	65 μs
Scans	100	30
Shots/pixel	1	1
Exemplary filename	Spec_MiN006b_2_07_U Roi.ita	FI_DE_MiN006b_2_03_Recalc.ita

SNMS

SNMS measurements were not a direct part of this work, but instead were successfully conducted by affiliated projects[Bosco 2020][Raiwa 2021][Bosco et al. 2021] on particles resulting from this work to increase the pool of analytical data per single particle. Since SIMS was limited to major elements due to high background interference, it could only provide indications of minor actinides like plutonium, however no actual proof for its presence within the particles could be claimed. By discarding the original SIMS signal and instead measuring resonant and non-resonant signal resulting from laser ionization, background interference was greatly decreased and minor elements like Sr, Pu and Am were identified. This method additionally allowed the calculation of isotopic ratios with higher precision and hence better comparability to literature values.

4.2 Particle Analysis Results

The following section presents a summary of achieved results via the more conventional methods. It is limited however to the most exemplary results, further data can be found in the appendix.

Short Summary of Results: A large quantity of particles have been identified throughout this work and affiliated works, all of which were analyzed via SEM and EDS. Solely based on these techniques, all three particle categories described by SALBU[Salbu 2009] and KASH-PAROV[Kashparov et al. 1996] could be identified. Zr content could only be measured in 6 out of 57 identified particles, a differentiation between reduced and oxidized particles was possible based on their visible structure. Their actual oxidation states could not finally be verified by these methods. Only few mass spectrometric experiments were part of this work and are presented here. Each particle's nuclear reactor origin has been verified though, as part of affiliated projects by further SIMS and SNMS measurements, proving their plutonium content and uranium isotopic ratios to be typical for RBMK reactors like the Chernobyl reactor.

4.2.1 Imaging and EDS

Particle imaging became possible with the SEM and particle extraction. SEM itself yielded high resolution images with little distortion due to low vacuum modes and conductivity provided by the metallic extraction needles. Optical imaging was possible largely only after extraction since there was no way to distinguish between nuclear fuel and natural soil particles in optical microscopy. Due to the small particle sizes, image quality in optical imaging was inferior to SEM in every way, which is why it was skipped for most particles. An example is given in figure 4.5, which compares SEM and optical images of KOP-011, a particle which becomes more relevant later in this work. Distinctive surface features are clearly visible in the SEM image, however barely recognizable in the optical image, which in addition is disturbed by light reflections from the SEMglu. Differentiation between the particle and remains of carbon sticky tape is obvious in the SEM image and close to impossible in the optical image.

(a) Imaging by SEM (SE)

(b) Imaging by optical microscopy
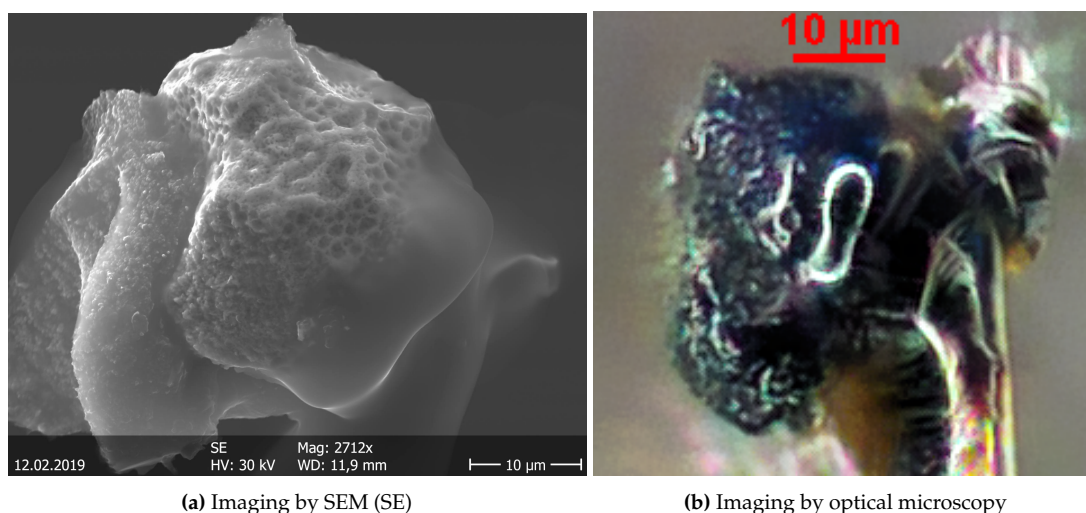
Fig. 4.5   SEM- vs. optical microscopy imaging:
The particle KOP-011 as imaged by SEM **(a)** and optical microscopy **(b)**. For particles in the µm size range, the optical microscopy was interesting to determine the particle's color. They are too small to see many details and proper lighting was difficult to achieve. The SEM image on the other hand allows easy differentiation between structures belonging to the particle and for example residuals of carbon tape or glue (left side in b). Additionally, SEM imaging gives high resolution images of the particle's surface, which can hint at information about the structure and becomes even more useful for chemical leaching experiments. Optical imaging was therefore largely skipped for smaller particles.

SEM Overview   In SEM analysis, a number of signals are available from a single measurement. A comparison between the different results is presented in figure 4.6, in which all images were taken from the same particle. The most obvious difference is visible between SE in 4.6a and BSE in 4.6b.

4.6c shows a surface contrast montage of the two images, which highlights the surface, however still suffers from the uneven illumination of the SE mode. Most final particle imaging was therefore done by using an overlay of SE and BSE as in figure 4.6d, as it yielded a good compromise between all modes advantages.

(a) SE image

(b) BSE image

(c) Surface contrast (SE-BSE)

(d) Enhanced contrast (SE+BSE)

(e) EDS measured area

(f) EDS spectrum
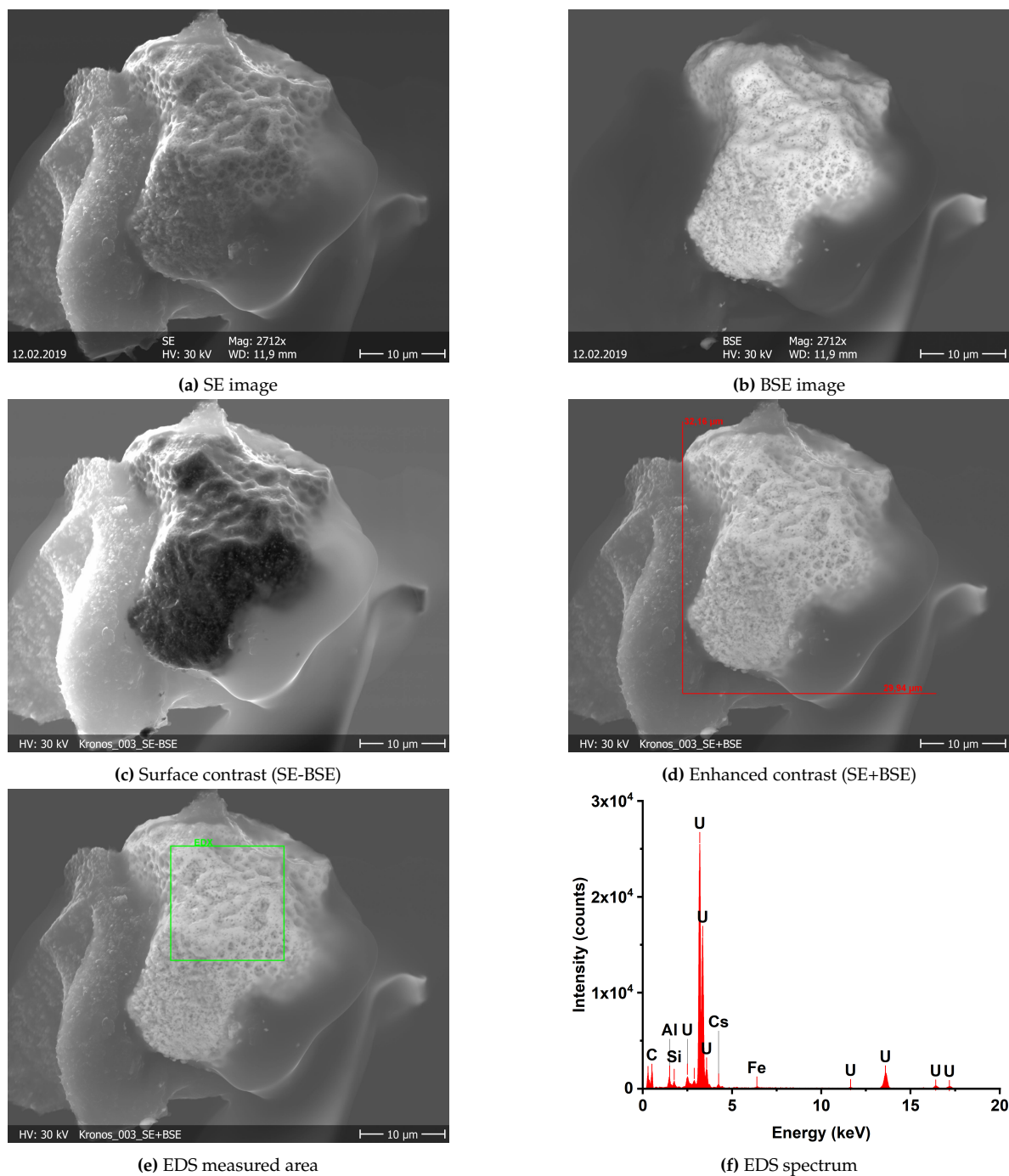
Fig. 4.6   SEM imaging results for KOP-011:
(a) A SE image of the particle showing surficial structures and morphology in high resolution. Particle, SEMglu and residuals of carbon sticky tape can only be distinguished based on changes in surface texture.
(b) The same particle in BSE contrast. High-Z materials like U and W appear brighter, making it easy to differentiate between particle and glue. Signal coming from the surface is now mixed with backscattered electrons coming from deeper within the particle, misrepresenting the surface texture.
(c) SE contrast with BSE contrast subtracted, correcting for the effect of backscattered electrons penetrating deeper into the surface.
(d) A contrast addition of SE and BSE imaging, enhancing the general image quality.
(e) The same image as (d). The area on which the EDS measurement was done is marked in green.
(f) An EDS spectrum as measured on the particle. Uranium is clearly represented as the main component of the particle, however no Zr is visible in this particle.

Particles with Zr:

Although only few particles containing EDS-measurable concentrations of Zr were found during the project, the very first one, CP-001, found in Chernobyl Cooling Pond sediment, was the one with the highest Zr content. Imaging and EDS results are presented in figure 4.7, showing an average EDS spectrum over the entire particle as well as a BSE image, that is perfectly reproduced by mappings of the U and Zr EDS signal. The particle has an oval shape and seems to be built up of many smaller, slightly spherical parts that were fused together. It contains major concentrations of Zr evenly distributed, with smaller amounts of U and the exceptions of one larger and few small areas of high U concentration.

(a) BSE image

(b) EDS spectrum

(c) U mapping

(d) Zr mapping
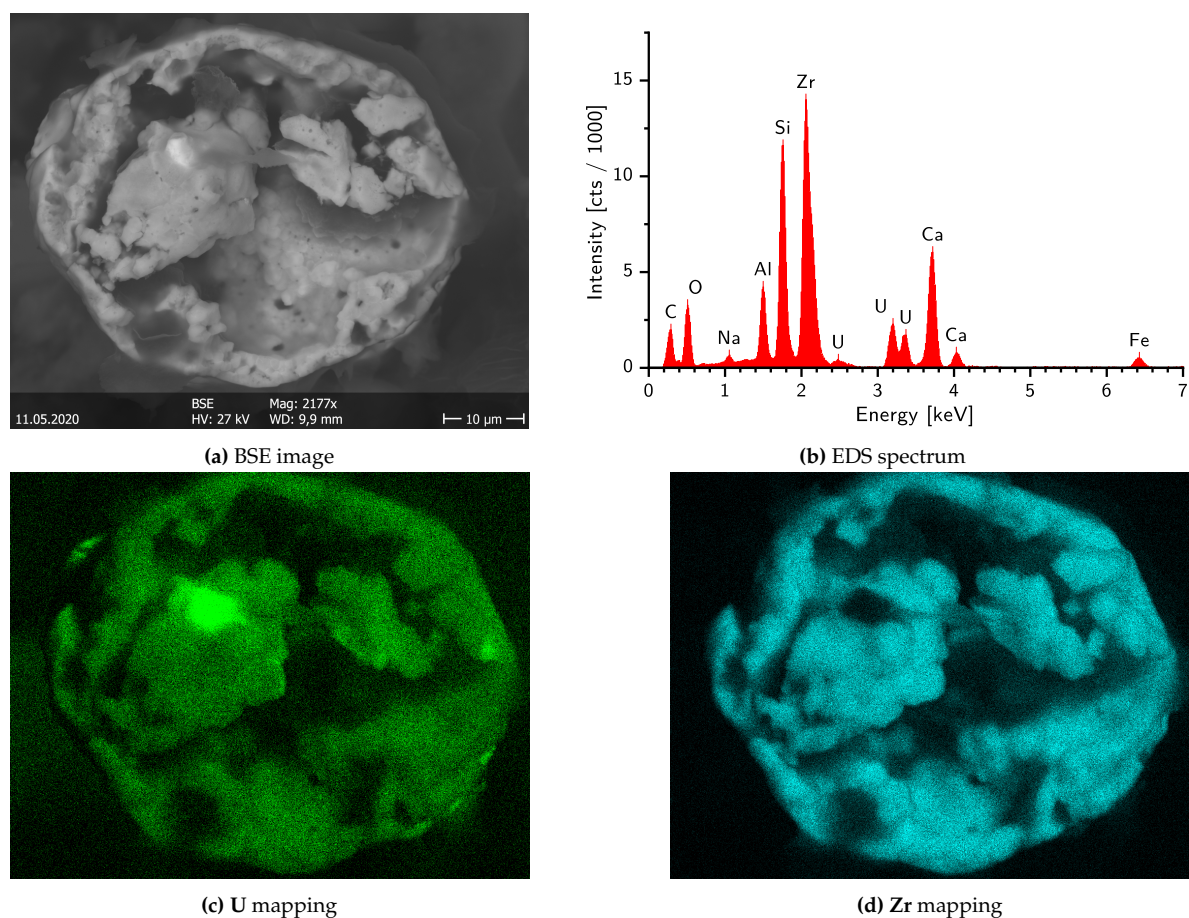
Fig. 4.7   SEM imaging and EDS of a Zr-containing particle:
(a) In BSE imaging, the particle seems significantly highlighted against the background. This effect is weaker than what would be expected from a particle consisting mostly of uranium though. One spot within the particle appears brighter than the average, hinting towards irregular U concentration.
(b) An EDS spectrum over the entire particle region, disregarding potential inhomogeneity of concentrations results in high amounts of Zr, with U signal being lower though clearly present.
(c) By mapping the EDS signal, U is found throughout the entire particle, with one large and several smaller spots of higher concentration. The larger spot is also visible as a brighter area in the BSE image 4.7a. **(d)** Similar to U, Zr is found in the entire particle, with a dark area only at the aforementioned region of increased U content.

Smooth Particles:

A second type of particles can be identified based on their relatively smooth surface without visible pores or crystalline structures. These appear to result from a melting process during the reactor explosion and the subsequent graphite fire. As an example for this type, sample CP-009 is shown in figure 4.8.

(a) SEM image of CP-009.

(b) EDS spectrum of CP-009.
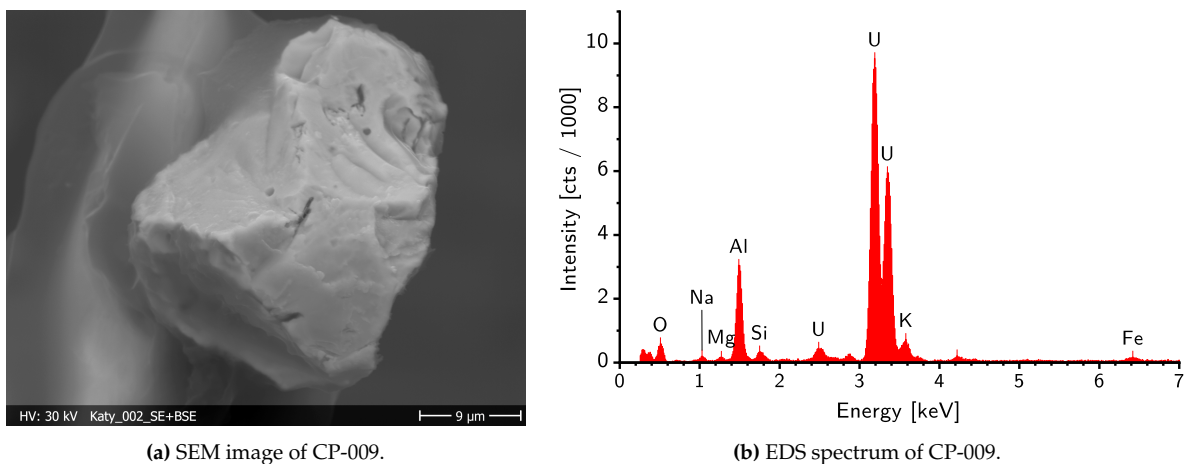
Fig. 4.8   SEM imaging and EDS of a second type particle:
(a) The particle has a relatively smooth surface, no pore structures are visible and no sharp crystal boundaries can be identified.
(b) EDS spectroscopy identifies high U, but no measurable Zr content.

Such particles do not resemble a typical nuclear fuel structure and the U content alone can not be considered sufficient evidence for this being a hot particle. During further analysis, U isotopic ratios and the presence of Pu within the particle were measured to ensure that it was actually of reactor origin.

Crystalline Particles

A third type of particle is classified by its porous structure and shows sharp edges resembling grain boundaries. CP-013 is shown in figure 4.9 as an example of this type.

(a) SEM image of CP-013.
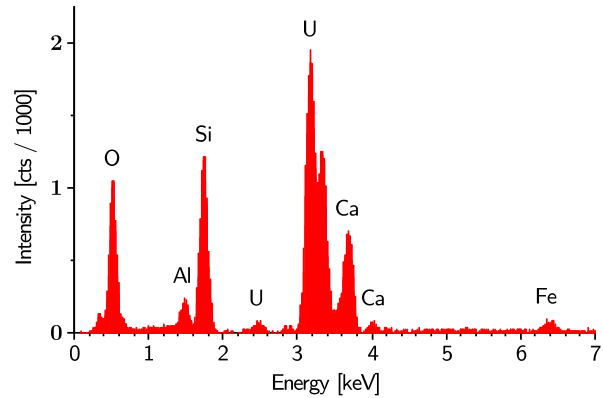
(b) EDS spectrum of CP-013.

Fig. 4.9 SEM imaging and EDS of a third type particle:
(a) In contrast to CP-009, this kind of particle is more comparable to what would be expected of spent nuclear fuel: high porosity and sharp edges indicating grain boundaries.
(b) A stronger influence of the surrounding matrix can be seen in higher O and Si signals. Again, U yields the highest signal and no Zr is visible.

The highly porous structure, with pores partly enlarged or even creating funnels is a strong indicator for spent nuclear fuel. The initial fuel is porous due to the pellet sintering process. Enlargement of pores and creation of funnels and holes in grain boundaries result from the release of fission gas during the burn-up process.[Rest et al. 2019]

4.2.2 γ Spectrometry

The isotopes ^{241}Am and ^{137}Cs could be quantified in each extracted particle, with activities ranging from 0.04 Bq to 221 Bq for ^{137}Cs and 0.01 Bq to 7.6 Bq for ^{241}Am. Additionally, smaller quantities of ^{154}Eu were measurable in fewer particles. Further evaluations can be by correlation of particle size, sampling locations and measured radionuclide concentrations and subsequent burn-up calculations and literature comparison. As all of these measurements were part of affiliated works, exact values for γ activities and more detailed information can be found in [Raiwa 2021].

4.2.3 SIMS Results

Presented spectra and images result from own measurements on CP-001 as well as examples from an affiliated work[Raiwa 2021] on KOP-011 for comparison. Since CP-001 has not been extracted from the surrounding matrix and is glued onto an Al surface by means of epoxy resin, it represents a particle mounting system that has since been superseded. It nonetheless serves as an example of SIMS capabilities and, in comparison to KOP-011, demonstrates the advantages of particle extraction.

In summary, each extracted particle and some non-extracted particles could be measured by SIMS. Extraction greatly improved the procedure of locating the particles with SIMS and reduced background signal and issues with low electrical conductivity. SIMS imaging was rarely used, since the quality and resolution of resulting images is inferior to SEM / EDS and the measurements are more complex. Details and comparisons between the different techniques are shown in the following subsections.

SIMS Spectra: Spectrometry vs Imaging

As described previously, spectrometry mode focuses on high mass resolution and was therefore used for particle search and isotope ratio determination. Imaging mode trades mass resolution for greatly enhanced lateral resolution and was used to monitor element distribution homogeneity throughout the particle. The differences in spectra measured on CP-001 are shown in figure 4.10. Both methods yield sufficient resolution and signal to clearly identify all isotopes of Zr and ^{238}U, however the minor isotopes ^{235}U and ^{236}U are not separated from background in imaging mode.
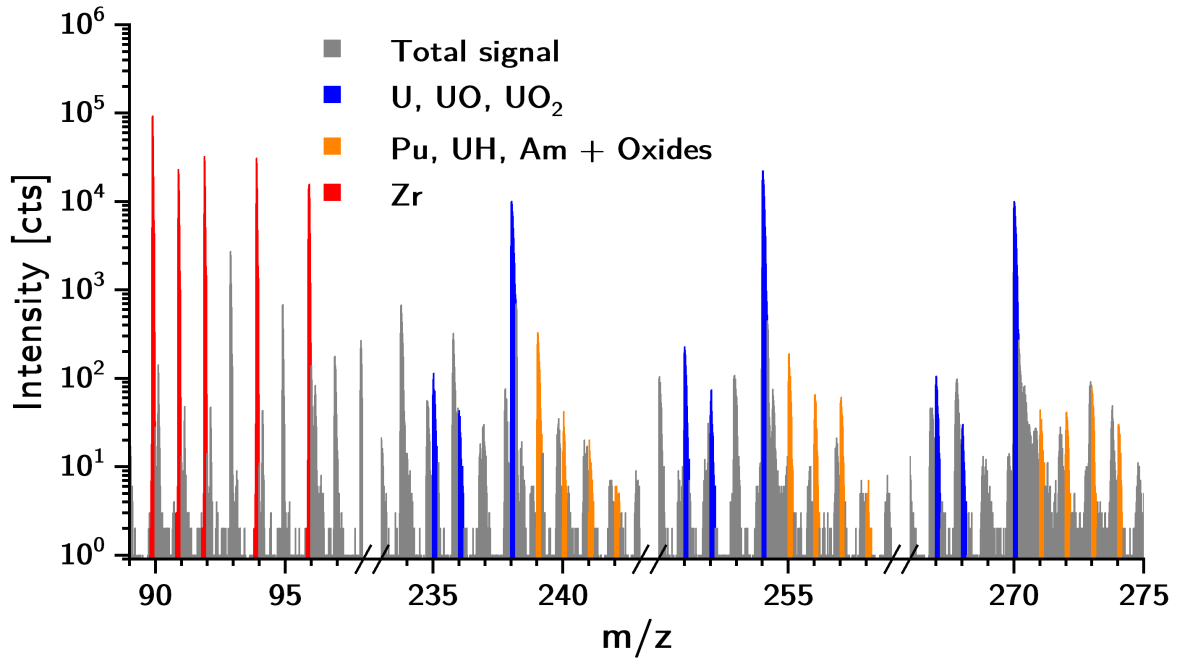
(a) SIMS spectrum of CP-001 in **spectrometry mode**.
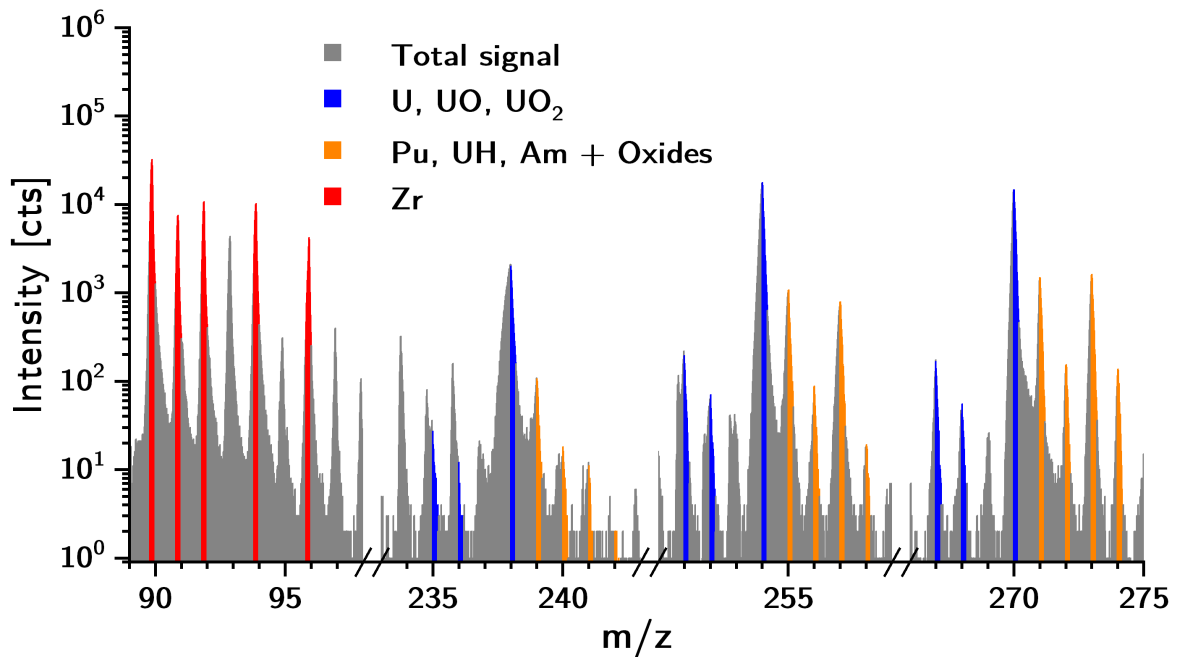
(b) SIMS spectrum of CP-001 in **imaging mode**.

Fig. 4.10   Comparison of SIMS spectra in spectrometry and in imaging mode:
Although the mass resolution in both modes is sufficient to identify Zr and ^{238}U, only spectrometry mode can also clearly separate ^{235}U and even hint on ^{236}U, both of which are concealed by background signal in imaging mode. Peaks on the masses of $^{239-242}$Pu are distinguishable in spectrometry mode, however are still prone to interference with ^{238}UH and ^{241}Am. ^{238}Pu is completely covered by ^{238}U signal and cannot be measured by SIMS.

SIMS Imaging

Figure 4.11 shows the result of a single SIMS imaging measurement. For the U and Zr mappings, all isotopes and the measurable oxides were added for enhanced contrast, figure 4.11d shows an overlay of the U map in green, the Zr map in red and the total ion signal over all masses in white.

When comparing such mappings to BSE imaging and EDS mapping as in figure 4.7, in terms of imaging quality and ease of use, SEM and EDS are far superior. The advantage of SIMS imaging is its higher sensitivity and selectivity on the isotope or molecule level. It can also be combined with SNMS to further reduce background and create mappings of minor actinides like Pu and Am, and subsequently compare their lateral distributions within particles.
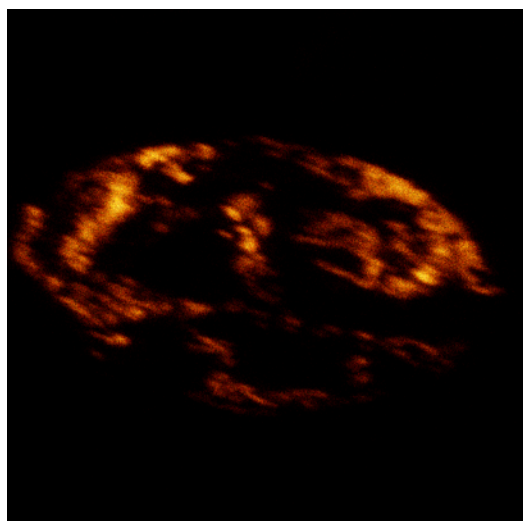
(a) SIMS **U** imaging.
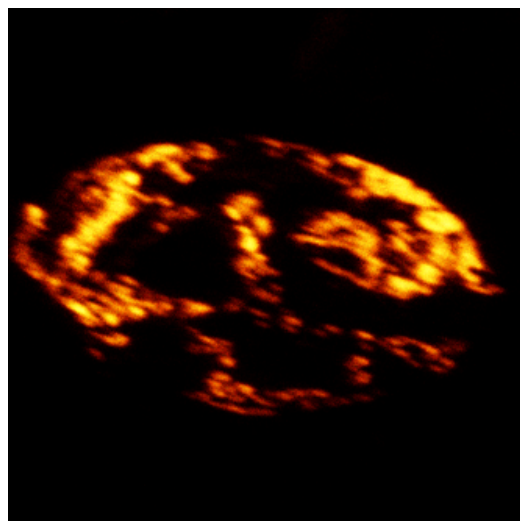
(b) SIMS **Zr** imaging.
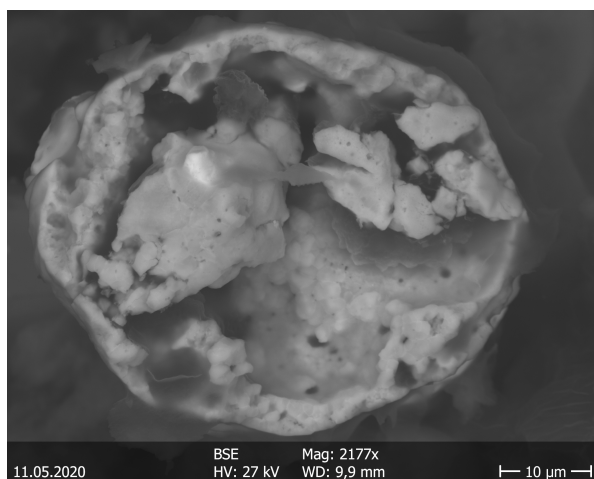
(c) BSE image.
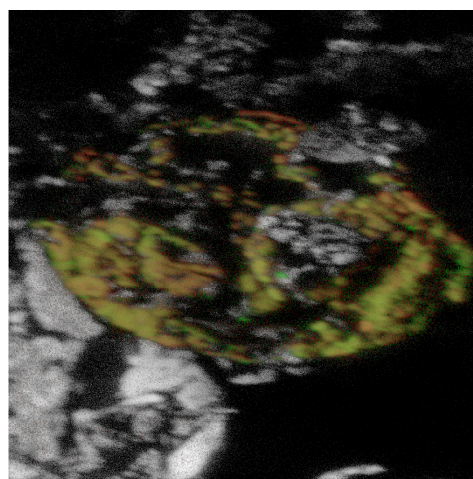
(d) Overlay of **U**, **Zr** and total SIMS signal.

Fig. 4.11   SIMS Zr and U imaging on CP-001:
Both mappings **(a)** and **(b)** show image additions for all isotopes and the oxides. This was done for contrast enhancement, however similar mappings can be constructed for each individual isotope. The more oval shape of the SIMS maps results from the uneven topography of the particle and the instrument's measuring angle.
(d) Signals are overlayed in green for U and red for Zr with the total ion signal from the entire measurement in white. Both signals clearly result from the same particle.
(c) A SEM image is added for comparison of imaging quality between SIMS and SEM.

SIMS after Particle Extraction

The first difference in SIMS analysis between extracted and non-extracted particles is the general ease of setup. Finding a particle, adjusting height and optimizing other analysis parameters is a quite cumbersome and time-consuming process for particles. When the particle is simply glued to the tip of a W needle, all of this becomes much easier and faster. The second difference is a drastic reduction of background and hence isobaric interference and improved mass resolution. A comparison of two full-scale spectra is presented in figure 4.12.
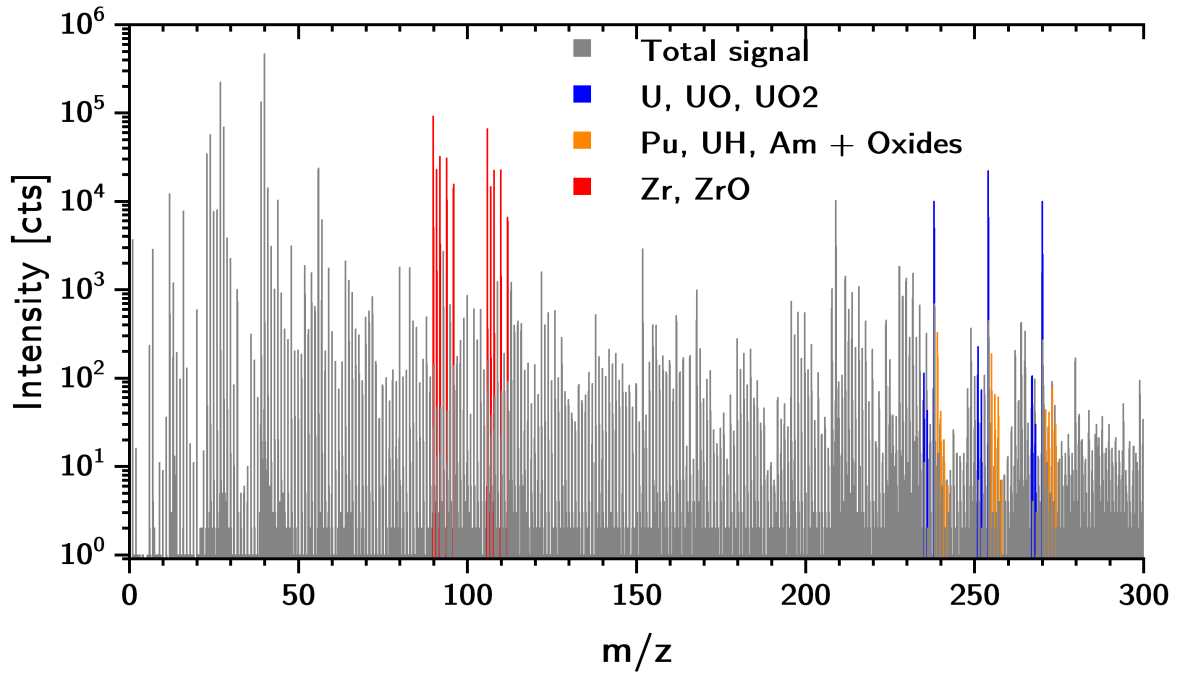
(a) Full SIMS spectrum of CP-001, **not extracted**, containing Zr.
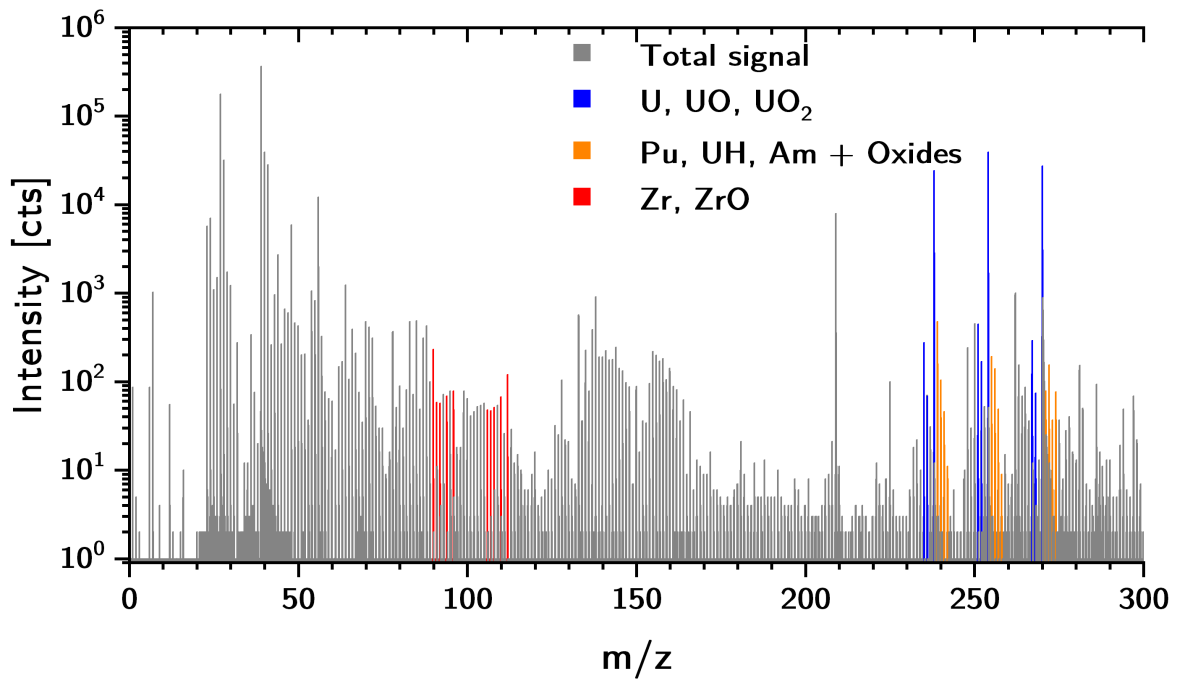
(b) Full SIMS spectrum of KOP-011, **extracted** by a W needle, no Zr visible.

Fig. 4.12   Full SIMS spectra of particles with and without extraction:
The two spectra presented here show the entire mass range that was commonly used for SIMS evaluation, from 0 m/z to 300 m/z. They also show the difference that extracting a particle before SIMS measurements can achieve. Although some common contaminants like ^{23}Na, ^{27}Al, ^{39}K and ^{40}Ca do yield similar intensities in both spectra, the average background is significantly reduced in (b) compared to (a).

The resulting difference in mass resolution becomes even clearer when comparing their relevant mass regions as shown in figures 4.10a (CP-001 not extracted) and 4.13a (KOP-011 after extraction). These spectra are from two different particles, but the enhanced spectrum quality can be observed for all extracted particles. Background interference, especially on the minor isotopes ^{235}U and ^{236}U, is significantly reduced. This allows better calculation of isotopic ratios as well as safer identification of other components of the particle.

4.2.4 SIMS vs SNMS

Since no SNMS measurements were done as part of this work, but only in affiliated projects, only one example is given here to demonstrate the potential of this technique. Figure 4.13 shows the previously used sections of a SIMS and a Pu-SNMS spectrum of KOP-011.
In the SNMS spectrum, the secondary ion signal in the Zr-range is suppressed efficiently. All U isotopes are reduced by several orders of magnitude in signal, whilst the Pu intensity is enhanced. Also visible is the suppression of Am on the mass 241. Extremely low concentrations of ^{238}Pu relative to ^{238}U present[Makarova et al. 2008] the strongest challenge for the method. It has been shown though, that suppression of ^{238}U is sufficient to validate the existence of ^{238}Pu within the particle without the use of destructive analysis.[Bosco 2020]
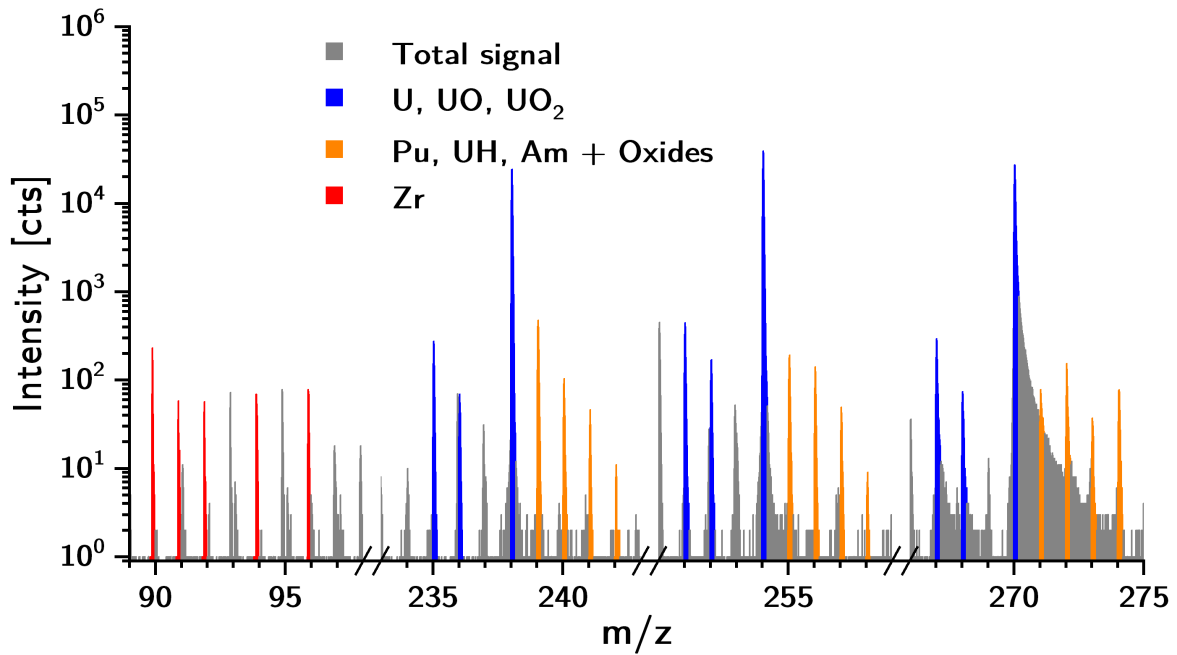
(a) SIMS spectrum of KOP-011.
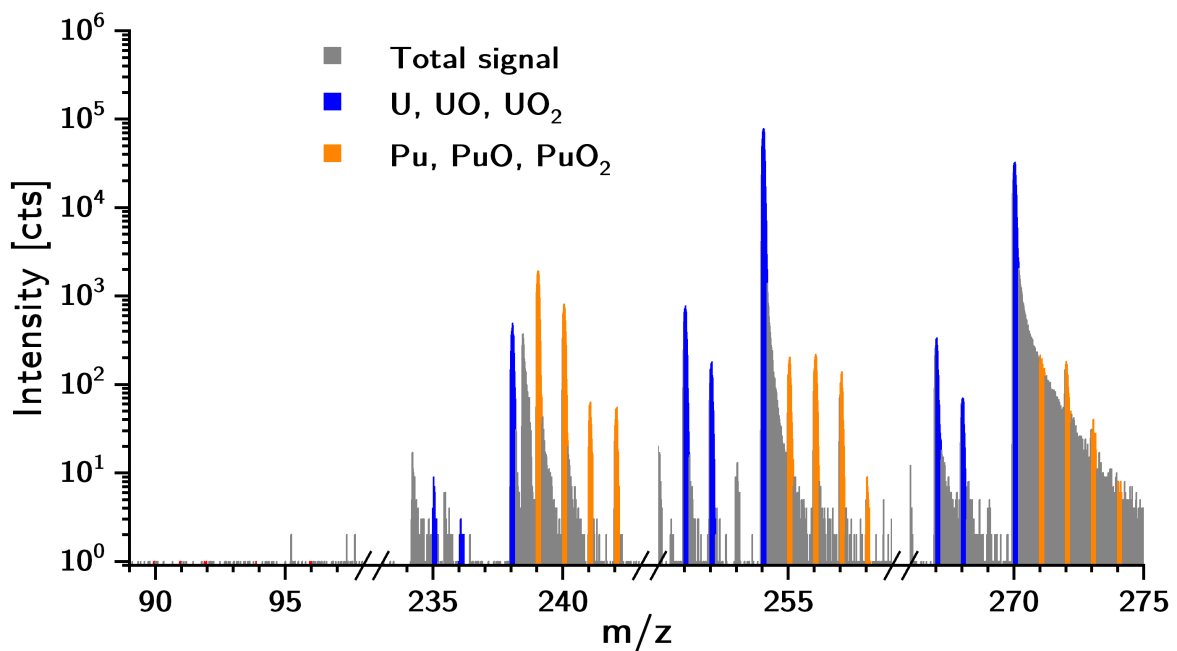
(b) Pu SNMS spectrum of KOP-011

Fig. 4.13 Comparison of SIMS and Pu SNMS spectra:
Although the mass resolution in SIMS is sufficient for determining U isotopic ratios, there is still potential background interference left on ^{235}U and especially ^{236}U and Pu cannot be distinguished from the background in (a).

SNMS in (b) leads to peak broadening, however the reduced mass resolution is more than compensated for by the elimination of background signal, here demonstrated in the lower mass range and by the greatly improved ^{238}U to ^{239}Pu ratio and elimination of the ^{241}Am isobar.

4.3 Particle Analysis Discussion

Summary: A wide array of non-invasive and almost non-invasive techniques has been applied to individual particles. Imaging and a loose categorization was done for each particle found during this work. Subsequent methods like SIMS, SNMS and γ spectrometry were mostly done by affiliated works, with few early exceptions, as presented in this chapter. Although such methods were available before, particle extraction to single needles has significantly lowered the boundaries for applying any methods after SEM imaging. Finally, by combining such non-destructive methods, a vast amount of data could be generated for each individual particle. SEM and EDS allowed the identification of U and Zr content and in some cases even classification as reactor material based on optical characteristics. γ spectrometry yielded quantification for relevant radionuclides, SIMS and SNMS was used to calculate isotopic ratios for U and Pu. After the entire process, all particles remained available for subsequent destructive analysis.

The aim of this thesis was the development of a non-destructive sequence of analytical methods for individual hot particle investigation. In this, it was fully successful. Although large parts of the actual analytical work was then shifted to affiliated works, proof-of-concept was given within the range of this project. Combining all the techniques described within this chapter yields data about dimensions and morphology of individual particles and their elemental composition. Also quantification of relevant radionuclides like ^{137}Cs and ^{241}Am and isotopic ratios of the U and Pu isotopes are available without inflicting chemical changes to the particle.

There are disadvantages to this way of particle analysis however:

Individual separation or extraction is necessary, requiring a significant amount of work and time for each single particle. For the instruments required, both electron microscopes equipped with EDS and γ spectrometers are widely available. A TOF-SIMS however is much more specific. The additional setup of lasers for SNMS and especially the expertise to operate this method is even rarer. In conclusion, the sequence of methods as described is relatively exclusive to the Institute of Radioecology and Radiation Protection (IRS) in Hanover, where this work was developed. The methods described so far also lack one analytical component, that was critical part of this project. To this point, only elemental and isotopic data are generated, though the chemical speciation of the particle's main structures remain unknown. As speciation analysis was another focus for this work, it is addressed in the following two chapters, first non-destructively via XAS and finally by sequential dissolution methods.

5 Beamline Analysis

The analytical techniques described in the previous chapters draw a comprehensive picture of an individual particle's chemical and isotopic composition. So far, using these methods, no data has been collected regarding the chemical speciation of U or Pu which is vital for predicting the potential for radionuclide leaching and mobility.[Salbu et al. 2004] One powerful method to investigate speciation properties like specific element's oxidation states is X-ray Absorption Spectroscopy (XAS), specifically XANES.[Nolf et al. 2010][Golosio et al. 2003][Bleuet et al. 2008] It can elucidate oxidation states and can yield a qualitative assessment of local atomic order. When using μ-focus X-ray analysis techniques, such results can be gained even from μm-sized particles.[Lind et al. 2005],[Salbu et al. 2001] Access to such techniques however is limited, as they require high-intensity X-ray sources like a synchrotron. All the measurements presented here were state of the art operations.

XAS measurements were conducted at the μ-focus X-ray Absorption Spectroscopy (μ-XAS) beamline X05-LA located at the Swiss Light Source in Villigen, Switzerland.[PSI 2009][Sanchez et al. 2017] A μ-XAS beamline was chosen, as it allows a high spatial resolution of down to 1 μm to 1.5 μm as well as 2D-tomography to reveal the particle's inner structure. Experiments included 2D μ-focus X-ray Fluorescence (μ-XRF)-tomography slices through the particles for several elements, μ-focus X-ray Diffraction (μ-XRD) mapping of 2D slices as well as μ-focus X-ray Absorption Near Edge Spectroscopy (μ-XANES) measurements for U and Pu of several individual voxels within the particles. Reconstruction and evaluation of the raw data were conducted separately.

Three particles were investigated at the beamline: CP-003, CP-004 and BK-006, all of which had previously been extracted and mounted to individual W needle tips. As subsequent chemical leaching experiments were planned, a special confinement had to be crafted to allow retrieving of the particles later and at the same time guarantee safety at the beamline. For this purpose, a tube of X-ray transparent Kapton tape was wrapped around a Plexiglas cylinder that held the needle. This way the particle was fully encased, but not stuck to the tape whilst maintaining the uncomplicated handling of the needle. Figure 5.1 shows a schematic of the containment.
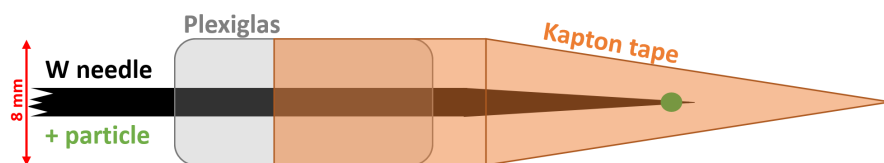
Fig. 5.1   Containment of the W needle for beamline experiments:
A Plexiglas tube, glued to the needle, was used as spacer, around which X-ray transparent Kapton tape was wrapped. This hollow cylinder was then closed at the top, enclosing the particle without touching it. This way the tape cap could be removed later on and the particle on its needle reused for other experiments.

Figure 5.2 shows a photo of the sample as set up in the beamline. The W needle is mounted onto a sample holder, that can be rotated to measure single voxels within the particle. As part of the setup process, the needle had to be positioned to center the particle in a rotational axis, since the particle-needle-constructions were not symmetrical.
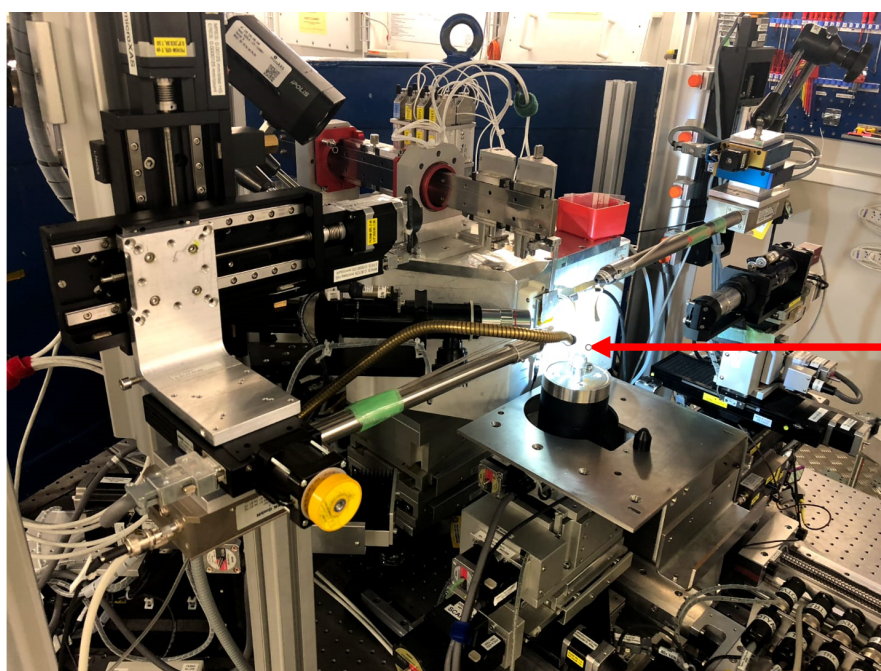
Fig. 5.2   Photo of the beamline experimental setup:
In the photo, the sample is already set up in the sample manipulator. Its location is indicated by the red arrow, since the bright lights make it hard to see the sample itself.

The absorption edge energies used in XRF and XANES experiments are listed in table 5.1. Zr and Y thin foils were used as energy calibration standards for Pu and U, respectively. W was measured to show the needle tip, Fe was included to show the Fe layer around CP-004 and Sr to investigate another potentially detectable radionuclide.

Tab. 5.1 **Absorption edges used for beamline XRF:**

Element	Edge	Energy
U	Lα	13.614 keV
Pu	Lα	14.276 keV
Sr	Kα	16.105 keV
Zr	Kα	15.775 keV
Fe	Kα	6.405 keV
W	Lα	8.398 keV
Y	Kα	14.958 keV

5.1 Experimental and Evaluation Process

To locate the particle itself for analysis, the XRF signal of the W needle was used and followed to the tip, where the particle could be identified based on its uranium signal. Additionally, it was used to adjust the correct rotational focus on the particle so ensure it to spin on its axis without moving in the horizontal plane, which was vital for tomography measurements. From that point on, all described experiments were performed before switching to the next particle. Because it provides the most accessible graphical overview, XRF was the first method applied. Based on the created XRF maps, spots for μ-XANES measurements were chosen, whilst μ-XRD was measured last.

5.1.1 μ-XRF mapping:

For each of the three particles, μ-focus X-ray Fluorescence (μ-XRF) maps were created for six elements: U, Pu, Sr, Zr, Fe and W. All respective edges and energies are listed in table 5.1. The main interest was the identification of potential Pu *hot spots*, which would yield the highest possible signal intensities for XANES measurements. Additionally, mapping revealed inhomogeneities of elemental concentrations within the particle. Evaluation and creation of the resulting elemental maps involved sorting through a number of scans per particle and discarding corrupt data sets. Initial scan sorting was done via FDA, a program provided by the beamline, creation of the final maps then was done in PyMCA (see below).[Schroer 2001]

Special software used for XRF evaluation:

- FDA (provided by beamline)
- PyMCA[Solé et al. 2007]

5.1.2 µ-XANES:

µ-focus X-ray Absorption Near Edge Spectroscopy (µ-XANES) scans were collected from several 'hot' spots on each individual particle, scanning energies across the U and Pu L_3 edges. The purpose of these measurements was the investigation of potential differences in oxidation states of U and Pu respectively, especially gradients between the inner particle core and the outer shell. The measured spots are shown in figure 5.7 in the results section. For energy calibration, metal foils of Y and Zr were used for U and Pu, respectively. Reference edge energies are included in table 5.1. Reference XANES data for the oxidation states in question were kindly provided by LAW for U[Bower et al. 2019] and CONRADSON[Conradson et al. 2004] for Pu. Again, initial evaluation of scan quality was done in FDA, for preprocessing of the data XAS Viewer was used. Final energy calibration and data evaluation was done in Athena (see below).

Special software used for XANES evaluation:

- FDA (provided by beamline)
- XAS Viewer (Part of Larch)[Newville 2013]
- Athena (Part of Demeter)[Ravel et al. 2005]

5.1.3 µ-XRD:

2-dimensional tomography slices were mapped with µ-focus X-ray Diffraction (µ-XRD) through each particle with a resolution of about 1 µm at 18.0 keV and 18.2 keV. Simultaneously, 2D diffraction intensity maps were created, resulting in images composed of several hundred pixels, each corresponding to an individual XRD pattern. A visualization is presented in figure 5.3.

(a) Measurement of µ-XRD sinograms for tomography.

(b) Reconstructions from sinograms to µ-XRD intensity maps.
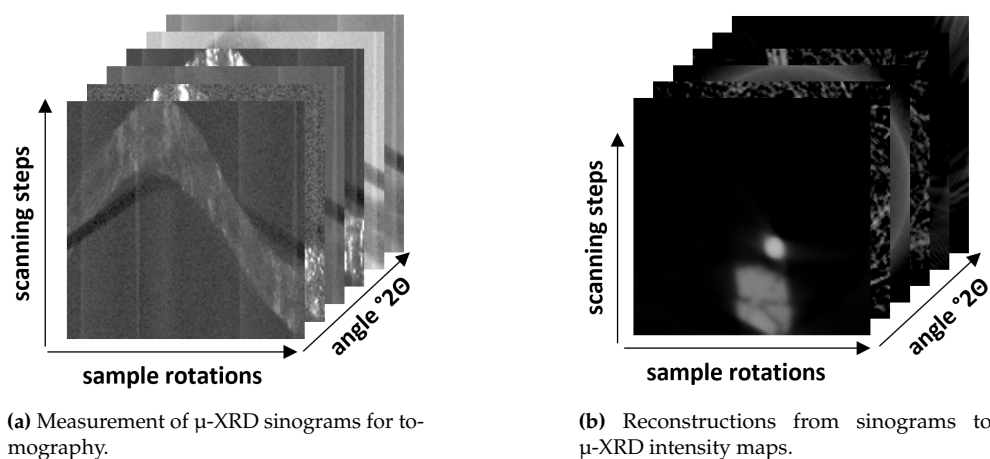
Fig. 5.3   Visualizations of the µ-XRD tomography reconstruction process:
To measure µ-XRD tomography, the particle is moved perpendicularly to the beam axis whilst simultaneously rotating. Measuring diffraction angles and intensities yields so-called sinograms[Bleuet et al. 2008], which can then be reconstructed into angle-dependent intensity maps. The depictions a and b are recreated after Sanchez et al. 2017 and contain more than 4300 individual sinograms for this single scan.

In addition to the single pixels, all patterns of each slice were summed up to create an average pattern, which was evaluated similarly to a powder-XRD pattern. These average patterns were compared to several references from the Crystallography Open Database (COD), to identify the crystal structure of the particles. As they are spent nuclear fuel, their main matrix was expected to be a uranium oxide, with U oxidation states between U(IV) and U(VI). Crystal structures representing these edge states would be UO_2 (uraninite) and UO_3, but also mixed oxidation structures like $UO_{2.12}$ U_4O_9 and U_3O_8 were investigated.

Conversion of raw data to readable XRD patterns necessitated an array of custom scripts provided by the beamline and publicly available software like Bubble and ImageJ. Pattern comparison and evaluation was then done in Match!3, with reference patterns from the COD. All reference patterns used are shown in table 5.2.

To additionally investigate crystallographic changes throughout each particle, individual pixel patterns were evaluated to compare outer layers to inner particle cores1. Images with the evaluated pixel indicated are shown in figure 5.12 in the results section.

Special software used for XRD evaluation:

- FDA (provided by beamline)
- Custom Python scripts provided by beamline
- Bubble[Dyadkin et al. 2016]
- ImageJ[Schneider et al. 2012]
- Match!3 by CrystalImpact in combination with the COD
- COD[Downs 2003],[Merkys et al. 2016],[Quirós et al. 2018]
  [Gražulis et al. 2009],[Gražulis et al. 2012],[Gražulis et al. 2015]

Tab. 5.2   **XRD reference patterns from COD.**

Structure	COD entry number	COD ID
$UO_{2.12}$	96-231-0515	2 310 514[Willis 1978]
$UO_{2.338}$	96-901-2196	9 012 195[Lauriat et al. 1989]
U_4O_9	96-231-0340	2 310 339[Belbeoch et al. 1967]
U_3O_8	96-231-0812	2 310 811[Siegel 1955]
UO_3	96-152-7744	1 527 743[Loopstra et al. 1977]
W	96-900-6488	9 006 487[Dubrovinsky et al. 1997]

5.2 Beamline Results

In summary, XRF mapping of two-dimensional slices for each particle was successful and showed relatively homogeneous distributions of elements within the particles.

Most of the measured μ-XANES spectra were heavily affected by a low signal-to-noise ratio, leaving most of the resulting scans with insufficient quality. Two U scans per particle were fit for evaluation, the Pu scans were too noisy for accurate determination of oxidation states. The reason for such low yield is presumably the low concentration of Pu as compared to U.

μ-XRD yielded hundreds of individual patterns, which could be compared to literature patterns. Averaged patterns were evaluated as well as a range of individual pixel patterns per each slice.

5.2.1 XRF mapping

Two-dimensional slices yielded elemental maps for six elements: U, Pu, Sr, Zr, Fe and W. These maps only represented element-specific information and no data about isotopic composition. Of the analyzed elements, only Fe showed actual hot spots in sample CP-004, the other elements appeared to be distributed relatively equally throughout the particles. These Fe hot spots were presumably a layer of small FeS cubes, that were abundantly found in Cooling Pond samples and are a product of the anoxic conditions in combination with microbial activity.[Schieber 2010][Mihály Pósfai et al. 1998]

In all images, an intensity gradient was visible: All elements seemed to have a concentration shift, rising in the same direction. This was a sample thickness issue, presumably resulting from self-absorption within the particle. Such a presumption is plausible since the absorption of high energy photons in nuclear fuel particles has been described in literature before.[Jiménez-Ramos et al. 2010]
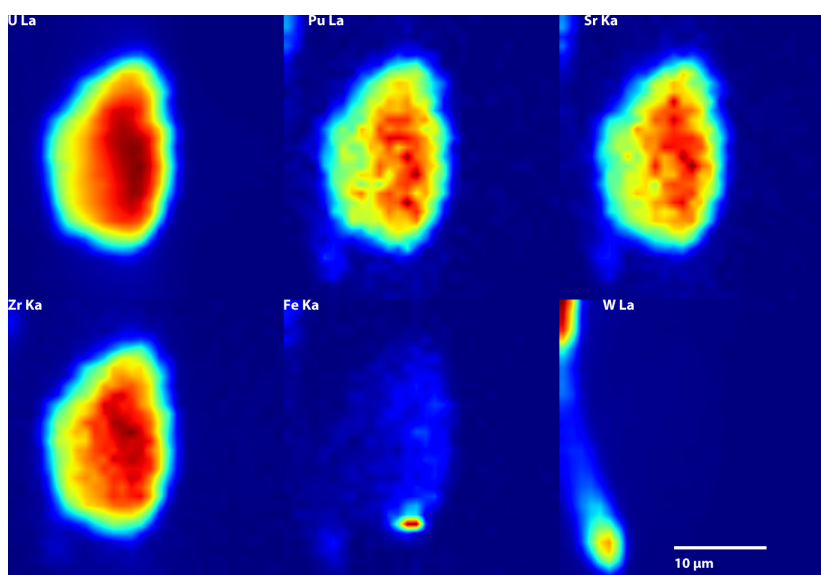
Fig. 5.4   Full particle XRF maps for sample BK-006:
Most investigated elements, with the exception of W and Fe (U, Pu, Sr, Zr), appeared to be relatively equally distributed within the particle. The visible gradient for the right direction resulted from self-absorption of the signal within the particle since only one detector was used. This would also explain the gradient always being from left to right.
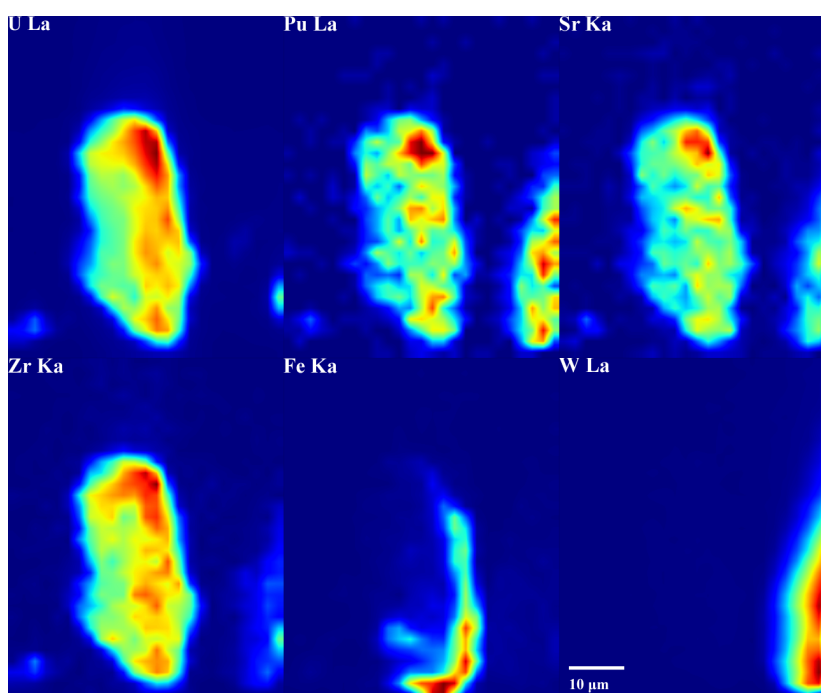
Fig. 5.5   Full particle XRF maps for sample CP-003:
A similar result to the XRF maps in image 5.4. Most elements seemed distributed in a spotty manner with an intensity gradient to one side, an artifact of not using tandem detectors. The visual non-uniformity of the intensities can be due to the irregular sample shape.
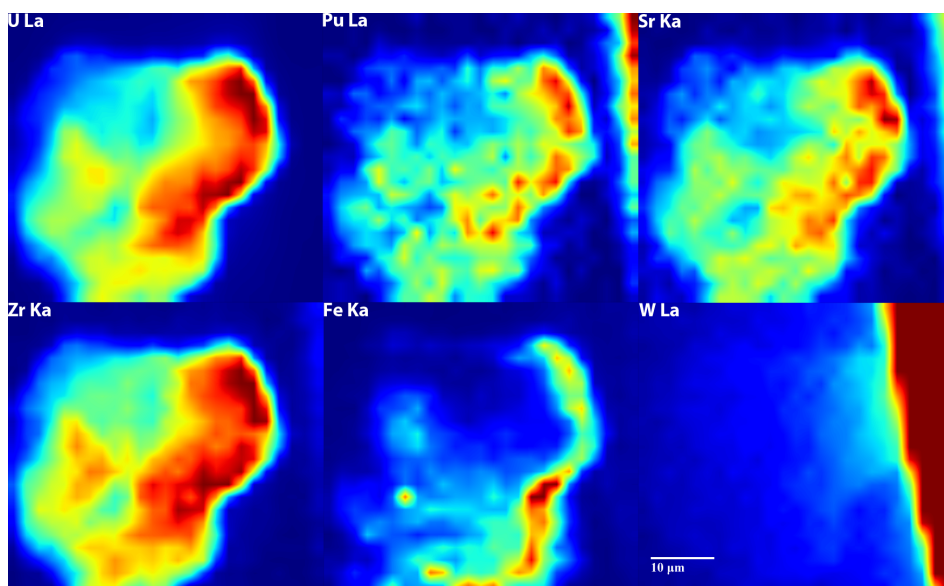
Fig. 5.6 Full particle XRF maps for sample CP-004:
The largest of all three particles shows the highest self-absorption effects, resulting in an even stronger gradient than the first two particles. An outer shell of Fe became visible, which probably matches an outer "crust" of small FeS particles already observed in SEM imaging[Schieber 2010][Mihály Pósfai et al. 1998].

5.2.2 XANES

µ-XANES measurements successfully yielded oxidation state information about U from several voxels within each particle. Spot sizes for these measurements were about 1 µm. The measured locations are indicated in XRF maps in figure 5.7, the resulting U XANES spectra are shown in figure 5.8.
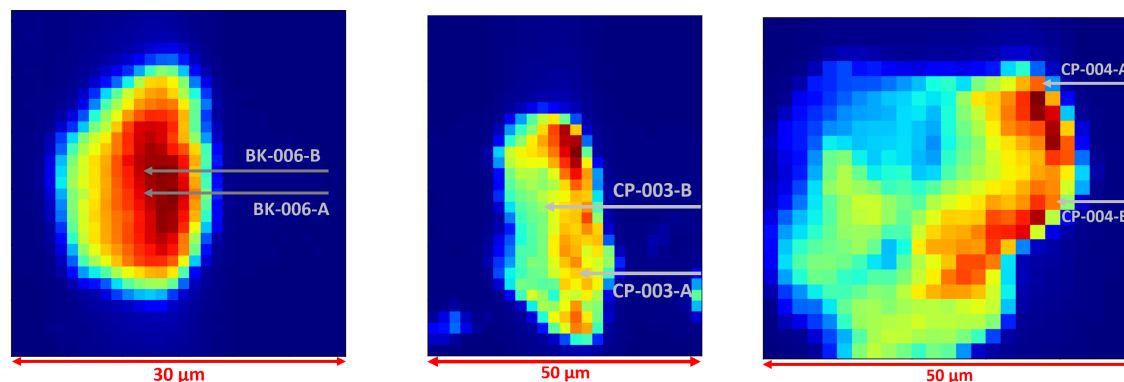
(a) Spots measured on BK-006 by µ-XANES.

(b) Spots measured on CP-003 by µ-XANES.

(c) Spots measured on CP-004 by µ-XANES.

Fig. 5.7   **U µ-XANES scan locations on the 2D tomography maps:**
Two µ-XANES scans per particle are presented in figure 5.8. Each scan was measured with an X-ray spot size of about 1 µm on the voxels shown in these maps.
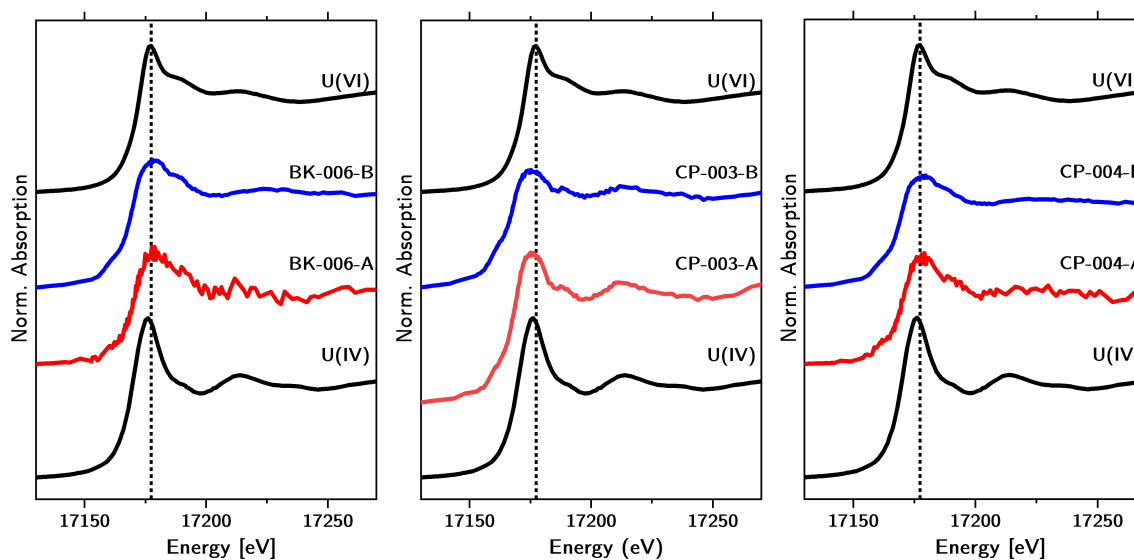
(a) U L_3 µ-XANES scans for BK-006.

(b) U L_3 µ-XANES scans for CP-003.

(c) U L_3 µ-XANES scans for CP-004.

Fig. 5.8   **U µ-XANES scans for 3 particles:**
Uranium µ-XANES scans for all 3 particles that were analyzed in the beamline. Due to low signal intensity, not all measured µ-XANES scans were of sufficient quality to evaluate. The displayed six scans however yielded useful results for the particles: CP-003 is clearly less oxidized compared to BK-006 and CP-004. Only two scans per particle were of sufficient signal quality for evaluation, both are presented as A and B.

Although the *A*-labeled scans are noisy, the trends in both scans are clearly distinguishable. The dotted line indicates the peak of the U(VI) white line, emphasizing the shift to lower energies in the U(IV) white line. A second difference is the shoulder on the higher energy side, which is elevated in U(VI) compared to U(IV).

Both BK-006 and CP-004 show the higher energy shoulder and match the white line peak of the U(VI). In contrast, CP-003 is shifted to lower energies and the shoulder is less pronounced compared to the other two samples. Based on these findings, it can be concluded, that CP-003 is at a lower oxidation state, presumably between U(IV) and U(V), whilst CP-004 and BK-006 are higher oxidized. Linear Combination Fitting (LCF) was calculated with these data, the results presented in table 5.3 quantify the relative proportions of both oxidation states and show clear trends for all three particles.

Tab. 5.3   LCF calcuation of the oxidation state ratios in uranium XANES measurements: Error margins of about $\pm$ 10 % are assumed for the results.[Kelly et al. 2008]

Scan	U(IV)	U(VI)	$\pm$	Comments
BK-006-A	42 %	58 %	$\sim$10 %	high noise, but more oxidized
BK-006-B	20 %	80 %	$\sim$10 %	clearly more oxidized
CP-003-A	68 %	32 %	$\sim$10 %	more reduced
CP-003-B	64 %	36 %	$\sim$10 %	broad white line, more reduced
CP-004-A	24 %	76 %	$\sim$10 %	clearly more oxidized
CP-004-B	21 %	79 %	$\sim$10 %	clearly more oxidized

The presented results show the continuous existence not only of reduced, but also of oxidized particles. Also, comparing the μ-XANES measurements from different locations, differences in oxidation state distribution throughout individual particles become visible. Such heterogeneity within the particles is also shown by the following XRD results.

5.2.3 XRD

To investigate the crystal structure of each particle, two methods of µ-XRD evaluation were used. For the average oxidation state over the entire particle, all patterns generated per 2D slice were added, averaged and evaluated. These are presented in figures 5.9 (BK-006, one slice), 5.10 (CP-003, two slices) and 5.11 (CP-004, two slices). The average oxidation states found in XANES were confirmed by the determined crystal structures. Additionally, individual µ-XRD pixel patterns were evaluated, which is described in figure 5.12, showing differences between near-surface areas and inner areas of the particle.

All reference patterns are from the COD and referenced in table 5.2.

Figure 5.9 shows the µ-XRD pattern averaged over the entire BK-006 particle compared to reference patterns of U_4O_9, UO_3 and U_3O_8. Peaks not indicated in the pattern belong to W resulting from the mounting needle. The sample pattern matches both oxidized patterns - UO_3 and U_3O_8 reasonably well, whilst clearly diverging from the U_4O_9 reference. Compared to the references, the intensity ratios diverge in the first three peaks, but match well for the following peaks after 15° 2θ. In the higher ° 2θ range, a slight shift towards lower values is observed, however the pattern and intensity ratios still match well. XANES indicated oxidation states closer to U(VI), supporting this result.
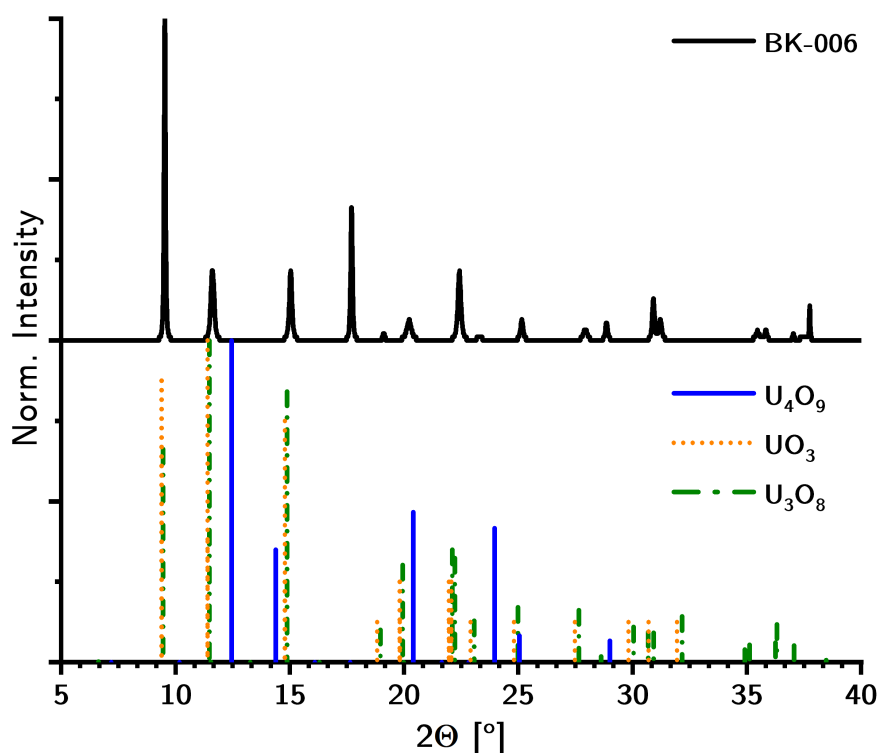
Fig. 5.9 XRD pattern for BK-006. Since the entire slice consists of hundreds of µ-XRD patterns, this is an average over the entire slice. The measured pattern clearly matches the more oxidized references UO_3 and U_3O_8 much better than the rather reduced reference U_4O_9.

Results for the particle CP-003 are clearly different from BK-006. Figure 5.10 shows the average patterns of two full slices through the pattern, matching the lower oxidized reference for U_4O_9 much better than UO_3. This is a strong contrast to BK-006 and also to CP-004, for which the results are shown in figure 5.11. Although the number of reflections in the reference pattern of U_4O_9 is limited, angles and intensity ratios match very well, suggesting that in CP-003, the average oxidation state of U is closer to U(IV) than to U(VI). The opposite is true for BK-006 and CP-004, for which XANES showed increased oxidation states close to U(VI).
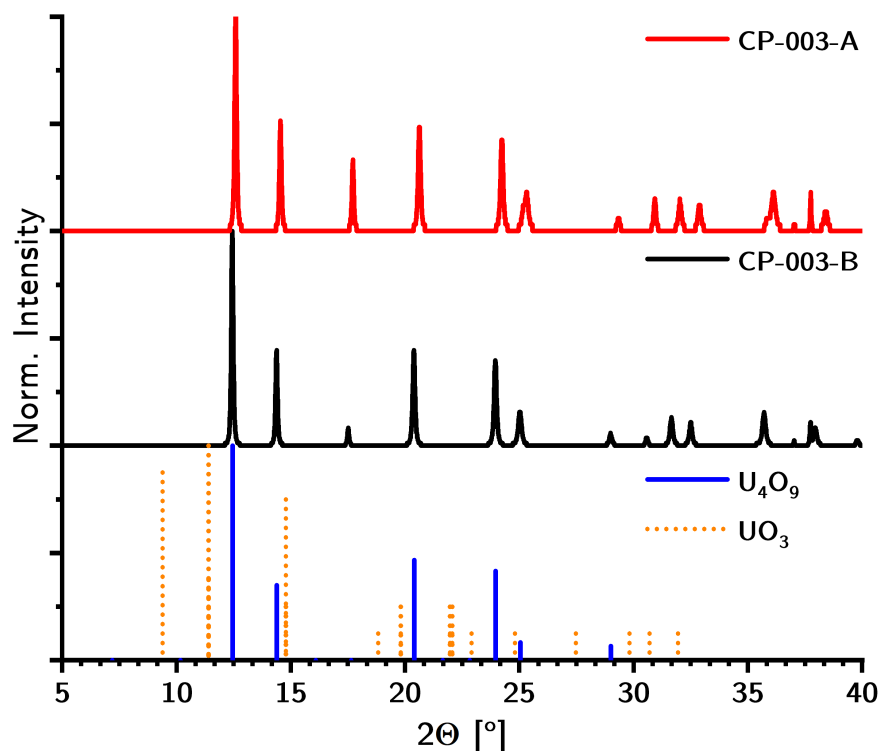
Fig. 5.10 Two average patterns for CP-003 over the full 2D slice. A difference to the BK-006 pattern can be seen, as both measured patterns match the more reduced reference U_4O_9 instead of UO_3.

It should be noted, that particle CP-003 had been heated to unknown temperatures in ultra high vacuum by illuminating it with an infrared laser previous to the beamline analysis. The influence of this procedure on the uranium speciation can not be defined without further investigation. This means that in contrast to BK-006 and CP-004, the oxidation states found in CP-003 might not correspond to the states before the laser heating procedure.

In summary, differences in oxidation state are measurable via beamline XRD in individual microcrystals, the findings are supported by XANES measurements and yield conclusive results.
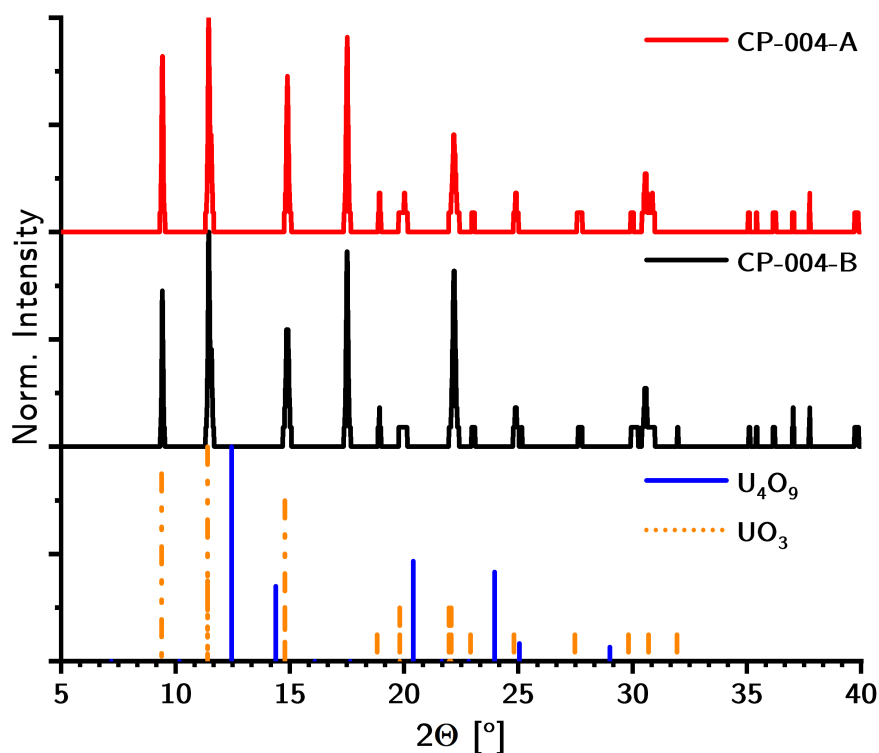
Fig. 5.11 Two average patterns for CP-004 over the full 2D slice. This one again is more similar to BK-006, matching the more oxidized UO_3 reference.

XRD Imaging

Figure 5.12 presents images resulting from the 2D µ-XRD scans. Each visible pixel corresponds to an individual XRD pattern, the ones marked in color were evaluated and compared to identify speciation changes between particle core and outer area. Based on these results, the indicated crystal structures need to be viewed with caution, as they can be only an approximation in these experiments. After comparing the individual patterns however, a trend of shifts towards higher oxidation states was observable in all three particles. This suggests a progressive oxidation on the surface due to exposure to air and humidity resulting in material weathering.

(a) CP-003.

(b) CP-004.
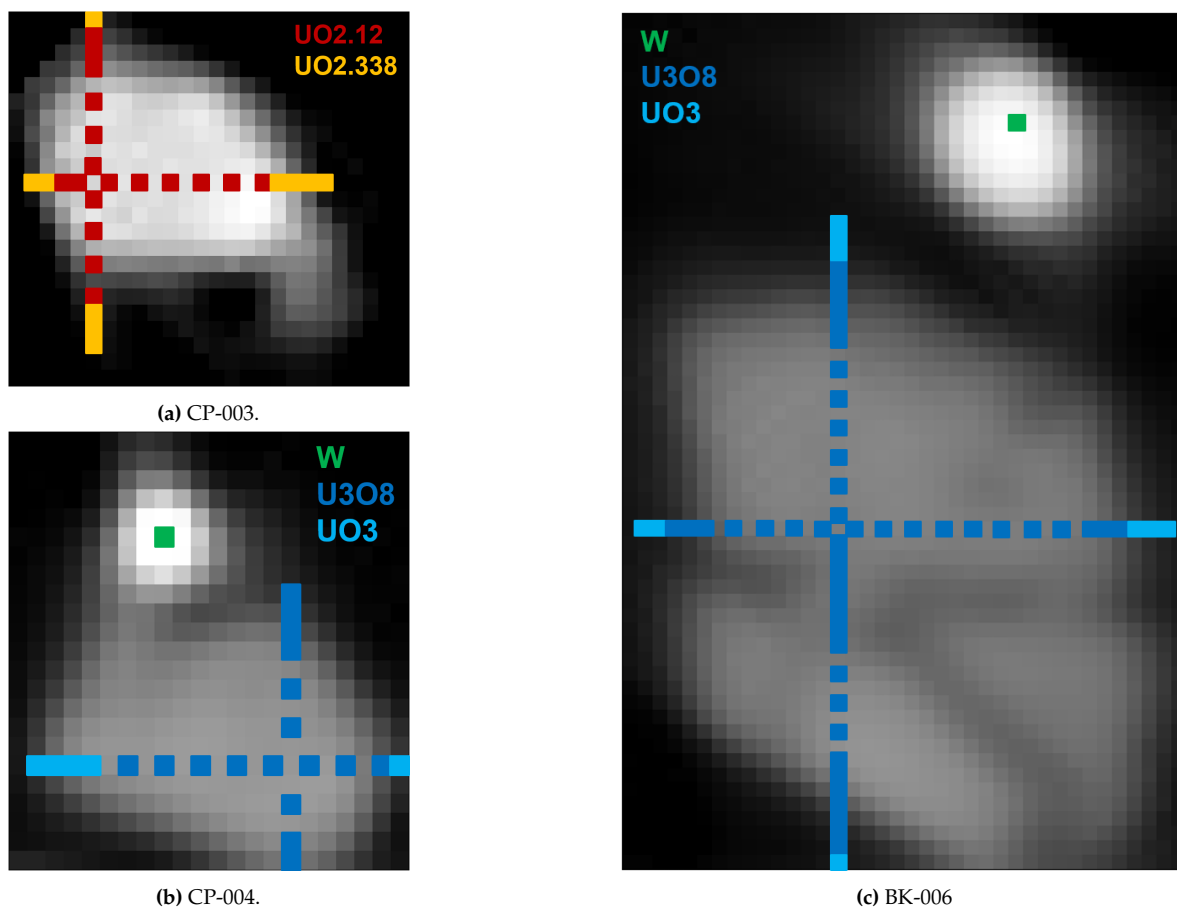
(c) BK-006

Fig. 5.12 XRD speciation results with 2D resolution:
(a) CP-003 shows a change in speciation between inner areas and the outer shell, with the latter yielding higher O/U ratio.
(b) With BK-006, the change to higher oxidation is less clear, but still observed in two positions.
(c) CP-004 shows the same trend, indicating higher oxidation towards the surface.

5.3 Beamline Results Discussion

Summary: All three particles were successfully scanned with μ-XRF, μ-XANES and μ-XRD. μ-XRF yielded 2D tomography maps, showing an even distribution of several relevant radionuclides throughout all particles, without revealing any hot spots. μ-XANES measurements successfully revealed uranium oxidation states in all particles within reasonable margins of error, however plutonium signal was not sufficient for evaluation. μ-XRD proved to be the most effective method in determining uranium speciation with spatial resolution. Since the particles base material is known to be uranium oxide, μ-XRD results could be compared to a number of reference patterns for uranium oxides with varying U oxidation states. Averaged patterns for each particle supported findings from XANES and showed CP-003 to be relatively reduced with an oxidation state between U(IV) and U(V), whilst CP-004 and BK-006 were more oxidized with an oxidation state between U(V) and U(VI). Evaluation of individual patterns per particle revealed further oxidation on the particle's surface.

Discussion: The presented experiments yielded an extensive set of data about the three investigated particles. Considering the time and cost efforts associated with beamline experiments however, analyzing an extended number of particles found during this work would be rather inefficient. To create a broad particle speciation database for comparisons between several sampling locations, extended measurement campaigns are necessary.
Based on the gathered amount of data per time, μ-XRD was the most efficient method applied here. Although the measurement time was longer compared to μ-XANES, each fully evaluated scan yielded several hundred XRD patterns with spacial resolution on the μm scale per particle instead of only one spot for XANES. Additionally, XANES quality seemed to suffer much more strongly from lower signal intensity compared to XRD. Information about oxidation states was extracted and matched from either method. In conclusion, future measurement campaigns could concentrate on μ-XRD experiments if time is a limiting factor. The value of additional XANES experiments depends on the existence of local uranium or plutonium concentrations, which could be investigated separately. Such hot spots would be detectable via μ-XRF mapping and if none are found, XANES experiments could be omitted in favor of analyzing more particles.

One point that could not be resolved in these experiments was the speciation analysis of plutonium within the particles. Generally such results are achievable, as has been demonstrated via XRF experiments before, however higher concentrations of plutonium might be necessary for lower self-absorption and interference by the uranium matrix.[Eriksson et al. 2005],[Law et al. 2019],[Lind et al. 2007] In a recent publication, COOK ET AL. showed even more detailed imaging and speciation data about particles from a nuclear test site in Australia.[Cook et al. 2021] In comparison, their particles

had much higher plutonium contents and were much larger than what was tested during this work. The application of High Resolution Scanning Electron Microscopy (HR-SEM) analysis in combination with Focused Ion Beam (FIB) cutting as demonstrated by COOK ET AL. should clearly be taken into consideration for future particle analysis. Additional promising techniques for uranium speciation are Electron BackScattering Detection (EBSD) and raman spectroscopy[Shiryaev et al. 2018]. A coupling of raman spectroscopy with SEM resolution would be especially useful for this case.[Pointurier et al. 2013] Both methods use much more common instruments and require much less effort in comparison to beamline-based techniques, however EBSD requires polished surfaces, as achievable for example via FIB cutting. Also, both only yield surface analysis and lack the tomographic information that μ-XAS is able to provide.

Including this last nondestructive method, a broad understanding of the particle's chemical composition was documented. To complete the data set, a switch to destructive methods was made by testing subsequent individual particle leaching and quantification of plutonium. A first approach is described in the following chapter, whilst further detailed experiments were part of a related masters thesis[Leifermann 2021]. Further discussion of the entire speciation results is part of the Summary and Discussion chapter.

6 Single Particle Leaching

So far in this work, uranium speciation was only achieved by beamline analysis, which is highly time-consuming, costly and to which access is very limited. Due to such restrictions, alternatives are highly desirable, for example a more direct approach to investigate particle solubility. As the particles are isolated and the tungsten needle is chemically very stable due to oxidative passivation, particle solubility can be tested directly on each sample by sequential particle leaching.

Chemical leaching experiments are commonly done with macroscopic particles and entire soil samples. Applying such a method to individual micron sized particles however required consideration of additional factors. The leaching setup used in this work is shown in figure 6.1. It consisted of standard laboratory clamping equipment, a variable height stage and a custom made Plexiglas tube to fix the needle.

6.1 Leaching Experimental Process

As a first test of feasibility, one inactive particle randomly chosen from a soil sample was glued to a W needle using the established process. SEM images were taken for later comparison before taking the particle out of the SEM. The needle was then clamped into a holder system and dipped into concentrated (w = 69 %) HNO_3 for about 20 h. Immediately after the first dip and again after the exposition time, an optical microscope was used to check whether the particle had been sheared off the needle. Inspection of the needle showed no changes except slight oxidation of the tungsten, indicated by the surface color changing to yellow. This effect only occurred when using HNO_3 in combination with a heat lamp. Even in these conditions, bonding between needle, glue and particle remained intact. Hence it was concluded, that this fixation method should be stable enough to implement it for single particle leaching without risk of losing the particle during individual steps.
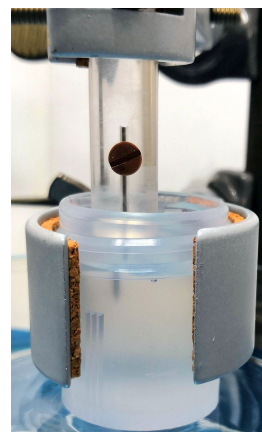
Fig. 6.1   The particle dissolution setup:
A Plexiglas tube, in which the needle was fixed by a screw, was mounted in standard laboratory clamping equipment. A variable height stage underneath allowed for careful dipping and withdrawing of the needle.

For the actual experiment, the particle KOP-011 was chosen. Data about KOP-011 measured in preceding analyses are summarized in table 6.1, whilst images were given previously in images 4.5 and 4.6d.

Tab. 6.1   Data about particle KOP-011 as known before leaching:

Designation	KOP-011
Origin	Kopachi
Size	30 μm × 32 μm
^{137}Cs activity	40.5 Bq
^{241}Am activity	2.3 Bq
relative ^{235}U quantitiy	0.975 %

All screw-cap containers and beakers used in the procedure were made of PerFluoroalkoxy Alkane (PFA) material and were cleaned with sub-boiled HNO_3 before use to avoid any cross contamination or loss of leached Pu to container walls. All used acids were of analytical grade purity. The procedure flow is listed below, with details for each step in the following:

1. HCl, $w = 37\,\%$ for 46.5 h as non-oxidative solvent

2. HNO_3, $c = 3\,mol/L$ for 71.4 h

3. HNO_3, $w = 69\,\%$ for 22.0 h as oxidative solvent

4. ^{242}Pu-tracer addition to all solutions and an additional blank acid

5. HF/HNO_3 digestion procedure for all solutions incl. the blank

6. Oxidation state adjustment and Pu-separation using TEVA-columns

7. γ-Spetrcometry for ^{137}Cs and ^{241}Am and ICP-MS measurements for ^{239}Pu, ^{240}Pu and ^{241}Pu

After each leaching step, the particle integrity was checked via optical microscopy and SEM imaging, to monitor changes in particle appearance and surface morphology.

6.1.1 HNO_3/HF Digestion Procedure

Each solution resulting from the leaching process was put through a standard digestion procedure involving HNO_3 and HF, to ensure complete dissolution of all residues in preparation for the following solid phase extraction to separate the Pu. This was especially important for the last dissolution experiment with conc. HNO_3. After this, it was not possible to determine whether the particle was dissolved completely. Some residues could have lost contact with the glue and fallen to the bottom of the beaker, where they could not be seen.

Before any chemical experiments were conducted with the sample solutions, a standard solution of ^{242}Pu was added to each as an internal recovery tracer. Additionally, a blank solution of diluted HNO_3 ($w = 2\%$) was created and also spiked with the tracer. This blank solution was treated in the same way as all sample solutions through the entire digestion and separation procedure. All necessary data about the used tracer are summarized in the following:

- **General data about the ^{242}Pu-standard:**
  Half-life time ^{242}Pu: 1.18×10^{13} s
  Specific activity ^{242}Pu: $145\,759\,000$ Bq/g
  Internal designation: xPu242-01.1

- **Data for reference-date:**
  Reference date: 01.06.2013
  Specific activity standard: 14.9 Bq/mL
  Mass fraction: 102 ppb (ng/g)

- **Data for measurement:**
  Date of measurement: 22.07.2019
  Specific activity standard: 14.9 Bq/mL
  Mass fraction: 102 ppb (ng/g)

About 50 mg of tracer solution was added to each sample solution. Then followed a standardized HNO_3/HF digestion procedure:

1. After the addition of the ^{242}Pu-tracer to each solution, all solutions were dried under a heatlamp

2. Uptake in conc. HNO_3 and heating under heatlamp until dry

3. Uptake in 1:1 conc. HNO_3/HF and heating until dry

4. Uptake in conc. HF and heating until dry

5. Again uptake in 1:1 conc. HNO_3/HF and heating until dry

6. Uptake in conc. HNO_3 and heating until dry

Finally, all samples were taken up in a solution of $Al(NO_3)_3$ ($c = 1\,mol/L$) and HNO_3 ($c = 3\,mol/L$) in preparation for the solid phase extraction.

6.1.2 Solid Phase Extraction of Pu

All four samples were processed in parallel in two subsequent steps.
First, the oxidation state of the plutonium in the samples had to be adjusted to Pu^{IV} as a requirement for the second step, the Pu separation by solid phase extraction:

Oxidation state adjustment

1. Addition of $2\,mL$ iron sulfamate

2. Waiting for $5\,min$ for plutonium reduction to Pu^{III}

3. Addition of $NaNO_2$, $c = 3.5\,mol/L$ for oxidation of Pu to Pu^{IV}

4. Heating to $90\,°C$

5. Filtration and rinsing with HNO_3 $c = 3\,mol/L$

After the oxidation state adjustment, the solutions were flushed through individual TEVA columns to separate plutonium from the other radionuclides that were leached from the particle. The central interest here was the separation of the ^{241}Pu and ^{241}Am isobars, to allow the quantification of ^{241}Pu by subsequent ICP-MS analysis. An additional benefit was the reduction of the U excess compared to Pu, which should reduce potential interference in the mass spectrum. A mass spectrometric quantification of ^{238}Pu was not expected to be possible, given the ^{238}U concentration before separation was expected to be about five orders of magnitude higher than the ^{238}Pu concentration. A difference this high could only be reduced sufficiently in several separation iterations, which again would also reduce the overall Pu concentration and was therefore omitted.

Solid Phase Extraction

1. Column conditioning with HNO_3, $c = 3\,mol/L$

2. Filling the column with sample solutions

3. Flushing with HNO_3, $c = 3\,mol/L$

4. Flushing with HCl, $c = 9\,mol/L$

5. Eluation of plutonium with hydroxylamine solution ($w = 0.1\,\%$)

6. Addition of HNO_3 until $w(HNO_3) = 2\,\%$

6.1.3 γ-Spectrometry

To investigate the leaching behavior of ^{137}Cs, ^{154}Eu and ^{241}Am, γ-spectrometry was performed on each of the three sample solutions resulting from the digestion reaction and before the Pu separation. To match the sample geometry for calibration, the same kind of PFA screw-cap container was used as for the sample solutions. A multi-nuclide calibration standard with the internal designation *xQCY-13* was diluted with HNO_3, $w_{HNO_3} = 2\,\%$ to match the sample matrix. For each sample a separate calibration was done, each time adjusting the standard solution volume to that of the sample, since they differed slightly at that point. All LODs resulting from those calibrations are depicted in table 6.2:

Tab. 6.2 LODs for the γ-spectrometry measurements of KOP-011:
Calibration measurements were based on a multi-nuclide standard with the internal designation *xQCY-13*, diluted in HNO_3, $w_{HNO_3} = 2\,\%$. The standard volume was matched to the samples for each measurement, simply by adding the HNO_3 between measurements. For optimal geometry matching, the same kind of container made from PFA was used for these calibrations.

	HCl conc.	HNO_3 dil.	HNO_3 conc.
^{137}Cs	0.096 Bq	0.113 Bq	0.042 Bq
^{154}Eu	0.063 Bq	0.022 Bq	0.013 Bq
^{241}Am	0.135 Bq	0.041 Bq	0.014 Bq

6.1.4 ICP-MS-Analysis

All four resulting solutions were analyzed by ICP-MS to quantify their Pu-content. Not all isotopes present in the sample could be measured this way: For ^{238}Pu, a high inferference from residual ^{238}U was to be expected because of the high excess of uranium in the original particle. A known standard of ^{242}Pu was added to all solutions before the HNO_3/HF digestion reaction as internal recovery tracer, hence the original ^{242}Pu-content could only be calculated based on the measurement of $^{239-241}$Pu.

To calibrate the ICP-MS measurement, the same ^{242}Pu standard solution was used in a seven-point calibration with steps at 0.5, 1, 10, 50, 100, 250 and 500 ppt ^{242}Pu. To compensate for fluctuation in the plasma flow, the resulting ^{242}Pu signal was divided by the simultaneously measured ^{129}Xe signal. ^{129}Xe is a trace component of the Ar gas used for the plasma and therefore its signal intensity is strictly dependent on the plasma flow. The result of the calibration measurement was the graph shown in figure 6.2 and the calibration equation **??**.

For the sample measurements, all sample solutions coming from the TEVA separation columns were collected in individual containers and adjusted to a volume of 10 to 11 mL with $w_{HNO_3} = 2\%$. 2 mL of each solution was used for the measurement, the rest was left for potential repetition of measurements or additional experiments.

All calibration and sample solutions were measured in a single experimental sequence in the following order:

1. All calibration solutions for up to 0.5 to 250 ppt
   with 2 runs of HNO_3 ($w_{HNO_3} = 2\%$) after each measurement

2. Sample solutions: Blank, conc. HCl, dil. HNO_3 and conc. HNO_3
   with 3 runs of HNO_3 $w_{HNO_3} = 2\%$ after each measurement

3. Calibration solution for 500 ppt
   with following runs of HNO_3 $w_{HNO_3} = 2\%$
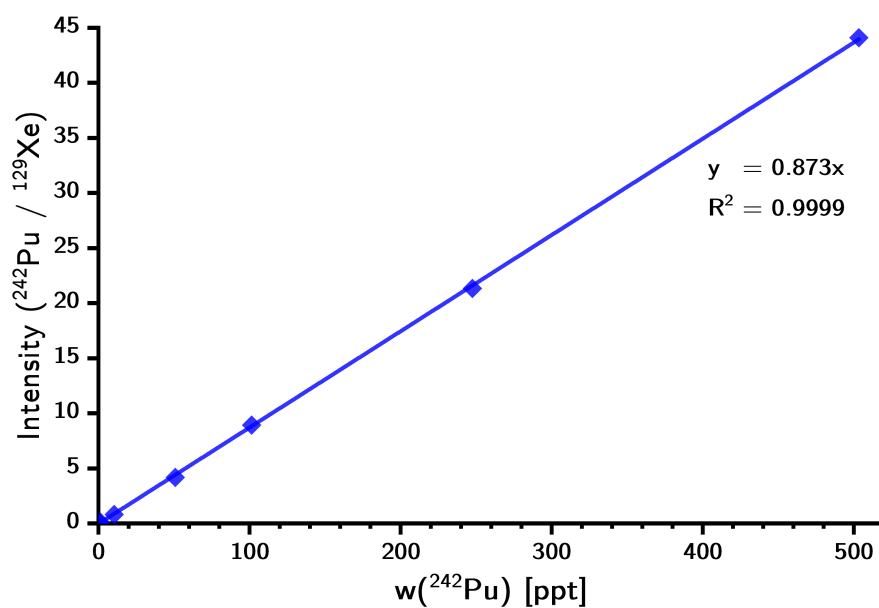
Fig. 6.2   Calibration chart for the ICP-MS-analysis after leaching:
The ICP-MS calibration was measured with reference solutions of ^{242}Pu in HNO$_3$, $w = 2\%$ over seven points at 0.5, 1, 10, 50, 100, 250 and 500 ppt. To compensate for plasma flow instabilities, instead of the ^{242}Pu-Signal, the ratio of $\frac{^{242}\text{Pu}}{^{129}\text{Xe}}$ was used for quantification.

The resulting calibration equation was $y = 0.0873x + n$, with $n = 0$ forced and a resulting $R^2 = 0.9999$.

6.2 Leaching Results

Before beginning the leaching process and after each individual step, the particle was investigated by SEM to observe any visible changes in the particle surface or overall morphology. This is of special interest because in combination with radionuclide analysis of the respective solutions, it could be deduced whether detected radionuclides resulted from more or less non-destructive leaching or from the particle being dissolved. The results are shown in figure 6.3:

When comparing figures 6.3a - the particle before leaching - and 6.3b - after HCl, there was no clearly visible difference after the first leaching step of 46.6 h in HCl. Hence, the HCl could only have had a very minor dissolution effect on the particles structure, for example on the topmost few nm or even no effect at all. A strong contrast in comparison is given by figure 6.3c, showing the particle after 71.4 h in diluted HNO_3. The surface is clearly disrupted and the particle has partially dissolved. To what extent it was dissolved could not be determined by this image alone, since the particle thickness was not known. A quantification of the process might be given by later ICP-MS analysis, when comparing the Pu content to that of the solution resulting from the last step, which is shown in figure 6.3d. Here, the particle is gone from the glue, only leaving a negative of its shape. Since at this point it was unclear whether the particle had been dissolved completely or simply lost contact with the glue, the resulting solution was divided into two equal parts and the measurable γ activity of the fractions compared. Both resulted in equal activity, indicating that the particle had actually been dissolved. For the subsequent process, both solutions were merged again.

(a) The initial particle before etching.

(b) Particle after 46.6 h in HCl, w = 37 %.

(c) Particle after 71.4 h in HNO$_3$, c = 3 mol/L.

(d) After 22.0 h in HNO$_3$, w = 69 %.
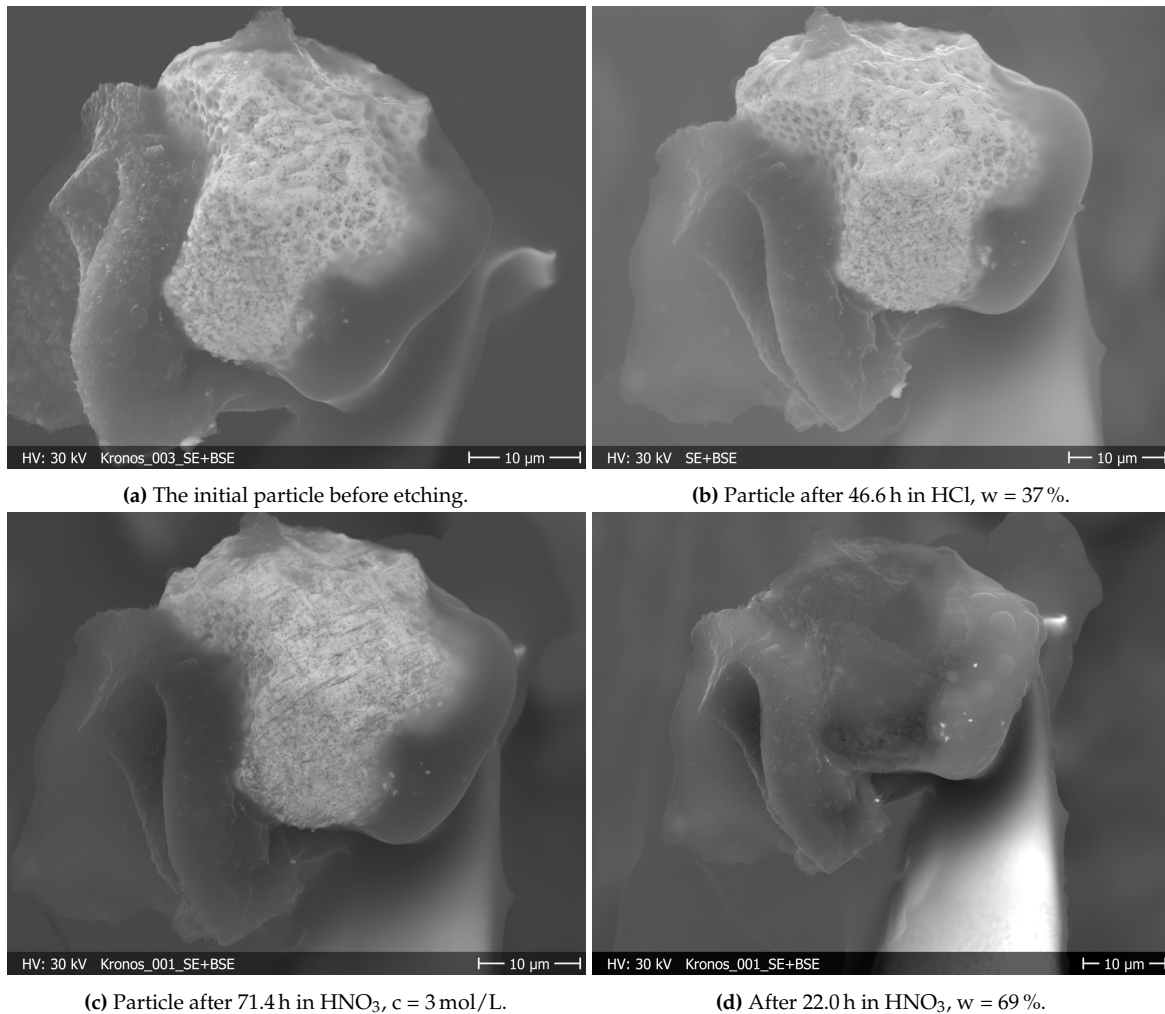
Fig. 6.3   SEM-Images during and after the single particle etching process:
(**6.3a**) Particle KOP-011 before etching. The finely structured surface was a good indicator for the progress of chemical dissolution
(**6.3b**) The same particle after 47 h in HCl ($w = 37$ %). The viewing angle was slightly turned due to remounting the needle to its original holder, but the surface structure was still visible. However, it did not seem to have changed in any way.
(**6.3c**) After 71 h in HNO$_3$ ($w = 3$ mol/L), the top layer of the surface seemed to have disintegrated, with structures looking like horizontal scratches appearing. The majority of the particle still remained intact however.
(**6.3d**) Finally, after 22 h in HNO$_3$ $w = 65$ %, the particle had disappeared completely, leaving behind only a negative in the SEMglue. Judging only from the images though, it could not clearly be concluded whether the particle was dissolved or simply had fallen off the glue.

6.2.1 ICP-MS Analysis for Pu

Based on the ^{242}Pu internal standard for the ICP-MS measurements, recovery rates for Pu were calculated. The results are displayed in table 6.3:

Tab. 6.3 Recovery rates for the ICP-MS measurement of KOP-011:
The recovery ratios for the first three solutions all were around 22 %, the last one about 10 % higher. The expected concentrations were calculated based on the initially added amount of ^{242}Pu in relation to the final weight of each solution after the entire process. The found values were based on each measurement, neglecting the ^{242}Pu-concentration originating from the particle (estimated from SNMS isotopic ratios, it should be well below 1 ppt).

Sample	expected	found	Recovery ratio
Blank	467.3 ppt	102.9 ppt	22.0 %
HCl $w = 37\,\%$	511.9 ppt	112.5 ppt	22.0 %
HNO$_3$ $c = 3\,$mol/L	477.5 ppt	106.7 ppt	22.3 %
HNO$_3$ $w = 65\,\%$	460.2 ppt	144.8 ppt	31.5 %

All recovery rates were below 32 %, which was unusual for the used digestion and separation process, where the recovery rates should have been well above 70 % to 80 %. However, after analyzing each solution coming from the column separation process via ICP-MS and not being able to detect residuals of Pu, the only conclusion could be that eluation of Pu with hydroxylamine solution had failed. Later attempts to re-eluate the column were unsuccessful, because the column became clogged, so this assumption could not be tested.

Nevertheless, despite low count rates, the detected concentrations of $^{239-241}$Pu were sufficient for quantification. This is mostly due to the fact that in ICP-MS the background counts in the mass range above uranium are almost zero. Results of the quantification are shown in table 6.4, where the values given as ppt are the measured ones. Values given in pg were corrected by the recovery ratio and the mass of the full sample to give an indication of the original plutonium content within the particle. The *Total* value displays the sum of all three acidic solution with the Blank subtracted from each. The blank also contained the ^{242}Pu-tracer, which is not 100 % isotope pure and hence contains traces of the other Pu isotopes.

Tab. 6.4   Results of the ICP-MS measurement of KOP-011:
The quantification of $^{239-241}$Pu was successful, only two values for ^{241}Pu were below the LOD. All LODs were calculated according to DIN 32645 based on 23 measurements of HNO$_3$, $w_{HNO_3} = 2\%$.
In ppt: The concentrations as calculated according to calibration.
In pg: The ppt values multiplied with the full sample mass and divided by the recovery rates. This way, they represent the amount of Pu in the original particle before dissolution.
Total (corrected): Sum of the results for each acid solution, each reduced by the Blank result, since this one was treated as background.

Nuclide	^{239}Pu			^{240}Pu			^{241}Pu		
	LOD $= 0.04$ ppt			LOD $= 0.05$ ppt			LOD $= 0.08$ ppt		
	ppt	pg	$\pm$	ppt	pg	$\pm$	ppt	pg	$\pm$
Blank	0.25	2.68	37.4 %	0.20	2.13	38.7 %	< LOD	0.66	91.8 %
HCl	0.80	8.27	27.1 %	0.47	4.86	28.0 %	< LOD	0.71	72.2 %
HNO$_3$ dil.	6.50	68.64	9.4 %	2.96	31.25	11.2 %	0.22	2.35	47.5 %
HNO$_3$ conc.	10.57	115.72	7.0 %	4.86	53.28	10.3 %	0.33	3.60	40.5 %
Total corr.	17.10	184.61	8.6 %	7.68	82.99	11.6 %	0.43	4.68	53.5 %

It became clear that the HCl leaching step was inefficient at dissolving Pu out of the particle, or even the uranium oxide matrix of the particle itself (see figure 6.3). The particle was however, clearly vulnerable to the HNO$_3$, even the diluted nitric acid dissolved parts of its surface. At that point, it remains unclear whether the same acid, if given more time than the applied 71 h, would have led to the same result as the concentrated HNO$_3$ in 22 h. Due to the low weight of the particle and general method restrictions, it was not possible to judge the rate of dissolution between the steps. Figure 6.3c clearly shows surface changes but does not allow quantification of the process. The ICP-MS results on the other hand show that already more than a third of the entire Pu inventory was in solution after the dil. HNO$_3$ step. A graphic representation of the Pu leaching effectiveness is shown in figure 6.4.
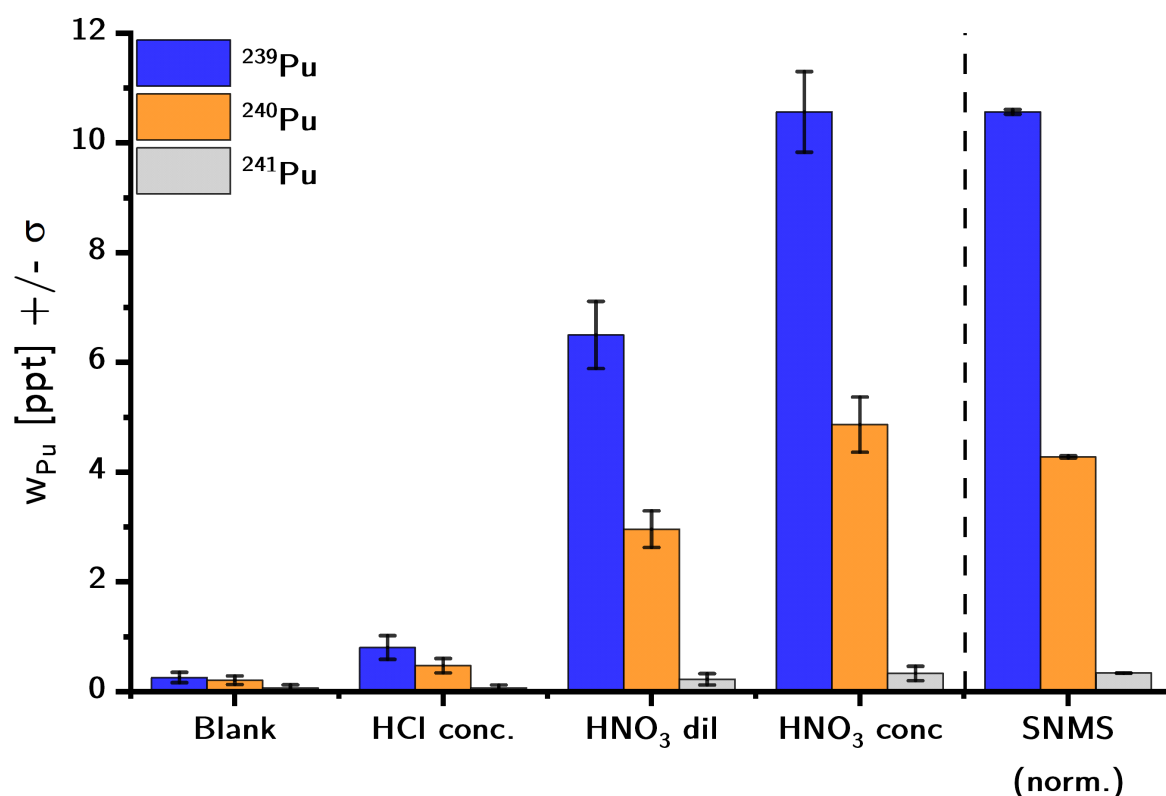
Fig. 6.4   Comparison of the ICP-MS results for Pu after the single particle leaching:
Compared to a ^{239}Pu-normalized SNMS isotope ratio, the measured results match well within the margin of error. The graph demonstrates, that the major fraction of Pu was leached by the HNO$_3$ solutions. A small Pu fraction however was clearly found in the HCl. The Pu measured in the blank can be attributed to the not perfectly monoisotopic tracer.

The most obvious result was that the major fraction of Pu had been leached by the HNO$_3$ solutions, with the conc. HNO$_3$ containing about 50 % more Pu than the diluted one. The relatively small difference between the two HNO$_3$ solutions indicated that much more than the topmost layer of the particle had been dissolved by the diluted HNO$_3$, which is a stark contrast to the initial interpretation of the SEM images. As the SEM images only show two dimensions and the particle's thickness can only be guessed, it is plausible that much more of it had been digested by the diluted HNO$_3$ than what was indicated by the images.
The measurable amount of Pu in the Blank solution was probably due to the ^{242}Pu-standard added to all four samples in equally high concentrations an can therefore be counted as the background signal.

Further interest lay in the calculation of isotopic ratios and their comparison to previously obtained results from SNMS analysis of the same particle. Figure 6.5 shows the percentages of total measured Pu for each nuclide separately for each leaching solution. Results from

both HNO_3 solutions matched well, and within the error margins, as did results from the HCl solutions and SNMS[Bosco et al. 2020].
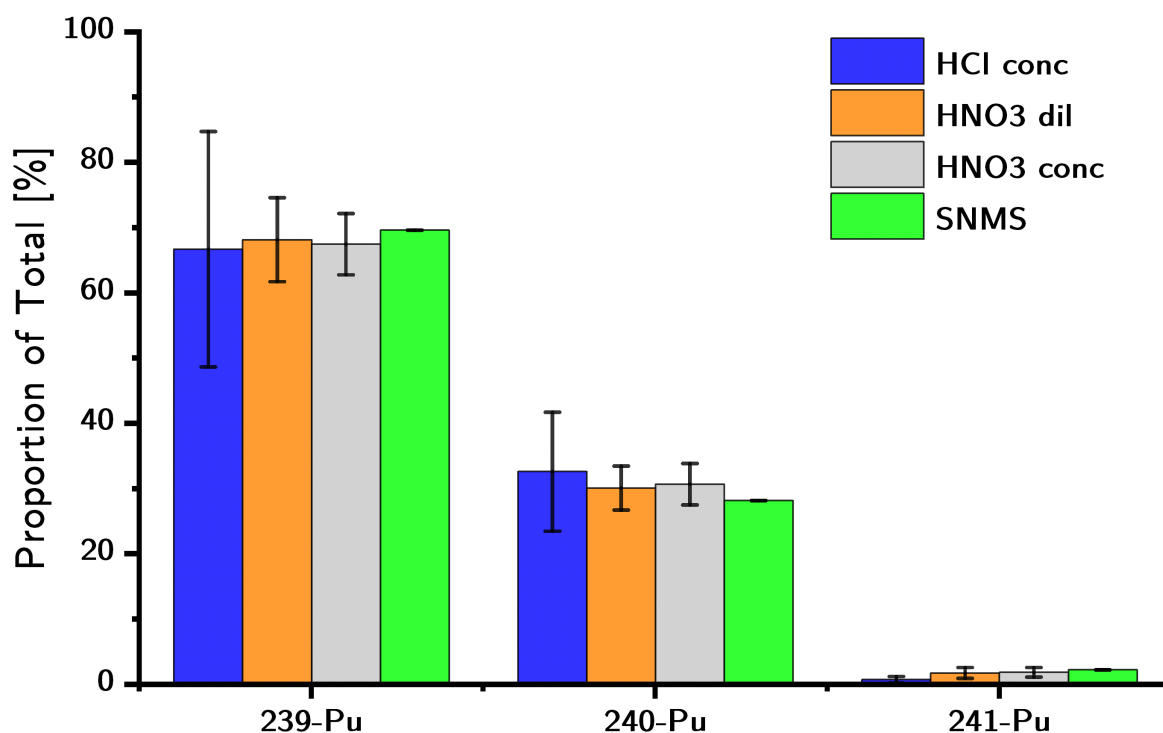
Fig. 6.5 Comparison of isotopic ratios obtained from ICP-MS and SNMS:
Based on outcomes of the $^{239-241}Pu$ quantification, proportions of the total Pu inventory measured for each isotope were calculated and drawn for comparison between the individual solutions and SNMS measurements for the same particle. All error bars are based on standard deviation from the measurements.

6.2.2 γ-Spectrometry for ^{137}Cs and ^{241}Am

All results of the γ-spectrometry are summarized in figure 6.6 and table 6.5. As in the original particle, three nuclides were identified and quantified: ^{137}Cs, ^{154}Eu and ^{241}Am. Detailed activity values for each step and comparative activities from the particle are listed in table 6.5. Figure 6.6 displays the relative recovery ratios of each dissolution step and a sum over all three steps.

HCl was an efficient extractant for ^{137}Cs, however it was less efficient for ^{241}Am. ^{154}Eu was slightly below the LOD for the HCl and the diluted HNO_3 solutions. Even in the concentrated HNO_3, the ^{154}Eu measurement resulted in an uncertainty of about 28 %. Whilst the total recovery rates for ^{137}Cs and ^{241}Am were well above 90 %, ^{154}Eu, which resulted solely from the concentrated HNO_3 solution, yielded only about 37 %. That value however is probably less accurate because of the concentrations being so close to the LOD and even the initial

concentration being very low at $0.19\,\mathrm{Bq} \pm 5.3\,\%$.
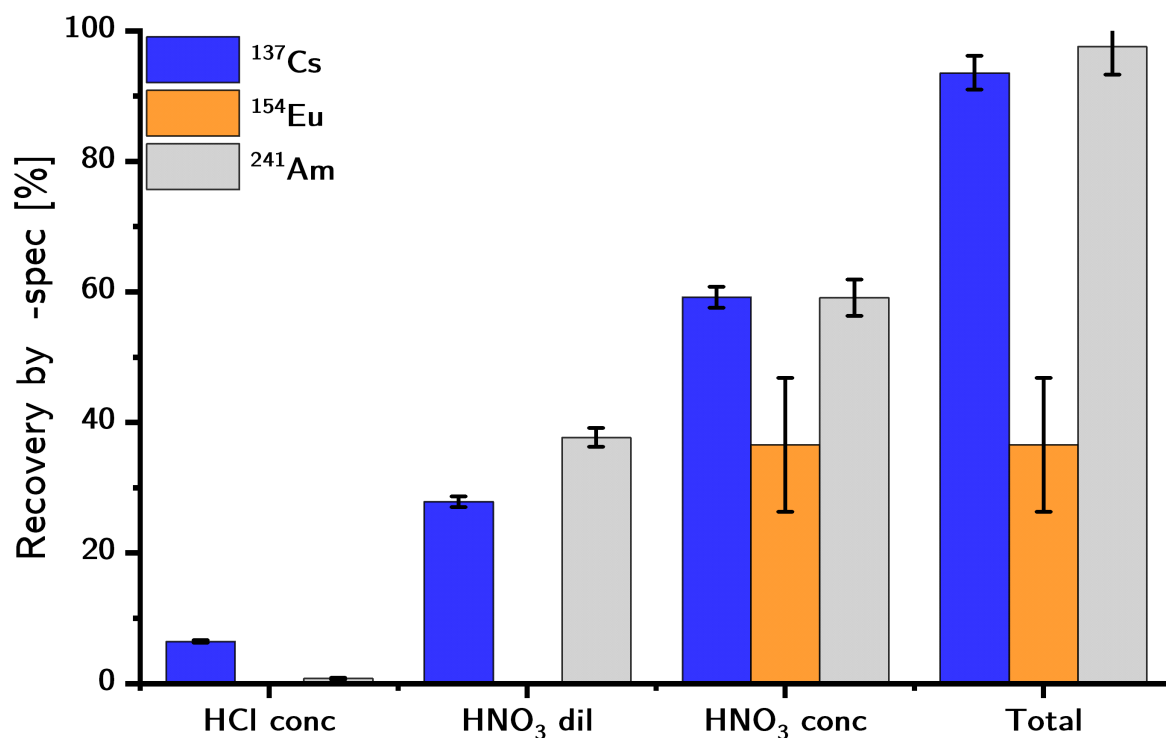
Fig. 6.6 **Results of γ spectrometry after single particle leaching:**
Displayed are the recovery rates in solution / partice for each solution after single particle leaching and the Pu separation process.
154Eu was below the LOD in HCl and diluted HNO_3, which is no surprise given its low activity in the original particle of $0.19\,\mathrm{Bq}$. Only $0.07\,\mathrm{Bq}$ or $36.6\,\%$ of that amount was retrieved in the final concentrated HNO_3 leaching.
241Am could be found in every solution, showing increasing activities up to a total recovery ratio of $97.6\,\%$, the total loss was well within the error margins for this nuclide.
137Cs was readily leached even by the HCl, where $6.5\,\%$ are not to be neglected, considering that the particle remained fully intact and had been leached by water for over 30 years. In total, $97.5\,\%$ of the original activity was recovered.
All recovery rates and relevant values are summarized in table 6.5.

Tab. 6.5   Results of the γ-spectrometry after single particle dissolution:
The activities of ^{137}Cs, ^{154}Eu and ^{241}Am were the only ones that could be quantified by γ spectrometry of the original particle. This table lists the activities of the mentioned nuclides as measured in each solution resulting from leaching, before measuring ICP-MS and the recovery rates as compared to the activities from the particle (also displayed in graph 6.6).

Nuclide	Activity	Uncertainty	Recovery from particle
HCl ($w = 37\,\%$)			
^{137}Cs	2.62 Bq	2.7 %	6.5 %
^{154}Eu	< 0.01 Bq	—	—
^{241}Am	0.02 Bq	15.2 %	0.8 %
HNO$_3$ ($c = 3\,$mol/L)			
^{137}Cs	11.30 Bq	2.9 %	27.9 %
^{154}Eu	< 0.02 Bq	—	—
^{241}Am	0.86 Bq	3.8 %	37.7 %
HNO$_3$ ($w = 65\,\%$)			
^{137}Cs	24.00 Bq	2.7 %	59.2 %
^{154}Eu	0.07 Bq	28.1 %	36.6 %
^{241}Am	1.35 Bq	4.7 %	59.1 %
Sum of all 3 solutions			
^{137}Cs	37.92 Bq	2.8 %	93.5 %
^{154}Eu	0.07 Bq	28.1 %	36.6 %
^{241}Am	2.23 Bq	4.4 %	97.6 %
Original Particle			
^{137}Cs	40.54 Bq	0.8 %	
^{154}Eu	0.19 Bq	5.3 %	
^{241}Am	2.28 Bq	0.8 %	

6.3 Leaching Discussion

In a first attempt at single particle leaching, a previously non-destructively but thoroughly analyzed particle has been dissolved over several subsequent steps. Numerous analytical results were obtained from each single step and interpreted.

The leaching step using concentrated HCl over 46.6 h did not yield any visible results, optical and SEM monitoring of the particle in question did not show any change in morphology or surface structure after the experiment. In ICP-MS concentrations of ^{154}Eu, ^{240}Pu and ^{241}Pu each were below their respective LODs. γ measurements however revealed clear ^{137}Cs leaching out of the particle's surface, yielding 6.5 % of its total inventory. With the particle's integrity unharmed, this amount certainly resulted from purely surface-near leaching and proves the high potential of ^{137}Cs mobility. In comparison, ^{241}Am only yielded 0.8 % of the entire inventory in this step. Its mobility therefore seems more dependent on the integrity of the particle's uranium oxide matrix.

In high contrast to the HCl, the HNO_3 solutions were quite capable of dissolving the particle. Whether the diluted HNO_3 would have been sufficient to dissolve it completely can only be assumed. Judging from the high recovery rates for ^{137}Cs and ^{241}Am (both above 25 %) and the measured Pu content of more than 50 % as compared to the concentrated HNO_3 and the visible dissolution effects on the particle, it probably would have been sufficient.

This experiment was meant to be a general proof of concept for subsequent single particle leaching and as such, it has clearly succeeded. The particle was dissolved in several steps whilst being monitored in between each single step. Visible changes could be documented and radionuclides were detected and quantified in each solution. However, since only a single particle was dissolved without any references, some of the results remain debatable. One of the most interesting questions for single particle leaching would be whether a significant difference between U^{IV} and U^{VI} could be concluded. In this work, the particle was not visibly attacked by a non-oxidant acid (HCl) in high concentration and the ICP-MS measurement yielded only very low concentrations of ^{239}Pu in the regarding solution. An oxidative acid like HNO_3 on the other hand dissolved the entire particle within a relatively short time. This can be seen as an indication that the particle mostly consisted of uranium in reduced oxidation state and the HCl only dissolved a thin, more oxidized surface.

Without more testing and some method validation this cannot be proven. It would therefore be highly interesting to use the same method for particles which have been analyzed by speciation methods like XRD or XANES beforehand to strengthen the base of this interpretation. This was part of an affiliated master thesis[Leifermann 2021], where - amongst others - BK-006, CP-004 and CP-003 were dissolved, with more detailed steps and more analysis. The process presented within this dissertation was mainly for method development and proof of principle,

where the limited availability of speciation-measured particles prohibited their dissolution. Another possibility would be using a more speciation sensitive set of solvents. With the particles being spent fuel material and therefore a wide mixture of elements and compounds, proven geochemical methods might still fail and certainly testing with references would be needed.

Even considering such shortcomings, the general method yielded a lot of analytical results and even more potential, and the experimental procedure worked out reasonably well. With some improvements already mentioned and summarized in the following, single particle leaching should be continued with more particles, after all non-destructive analysis has been finished. The technique remains as a versatile tool for future investigations and, if extended to a wide range of particles, could yield highly interesting results to feed into radionuclide mobility models.

- The Plexiglas needle holder and its screw should be substituted by some material more resistant to chemicals, especially against acidic fumes and organic solvents. The latter could be used to remove unwanted residuals of carbon tape on the particle.
- Used solvents, especially ones meant to be non-oxidizing should be degassed before the experiment to avoid oxidation by dissolved O_2
- A wider array of solvents could be used to further investigate this method's potential for speciation. There is potential in dissolution by slightly alkaline carbonate solutions.
- The plutonium separation procedure used in this experiment yielded low Pu recovery rates. This should be refined, as it could become an increasing problem with smaller particles when trying to detect Pu using ICP-MS. Therefore, a different Pu separation procedure should be chosen and / or, if available, a more sensitive detection method like ICP-MS with a sector field analyzer should be used.
- After some optimization - with special regard to speciation-specific solvents - this leaching method could be used on particles that were measured with XANES and XRD at a beamline or investigated with any other speciation technique to further prove its potential in that regard

7 Summary and Discussion

7.1 Summary

In the first steps of the project, a standardized routine for finding nuclear fuel particles of various sizes and activities within soil and sediment samples was successfully developed. The premise of avoiding any chemical treatment, to avoid changes in the particles speciation, was kept. The routine was revised and optimized to present a final process starting with the *sieving of samples* followed by *flotation* in a heavy liquid. Both steps primarily served to reduce sample size without losing particles of interest. Finding the actual hot particles was achieved by further sample preparation and SEM analysis in BSE mode. Finally, identified particles were extracted by the micromanipulator built into the SEM. The initially heavily utilized ATD was omitted in the final routine, but kept to potentially locate especially small particles in the sub-micron range.

An array of analytical methods was used on individual particles. SEM imaging and EDS measurements were repeated after extraction, since signal quality benefited greatly from the reduced background. In some cases, EDS mapping revealed inhomogeneous structures. Optical microscopy was attempted, but yielded no additional results and its imaging quality proved inferior compared to SEM. SIMS was shown for an unextracted Zr-containing particle and yielded isotopic information with spatial resolution. Examples were given from affiliated works, proving that SIMS also benefits greatly from particle extraction. Additionally, the possibilities of resonant laser-SNMS were presented based on works from an affiliated project measured on an extracted particle. This advanced technique allows determination of minor actinide isotopic ratios directly on the intact particle without previous chemical treatment.

To address speciation analysis, again in a non-destructive way, XAS experiments were conducted at the μ-XAS beamline, which is part of the SLS at the Paul Scherrer Institut. XRF, XANES and XRD measurements were conducted on two particles from the cooling pond and one from Prypjat, both located within the CEZ. Whilst XRF did not yield additional data, XANES could be used to identify the oxidation states of U in all three particles. The particle from Prypjat and one from the cooling pond were identified as being higher oxidized and the last one from the cooling pond rather reduced. Attempts to measure XANES for Pu

were unsuccessful, as signal quality was insufficient to identify oxidation states. XRD, in contrast, yielded well interpretable results in form of crystallographic data. Comparison of the measurement patterns to literature could not prove exact crystal structures per particle, but showed clear differences between reduced (U^{IV-V})and oxidized U^{V-VI} uranium oxide structures and supported the XANES results.

Although XAS measurements were a partial success, access to such techniques is limited and experiments as well as interpretation need high levels of experience. As an alternative for speciation sensitive analysis, the practicality of subsequent dissolution of individual particles was explored in the last chapter of this work. In a first experiment, one extracted particle was exposed to concentrated HCl, dil. HNO_3 (c = 1 mol/L), conc. HNO_3 and finally fully dissolved in a HF digestion process. SEM imaging after each step revealed the particles subsequent dissolution. ICP-MS and γ spectrometry measurements of each resulting solution allowed quantification of ^{239}Pu, ^{240}Pu, ^{241}Pu, ^{137}Cs and ^{241}Am. The results could be used to quantify the dissolution progress and also to determine the particles speciation when using more speciation sensitive solutions and well characterized reference particles or modeling data.

7.2 Discussion

The individual work packages of this project were already discussed in each regarding chapter. What is left, is an overall evaluation of the described single particle analysis process.

7.2.1 The Process

Despite being known for a relatively long time, particle separation and extraction is rarely used to analyze *individual* particles. Instead, often the bulk sample material is analyzed by γ spectrometry or dissolution and subsequent radioisotope isolation and α spectrometry or ICP-MS. Bulk analysis does have a major advantage over single particle investigation, which is higher activity by orders of magnitude. This results in much better time efficiency and throughput but ignores radionuclide speciation. The latter can be accounted for by using subsequent dissolution methods as described by V. KASHPAROV, SALBU, ET AL.[Kashparov et al. 2019], which can distinguish between particles and non-particular contamination. Such a procedure however still averages over all the particles contained in a sample, unless combined with single particle separation.

In contrast, separating, extracting and analyzing individual particles is the exact counterpart to an averaging bulk technique. It necessitates high amounts of manual labor and time to receive data for many particles. This can be mitigated to a degree by upscaling of preparative work, practice and experience. It also benefits greatly from automation, for example by automatic SEM scanning software. The methods advantage is, that it does not average but instead yield information about individual types of particles and ideally speciation and forensic data. If repeated for a sufficient number of particles, this procedure contributes to a detailed data model about the entire spectrum of particular contamination and allows more detailed predictions about the radioecological situation, radionuclide migration potential and particle dissolution behavior.

In conclusion, single particle extraction and analysis as presented in this work has outstanding potential for extensive analysis and wide sets of data, at the cost of manual labwork and time. As long as only non-destructive techniques are used, it further benefits from any available method that can be applied. For some of the methods presented, access is rare or expensive, especially resonant laser-SNMS and synchrotron-based analysis. However, even with only the more common methods like SEM/EDS, ICP-MS and γ spectrometry applied, the gained dataset becomes extensive and subsequent leaching still remains an option.

So, whether or not single particle analysis is worth the effort strongly depends on the kind of sample. In a case like Chernobyl, where many different types of particles are spread over diverse environments, original particle composition as well as weathering effects can

vary widely, so investigating and comparing individual particles yields a lot of additional information. In a potential case, where no such strong heterogeneity in particles is expected, extracting individual ones would probably not give much advantage over bulk analysis.

On the analytical side, most individual methods have already been discussed within the regarding chapters. The strongest impact on their implementation achieved during this work was the provision of individually mounted particles instead of the more often utilized complete dissolution of particles[Veliscek-Carolan 2016]. This greatly reduced the amount of manual work necessary for the application of SIMS/SNMS and allowed γ spectrometry in a reproducible geometry without interference from additional sample matrix. An alternative could be a mounting in resin, followed by polishing.[Pöml et al. 2017] This would further benefit the ease of handling as well as safety and reduce issues with sample geometry during SIMS measurements, which is optimized for flat, grounded samples instead of a "floating" particle. It however also would need further specialized tools and could interfere with the planned single particle dissolution experiments.

It would work with beamline experiments though, which based on the results presented here, yield exceptionally interesting data. The technique however is highly dependent on the utilized beamline setup. This means that although no Pu data could be measured during the presented line of experiments, this might be possible in a different specialized setup. Studies have shown, that generally, XAS analysis of the near field around U and Pu[Martin et al. 2003][Martin et al. 2007][Arab-Chapelet et al. 2016] in synthetic mixed oxides is possible and yields promising results. Spent fuel particles as analyzed during this project however are much smaller and have lower concentrations in Pu than the synthetic particles, so this might prove to be challenging.

7.2.2 The Results

Identified Particles: Finding hot particles in asphalt or Kopachi soil posed no major difficulties once the sequence was optimized. Fewer particles were identified in Red Forest samples during this work, which is most likely due to the fact that the samples were milled before analysis, so that individual particles were very small and hence harder to find based on SEM or activity. Particles were the easiest to find within the Cooling Pond sediment however. This is presumably due to the fact that the high pH and low O_2 environment preserves oxidation sensitive particles. Additionally, the sediment contained much less organic material than the Kopachi soil, which made a separation into a highly active small particle fraction and much less active bulk material simply by sieving possible.

The first result was the identification of individual particles by SEM and first elemental composition analysis by EDS. Expectations according to literature were to find three main types of particles:[Zhurba et al. 2009][Kashparov et al. 1996] Such mostly resembling the original nuclear fuel

structure consisting of UO_2, higher oxidized particles resulting from the ongoing reactor fire, and finally mixed oxide particles composed of $(U,Zr)O_x$. Most identified particles could be assigned to one of these categories, however any assignment to *reduced* or *oxidized* particles could only be made based on optical and morphological observations, whilst Zr-bearing particles were identified by EDS-measurements.

Although such particles were initially relatively stable in the Cooling Pond, in 2014 the pumping station supplying the Cooling Pond was shut off. Because of that, particle stability will potentially change rapidly in the near future, as the water level will start to sink and the previously stabilizing sediment conditions will change.[Bulgakov et al. 2009] Until 2017, the water level had lowered by 5 m, exposing sediment and the settled radionuclides and particles to the air.[Kanivets et al. 2020] This direct access to air and changing pH levels as well as microbial activity due to plant growth could lead to particles' oxidation and mobilization of radionuclides. This process should be closely monitored in the future to gain further insight into the weathering stability and behavior of such particles and to investigate further remediation potential.[IAEA 2019]

Speciation via beamline methods: Only three samples were analyzed by speciation-sensitive techniques, as described in the Beamline Analysis chapter. These three however revealed a relatively reduced particle from the Cooling Pond and also a relatively oxidized particle from Prypjat asphalt. Especially the latter strikes interest, as literature predicted a rather fast dissolution of such oxidized particles[Konoplev et al. 2000] outside of the Cooling Pond environment. Possible explanations for this are for once the unknown original size of the asphalt particle. It might have dissolved at the predicted rate and still be existent due to its large initial size. Another explanation is the environment, for example the microbiological activity within the asphalt surface should be entirely different from the one in Kopachi soil or Red Forest litter. As μ-XRD revealed a slightly higher oxidation state on each particles surface compared to the core, oxidation and weathering is still ongoing in both oxidized and reduced particles, even in the cooling pond environment. In addition, even CP-003 showing this oxidation gradient suggests that the vacuum heating was not responsible for its reduced state, unless the oxidation layer had reformed afterwards.

Expansion of such experiments to much more samples would yield better statistics to compare particles from different environmental matrices or for single particles with artificial weathering conditions applied in between measurements. Speciation measurements of additional radionuclides, especially plutonium would also greatly benefit such experiments, to investigate differences and similarities in mobilization between uranium and plutonium.[Buck et al. 2004] The general feasibility of such has been demonstrated before[Salbu et al. 2001][Martin et al. 2007] and hence should be considered for the particles presented here.

By combining XAS speciation with subsequent dissolution, potential correlations between ura-

nium oxidation state and leaching behavior of the many radionuclides within such particles could be investigated.

Speciation via sequential dissolution: The technique of sequentially dissolving individual particles as presented in this work opens several possibilities. As UO_2, in contrast to higher oxidized forms of uranium oxide, is relatively stable in non-oxidizing solvents like HCl[Oughton et al. 1993], sequential dissolution could be used to differentiate between reduced and oxidized uranium oxide particles.[Casas et al. 1998] In such way, such a routine is an alternative to beamline experiments, which require much more time, work and experience. In contrast to XRD or XANES however, this wold be a destructive approach and hence would leave only one attempt per particle. For validation purposes, it would be highly beneficial to sequentially dissolve particles after speciation measurements at a beamline to compare the findings and also to test such methods with artificial particles.

The second field opened by this technique is the separation and quantification of leached radionuclides after each solvent step. This was shown here by mass spectrometric quantification of several plutonium isotopes and gamma spectrometric quantification of ^{137}Cs, ^{241}Am and ^{154}Eu. Provided sufficiently low backgrounds on the respective masses, ideally by using subboiled quality solvents and / or a clean room, mass spectrometry could also quantify uranium isotopes. Further radionuclide separation might allow investigation of ^{90}Sr as another nuclide most relevant in radioecology.

7.2.3 Outlook

As this was a mostly method-focused work, the much wider application of developed and optimized methods should be approached in follow-up projects. Especially particle dissolution and beamline experiments were kept to very few samples here. The presented results would greatly benefit from statistically significant numbers of experiments and should be used to compare a large number of e. g. Cooling Pond particles.

The entire set of tools should also be expanded by testing alternative methods for example for uranium speciation, like Raman spectroscopy.[Shiryaev et al. 2018] Such methods could be much more accessible as compared to beamline techniques and at the same time keep the advantage of non-destructiveness.

Another factor not available for this work was a reference or benchmark for the applied techniques. The synthesis of model particles containing UO_2 as matrix with Pu, Zr and other elements[Arab-Chapelet et al. 2007] could provide such references for dissolution experiments.

Regarding other techniques presented here, TOF-SIMS and resonant laser-SNMS were only used in the beginning of this work and not even close to the limits of their potential applications. So far, only the surface of larger particles was analyzed. In future works with more particle samples being available and extracted, individual particles could be cut or polished either by a FIB or a SIMS ion source like the GCIB, Cs or O_2 ion gun. Either the spectrometry or the imaging modes of the TOF-SIMS could then be used to image element distribution, with SNMS potentially even for actinides like plutonium.

Lists

List of Instruments and Materials

Tab. 1   List of instruments and special materials used for this work.

Instrument	Manufacturer	Type
SEM	Philips	XL30 ESEM
EDS	remX	SDD-Detektor
SIMS	IonTOF	TOF.SIMS 5
Microscope	Nikon	Eclipse LV-DAF
γ-Spectrometer		HP-Ge
ICP-MS	Thermo-Fischer	IcapQ ASX520
MicroManipulator	Kleindiek	MM3A-EM
α-track detectors	Mi-Net	CR39-PADC
Sodium Polytungstate	TC-Tungsten Compounds GmbH	SPT-2 (solid)

List of Acronyms

SIMS	Secondary Ion Mass Spectrometry
SNMS	Secondary Neutral Mass Spectrometry
LMIG	Liquid Metal Ion Gun
PI	Primary Ion
SI	Secondary Ion
TOF	Time-Of-Flight
TOF-SIMS	Time Of Flight Secondary Ion Mass Spectrometry
EDS	Energy Dispersive X-ray Spectroscopy
SEM	Scanning Electron Microscopy
HR-SEM	High Resolution Scanning Electron Microscopy
ESEM	Environmental Scanning Electron Microscopy
FIB	Fast Ion Beam
EBSD	Electron BackScattering Detection
ATD	α Track Detection
XRD	X-ray Diffraction
µ-XRD	µ-focus X-ray Diffraction
XRF	X-ray Fluorescence
µ-XRF	µ-focus X-ray Fluorescence
XAS	X-ray Absorption Spectroscopy
µ-XAS	µ-focus X-ray Absorption Spectroscopy
SLS	Swiss Light Source
XANES	X-ray Absorption Near Edge Spectroscopy
µ-XANES	µ-focus X-ray Absorption Near Edge Spectroscopy
SE	Secondary Electron
GSE	Gaseous Secondary Electron
BSE	Backscattered Electron
ICP-MS	Inductively Coupled Plasma Mass Spectrometry
DI-water	Deionized Water
XAS	X-ray Absorption Spectroscopy
CEZ	Chernobyl Exclusion Zone
LV	Low Vacuum
HV	High Vacuum
UHV	Ultra High Vacuum
IR	InfraRed
cps	counts per second
GCIB	Gas Cluster Ion Beam

LOD	Limit Of Detection
PFA	PerFluoroalkoxy Alkane
HP	High Purity
RW	Red Forest
BK	Drillcore
KOP	Kopachi
HPGe	High Purity Germanium
RoI	Region of Interest
IRS	Institute of Radioecology and Radiation Protection
COD	Crystallography Open Database
PSI	Paul Scherrer Institut
LCF	Linear Combination Fitting
FIB	Focused Ion Beam

List of Figures

List of Tables

Bibliography

Adamov, E. O., Y. Cherkashov, and L. N. Podlazov (1996). *Chernobyl accident causes: Overview of studies over the decade*. IAEA–J4-TC972. International Atomic Energy Agency (IAEA). URL: http://inis.iaea.org/search/search.aspx?orig_q=RN:28053749.

Arab-Chapelet, B., S. Grandjean, et al. (2007). "Synthesis of new mixed actinides oxalates as precursors of actinides oxide solid solutions". In: *Journal of Alloys and Compounds* 444-445. PII: S0925838807000795, pp. 387–390. URL: http://www.sciencedirect.com/science/article/pii/S0925838807000795.

Arab-Chapelet, B., P. M. Martin, et al. (2016). "Multiscale structural characterizations of mixed U(iv)-An(iii) oxalates (An(iii) = Pu or Am) combining XAS and XRD measurements". eng. In: *Dalton transactions (Cambridge, England : 2003)* 45.16. Journal Article, pp. 6909–6919. eprint: 26979820.

Balonov, M. (2013). "The Chernobyl accident as a source of new radiological knowledge: implications for Fukushima rehabilitation and research programmes". eng. In: *Journal of radiological protection : official journal of the Society for Radiological Protection* 33.1. Journal Article, pp. 27–40. eprint: 23295495.

Batuk, O. N. et al. (2015). "Multiscale Speciation of U and Pu at Chernobyl, Hanford, Los Alamos, McGuire AFB, Mayak, and Rocky Flats". eng. In: *Environmental science & technology* 49.11. Journal Article Research Support, U.S. Gov't, Non-P.H.S., pp. 6474–6484. eprint: 25815708.

Belbeoch, B., J. C. Boivineau, and P. Perio (1967). "Changements de structure de l'oxyde U4O9". In: *Journal of Physics and Chemistry of Solids* 28.7. PII: 0022369767900704, pp. 1267–1275. URL: http://www.sciencedirect.com/science/article/pii/0022369767900704.

Bleuet, P. et al. (2008). "Probing the structure of heterogeneous diluted materials by diffraction tomography". eng. In: *Nature materials* 7.6. Journal Article, pp. 468–472. eprint: 18425135.

Bogatov, S. A. et al. (1990). "Form and parameters of the particles of the fuel ejection in the Chernobyl reactor accident". In: *Soviet Atomic Energy* 69.1. PII: BF02086947, pp. 595–601.

Bondarenko, O. A. et al. (1996). "Alpha-particle spectroscopy with TASTRAK (CR-39 type) plastic, and its application to the measurement of hot particles". In: *Nuclear Instruments and Methods in Physics Research Section A: Accelerators, Spectrometers, Detectors and Associated Equipment* 369.2-3. PII: S0168900296800568, pp. 582–587.

Bosco, H. (2020). "Ortsaufgelöste Analyse von Aktiniden mittels resonanter ToF-Laser-SNMS". Institut für Radioökologie und Strahlenschutz (IRS). Dissertation. Hannover: Leibniz Universität Hannover.

Bosco, H., L. Hamann, et al. (2021). "New horizons in microparticle forensics: Actinide imaging and detection of 238Pu and 242mAm in hot particles". eng. In: *Science advances* 7.44. Journal Article, eabj1175. eprint: 34714671.

Bosco, H., M. Weiss, et al. (2020). "Influence of the hyperfine structure on plutonium in resonant laser-SNMS". In: *Hyperfine Interactions* 241.1. PII: 1696, p. 27.

Boulyga, S. F., N. Erdmann, et al. (1997). "Determination of isotopic composition of plutonium in hot particles of the Chernobyl area". In: *Radiation Measurements* 28.1-6. PII: S135044879700098X, pp. 349–352. URL: http://www.sciencedirect.com/science/article/pii/S135044879700(

Boulyga, S. F. and T. Prohaska (2008). "Determining the isotopic compositions of uranium and fission products in radioactive environmental microsamples using laser ablation ICP-MS with multiple ion counters". eng. In: *Analytical and bioanalytical chemistry* 390.2. Journal Article, pp. 531–539. eprint: 17874079.

Bower, W. R. et al. (2019). "Metaschoepite Dissolution in Sediment Column Systems-Implications for Uranium Speciation and Transport". eng. In: *Environmental science & technology* 53.16. Journal Article, pp. 9915–9925. eprint: 31317743.

Buck, E. C., B. D. Hanson, and B. K. McNamara (2004). "The geochemical behaviour of Tc, Np and Pu in spent nuclear fuel in an oxidizing environment". In: *Geological Society, London, Special Publications* 236.1, pp. 65–88.

Bugai, D. A. et al. (2002). "Strontium-90 transport parameters from source term to aquifer in the Chernobyl Pilot Site". In: *Radioprotection* 37.C1. PII: rad20021pC1-11, pp. C1-11-C1–16. URL: https://www.researchgate.net/profile/dmitri-bugai/publication/239385278_strontium-90_transport_par

Bulgakov, A. et al. (2009). "Fuel particles in the Chernobyl cooling pond: current state and prediction for remediation options". eng. In: *Journal of environmental radioactivity* 100.4. Journal Article Research Support, Non-U.S. Gov't, pp. 329–332. eprint: 19185396.

Burakov, B. E., S. I. Shabalev, and E. B. Anderson (2003). *Principal Features of Chernobyl Hot Particles: Phase, Chemical and Radionuclide Compositions*.

Calvin, S. (2013). *XAFS for Everyone*. eng. Hoboken: CRC Press. 449 pp.

Casas, I. et al. (1998). "The role of pe, pH, and carbonate on the solubility of UO2 and uraninite under nominally reducing conditions". In: *Geochimica et Cosmochimica Acta* 62.13. PII: S0016703798001409, pp. 2223–2231. URL: http://www.sciencedirect.com/science/article/pii/S001670379800140

Conradson, S. D. et al. (2004). "Higher order speciation effects on plutonium L(3) X-ray absorption near edge spectra". eng. In: *Inorganic chemistry* 43.1. Journal Article, pp. 116–131. eprint: 14704059.

Cook, M. et al. (2021). "The nature of Pu-bearing particles from the Maralinga nuclear testing site, Australia". eng. In: *Scientific reports* 11.1. Journal Article, p. 10698. eprint: 34021195.

Cort, M. de (1998). *Atlas of caesium deposition on Europe after the Chernobyl accident*. CEC.

Danesi, P. et al. (2003). "Depleted uranium particles in selected Kosovo samples". In: *Journal of environmental radioactivity* 64.2-3. PII: S0265931X02000450, pp. 143–154.

Downs, R. T. and M. Hall-Wallace (2003). "The American Mineralogist crystal structure database". In: *American Mineralogist* 88.1, pp. 247–250.

Dubrovinsky, L. S. and S. K. Saxena (1997). "Thermal Expansion of Periclase (MgO) and Tungsten (W) to Melting Temperatures". In: *Physics and Chemistry of Minerals* 24.8. PII: 73TNK8R6DX1LH8CX, pp. 547–550.

Dyadkin, V. et al. (2016). "A new multipurpose diffractometer PILATUS@SNBL". eng. In: *Journal of synchrotron radiation* 23.Pt 3. Journal Article Research Support, Non-U.S. Gov't, pp. 825–829. eprint: 27140164. URL: https://soft.snbl.eu/bubble.html.

Eriksson, M. et al. (2005). "Source term identification of environmental radioactive Pu/U particles by their characterization with non-destructive spectrochemical analytical techniques". In: *Spectrochimica Acta Part B: Atomic Spectroscopy* 60.4. PII: S0584854705000248, pp. 455–469.

Esaka, F. et al. (2007). "Particle isolation for analysis of uranium minor isotopes in individual particles by secondary ion mass spectrometry". eng. In: *Talanta* 71.3. Journal Article, pp. 1011–1015. eprint: 19071406.

Fleischer, R. L., P. B. Price, and R. M. Walker (1980). *Nuclear tracks in solids. Principles and applications*. Berkeley and London: University of California Press. 605 pp.

Franzmann, M., H. Bosco, L. Hamann, et al. (2018). "Resonant laser-SNMS for spatially resolved and element selective ultra-trace analysis of radionuclides". eng. In: *Journal of Analytical Atomic Spectrometry* 33, pp. 730–737.

Franzmann, M., H. Bosco, C. Walther, et al. (2017). "A new resonant Laser-SNMS system for environmental ultra-trace analysis: Installation and optimization". In: *International Journal of Mass Spectrometry* 423. PII: S1387380617301574, pp. 27–32.

Golosio, B. et al. (2003). "Internal elemental microanalysis combining x-ray fluorescence, Compton and transmission tomography". In: *Journal of Applied Physics* 94.1, pp. 145–156.

Gražulis, S., D. Chateigner, et al. (2009). "Crystallography Open Database - an open-access collection of crystal structures". eng. In: *Journal of applied crystallography* 42.Pt 4. Journal Article, pp. 726–729. eprint: 22477773.

Gražulis, S., A. Daškevič, et al. (2012). "Crystallography Open Database (COD): an open-access collection of crystal structures and platform for world-wide collaboration". eng. In: *Nucleic acids research* 40.Database issue. Journal Article Research Support, Non-U.S. Gov't, pp. D420–7. eprint: 22070882.

Gražulis, S., A. Merkys, et al. (2015). "Computing stoichiometric molecular composition from crystal structures". eng. In: *Journal of applied crystallography* 48.Pt 1. Journal Article, pp. 85–91. eprint: 26089747.

Hamann, L. (2017). "Untersuchung radioaktiver Partikel mittels Sekundärionen-Flugzeit-Massenspektrometrie". Institut für Radioökologie und Strahlenschutz (IRS). ger. Hannover: Leibniz Universität Hannover. URL: 10.15488/8989.

Hanemann, P. (2019). "Extraktion und Analyse uranhaltiger Partikel aus Bodenproben". Institut für Radioökologie und Strahlenschutz. ger. B. Sc. thesis. Hannover: Leibniz Universität Hannover.

IAEA (2011). *Radioactive particles in the environment. Sources, particle characterization and analytical techniques*. IAEA-TECDOC-1663. 2011 update. Vienna: IAEA. 77 pp.

– (2019). *Environmental Impact Assessment of the Drawdown of the Chernobyl NPP Cooling Pond as a Basis for Its Decommissioning and Remediation*. IAEA-TECDOC-1886. Vienna: IAEA.

Jiménez-Ramos, M. C. et al. (2010). "(239)Pu, (240)Pu, and (241)Am determination in hot particles by low level gamma-spectrometry". eng. In: *Environmental science & technology* 44.11. Journal Article Research Support, Non-U.S. Gov't, pp. 4247–4252. eprint: 20441142.

Kanivets, V. et al. (2020). "Distribution and Dynamics of Radionuclides in the Chernobyl Cooling Pond". In: *Behavior of Radionuclides in the Environment II*. Ed. by A. Konoplev, K. Kato, and S. N. Kalmykov. Singapore: Springer Singapore, pp. 349–405.

Kashparov, V., V. Yoschenko, et al. (2012). "Radionuclide migration in the experimental polygon of the Red Forest waste site in the Chernobyl zone – Part 1: Characterization of the waste trench, fuel particle transformation processes in soils, biogenic fluxes and effects on biota". In: *Applied Geochemistry* 27.7. PII: S0883292711004495, pp. 1348–1358.

Kashparov, V. A. et al. (1996). "Formation of Hot Particles During the Chernobyl Nuclear Power Plant Accident". In: *Nuclear Technology* 114.2, pp. 246–253. URL: https://doi.org/10.13182/NT96-A35253.

Kashparov, V., S. Lundin, et al. (2003). "Territory contamination with the radionuclides representing the fuel component of Chernobyl fallout". In: *The Science of the total environment* 317.1-3. PII: S004896970300336X, pp. 105–119.

Kashparov, V., B. Salbu, et al. (2019). "Environmental behaviour of radioactive particles from chernobyl". eng. In: *Journal of environmental radioactivity* 208-209. Journal Article, p. 106025. eprint: 31419762.

Kelly, S. D., D. Hesterberg, and B. Ravel (2008). "Analysis of Soils and Minerals Using X-ray Absorption Spectroscopy". In: *Methods of Soil Analysis: Part 5-Mineralogical Methods*. Ed. by A. L. Ulery and R. Drees. SSSA Book Series. [Place of publication not identified]: SSSA, pp. 387–463.

Knoll, G. F. (2000). *Radiation detection and measurement*. eng. 3. ed. New York, NY: Wiley. 802 pp.

Konoplev, A. V. and A. A. Bulgakov (2000). "Transformation of 90 Sr and 137 Cs speciation in soils and bottom sediments". In: *Atomnaya Ehnergiya* 88.1, pp. 55–60.

Lauriat, J. P., G. Chevrier, and J. X. Boucherle (1989). "Space group of U4O9 in the beta phase". In: *Journal of Solid State Chemistry* 80.1. PII: 0022459689900340, pp. 80–93.

Law, K. A. et al. (2019). "Plutonium Migration during the Leaching of Cemented Radioactive Waste Sludges". In: *Geosciences* 9.1. PII: geosciences9010031, p. 31.

Leifermann, L. (2018). "Lokalisierung und Vergleich uranhaltiger Partikel in Bodenproben". Institut für Radioökologie und Strahlenschutz. ger. B. Sc. thesis. Hannover: Leibniz Universität Hannover.

– (2021). "Extraktion und Speziationsanalytik von Brennstoffpartikeln aus der Chernobyl Exclusion Zone". Institut für Radioökologie und Strahlenschutz. ger. M. Sc. thesis. Hannover: Leibniz Universität Hannover.

Lind, O. C., B. Salbu, K. Janssens, K. Proost, and H. Dahlgaard (2005). "Characterization of uranium and plutonium containing particles originating from the nuclear weapons accident in Thule, Greenland, 1968". eng. In: *Journal of environmental radioactivity* 81.1. Journal Article Research Support, Non-U.S. Gov't, pp. 21–32. eprint: 15748658.

Lind, O. C., B. Salbu, K. Janssens, K. Proost, M. García-León, et al. (2007). "Characterization of U/Pu particles originating from the nuclear weapon accidents at Palomares, Spain, 1966 and Thule, Greenland, 1968". eng. In: *The Science of the total environment* 376.1-3. Journal Article Research Support, Non-U.S. Gov't, pp. 294–305. eprint: 17336369.

Loopstra, B. O., J. C. Taylor, and A. B. Waugh (1977). "Neutron powder profile studies of the gamma uranium trioxide phases". In: *Journal of Solid State Chemistry* 20.1. PII: 0022459677900469, pp. 9–19.

Makarova, T. P., B. A. Bibichev, and V. D. Domkin (2008). "Destructive analysis of the nuclide composition of spent fuel of WWER-440, WWER-1000, and RBMK-1000 reactors". In: *Radiochemistry* 50.4. PII: 4015, pp. 414–426.

Martin, P., S. Grandjean, et al. (2007). "XAS study of (U1-yPuy)O2 solid solutions". In: *Journal of Alloys and Compounds* 444-445. PII: S0925838807000783, pp. 410–414.

Martin, P., M. Ripert, et al. (2003). "A XAS study of the local environments of cations in (U, Ce)O2". In: *Journal of Nuclear Materials* 312.1. PII: S0022311502015908, pp. 103–110.

Merkys, A. et al. (2016). "COD::CIF::Parser: an error-correcting CIF parser for the Perl language". eng. In: *Journal of applied crystallography* 49.Pt 1. Journal Article, pp. 292–301. eprint: 26937241.

Mihály Pósfai et al. (1998). "Iron sulfides from magnetotactic bacteria: Structure, composition, and phase transitions". en. In: *American Mineralogist* 83.11, pp. 1469–1481. URL: https://www.degruyter.com/document/doi/10.2138/am-1998-1108/html.

Mi-Net Technology Ltd (2020). *Dosimeter Detector Plastic Cr39 PADC*. URL: http://www.mi-net.co.uk/dosimeter-detector-plastic-cr39.php (visited on 03/09/2020).

Newville, M. (2013). "Larch: An Analysis Package for XAFS and Related Spectroscopies". In: *Journal of Physics: Conference Series* 430. URL: https://xraypy.github.io/xraylarch/.

Nolf, W. de and K. Janssens (2010). "Micro X-ray diffraction and fluorescence tomography for the study of multilayered automotive paints". In: *Surface and Interface Analysis* 42.5, pp. 411–418.

Nucleonica GmbH (2017). *Nucleonica Nuclear Science Portal: Nuclide Datasheets*. Version Version 3.0.187.0001. URL: www.nucleonica.com (visited on 03/24/2020).

Oughton, D. H. et al. (1993). "Under-determination of strontium-90 in soils containing particles of irradiated uranium oxide fuel". In: *The Analyst* 118.9, p. 1101.

Pointurier, F. and O. Marie (2013). "Use of micro-Raman spectrometry coupled with scanning electron microscopy to determine the chemical form of uranium compounds in micrometer-size particles". In: *Journal of Raman Spectroscopy* 44.12, pp. 1753–1759.

Pöml, P. and B. Burakov (2017). "Study of a "hot" particle with a matrix of U-bearing metallic Zr: Clue to supercriticality during the Chernobyl nuclear accident". In: *Journal of Nuclear Materials* 488. PII: S0022311517301320, pp. 314–318.

PSI (2009). *microXAS - X05LA: Environmental & Materials Sciences*. Paul Scherrer Institut. URL: https://www.psi.ch/en/sls/microxas (visited on 03/17/2020).

Quirós, M. et al. (2018). "Using SMILES strings for the description of chemical connectivity in the Crystallography Open Database". eng. In: *Journal of cheminformatics* 10.1. Journal Article, p. 23. eprint: 29777317.

Raiwa, M. (2021). "Ortsaufgelöste Untersuchung und Speziation anthropogener Radionuklide in der Umwelt mittels Massenspektrometrie". Institute of Radioecology and Radiation Protection. Dissertation. Hannover: Leibniz Universität Hannover.

Ravel, B. and M. Newville (2005). "ATHENA, ARTEMIS, HEPHAESTUS: data analysis for X-ray absorption spectroscopy using IFEFFIT". eng. In: *Journal of synchrotron radiation* 12.Pt 4. Journal Article Research Support, Non-U.S. Gov't, pp. 537–541. eprint: 15968136. URL: https://bruceravel.github.io/demeter/.

Rest, J. et al. (2019). "Fission gas release from UO2 nuclear fuel: A review". In: *Journal of Nuclear Materials* 513. PII: S0022311518309449, pp. 310–345.

Salbu, B., T. Krekling, et al. (2001). "High energy X-ray microscopy for characterisation of fuel particles". In: *Nuclear Instruments and Methods in Physics Research Section A: Accelerators, Spectrometers, Detectors and Associated Equipment* 467-468. PII: S0168900201006416, pp. 1249–1252. URL: http://www.sciencedirect.com/science/article/pii/S0168900201006416.

Salbu, B., O. C. Lind, and L. Skipperud (2004). "Radionuclide speciation and its relevance in environmental impact assessments". eng. In: *Journal of environmental radioactivity* 74.1-3. Journal Article Research Support, Non-U.S. Gov't, pp. 233–242. eprint: 15063551. URL: https://www.sciencedirect.com/science/article/pii/S0265931X0400013X.

Salbu, B. (2009). "Radioactive Particles Released from Different Nuclear Sources". In: *Radioactive Particles in the Environment*. Ed. by D. H. Oughton and V. Kashparov. NATO Science for Peace and Security Series C: Environmental Security. Dordrecht: Springer Netherlands, pp. 3–13.

Sanchez, D. F., D. Grolimund, et al. (2017). "A 2D and 3D X-ray μ-diffraction and μ-fluorescence study of a mixed ionic electronic conductor". In: *International Journal of Hydrogen Energy* 42.2. PII: S0360319916333833, pp. 1203–1211.

Sanchez, D. F., A. S. Simionovici, et al. (2017). "2D/3D Microanalysis by Energy Dispersive X-ray Absorption Spectroscopy Tomography". eng. In: *Scientific reports* 7.1. Journal Article, p. 16453. eprint: 29184091.

Schieber, J. (2010). "Iron Sulfide Formation". In: *Encyclopedia of Geobiology*. Ed. by J. Reitner and V. Thiel. 1. Ed. Encyclopedia of Earth Sciences Series. Berlin: Springer Netherland, pp. 486–502.

Schneider, C. A., W. S. Rasband, and K. W. Eliceiri (2012). "NIH Image to ImageJ: 25 years of image analysis". eng. In: *Nature methods* 9.7. Historical Article Journal Article Research Support, N.I.H., Extramural, pp. 671–675. eprint: 22930834. URL: https://imagej.nih.gov/ij/.

Schroer, C. G. (2001). "Reconstructing x-ray fluorescence microtomograms". In: *Applied Physics Letters* 79.12, pp. 1912–1914.

Schulz, W. (2020). "Untersuchung des Migrationsverhaltens von Radionukliden in Umweltkompartimenten mit spektroskopischen und massenspektrometrischen Methoden". Institute of Radioecology and Radiation Protection. Dissertation. Hannover: Leibniz Universität Hannover. URL: https://www.repo.uni-hannover.de/handle/123456789/10383.

Schulz, W. et al. (2019). "Sorption of radiostrontium on various soils". In: *Applied Geochemistry* 101. PII: S0883292719300010, pp. 103–108.

Shiryaev, A. A. et al. (2018). "Forensic study of early stages of the Chernobyl accident: Story of three hot particles". In: *Journal of Nuclear Materials* 511. PII: S0022311518308596, pp. 83–90.

Siegel, S. (1955). "The crystal structure of trigonal U3O8". In: *Acta Crystallographica* 8.10. PII: S0365110X55001953, pp. 617–619.

Smith, J. T. and N. A. Beresford, eds. (2005). *Chernobyl - catastrophe and consequences*. eng. Springer-Praxis books in environmental sciences. Berlin: Springer. 310 pp. URL: http://www.loc.gov/catdir d.html.

Solé, V. A. et al. (2007). "A multiplatform code for the analysis of energy-dispersive X-ray fluorescence spectra". In: *Spectrochimica Acta Part B: Atomic Spectroscopy* 62.1. PII: S0584854706003764, pp. 63–68. URL: http://pymca.sourceforge.net/.

Steinhauser, G., A. Brandl, and T. E. Johnson (2014). "Comparison of the Chernobyl and Fukushima nuclear accidents: a review of the environmental impacts". eng. In: *The Science of the total environment* 470-471. Comparative Study Journal Article Research Support, U.S. Gov't, P.H.S. Review, pp. 800–817. eprint: 24189103.

The Chernobyl accident (1992). *A report by the International Nuclear Safety Advisory Group*. Updating. Vol. 75,7. Safety series Safety reports. Vienna. 134 pp.

UNSCEAR (2000). *Sources and effects of ionizing radiation*. eng. New York: United Nations. 654 pp.

Veliscek-Carolan, J. (2016). "Separation of actinides from spent nuclear fuel: A review". eng. In: *Journal of hazardous materials* 318. Journal Article Review Journal Article Review, pp. 266–281. eprint: 27427893.

Willis, B. T. M. (1978). "The defect structure of hyper-stoichiometric uranium dioxide". In: *Acta Crystallographica Section A* 34.1. PII: S0567739478000157, pp. 88–90.

Yano, J. and V. K. Yachandra (2009). "X-ray absorption spectroscopy". eng. In: *Photosynthesis research* 102.2-3. Journal Article Research Support, N.I.H., Extramural Research Support, U.S. Gov't, Non-P.H.S. Review Journal Article Research Support, N.I.H., Extramural Research Support, U.S. Gov't, Non-P.H.S. Review, pp. 241–254. eprint: 19653117.

Zhurba, M. et al. (2009). "The "Hot Particles" Data Base". In: *Radioactive Particles in the Environment*. Ed. by D. H. Oughton and V. Kashparov. NATO Science for Peace and Security Series C: Environmental Security. Dordrecht: Springer Netherlands, pp. 187–195.

A Acknowledgments / Danksagung

B Appendix

This chapter contains further SEM images and EDS spectra of particles. More can be found in affiliated B.Sc. and M.Sc. theses[Hanemann 2019],[Leifermann 2018],[Leifermann 2021] and also in cooperating dissertations[Bosco 2020],[Hamann 2017],[Schulz 2020].

B.1 Drillcore (BK) Particles
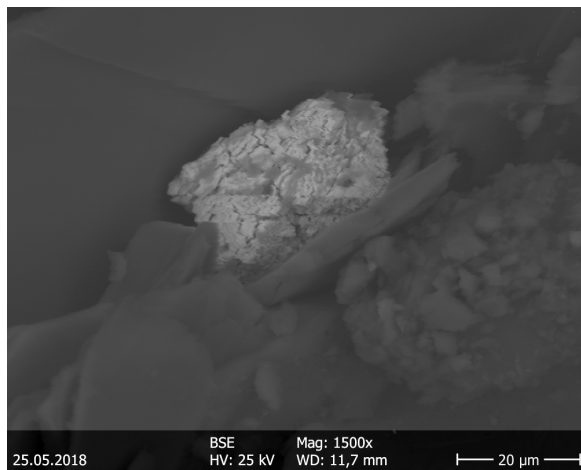
(a) SEM Image of BK-001(BSE)
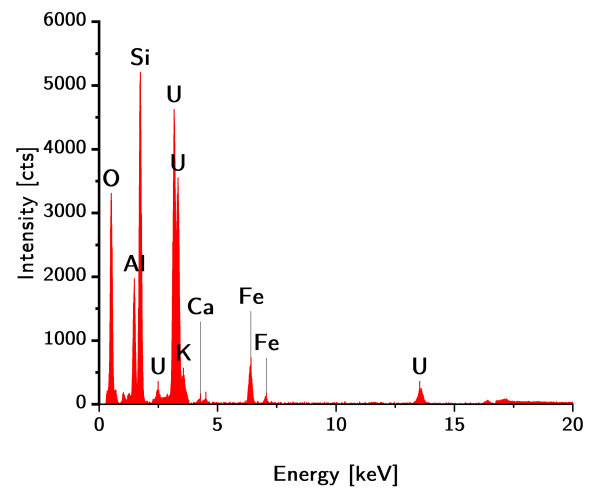
(b) EDS spectrum for BK-001

Fig. B.1   BK-001 (Uwe) imaging and EDS analysis. The particle was found as part of an affiliated thesis[Hanemann 2019]
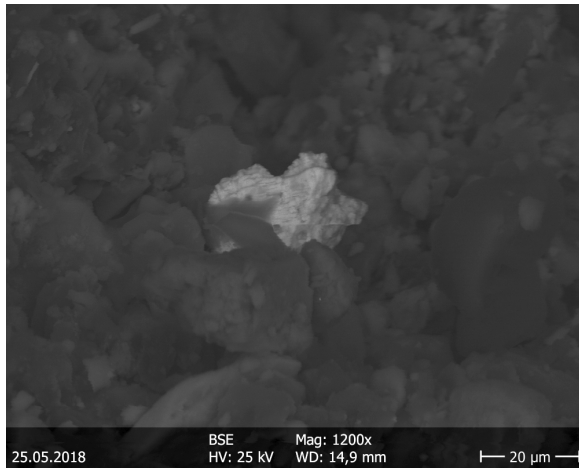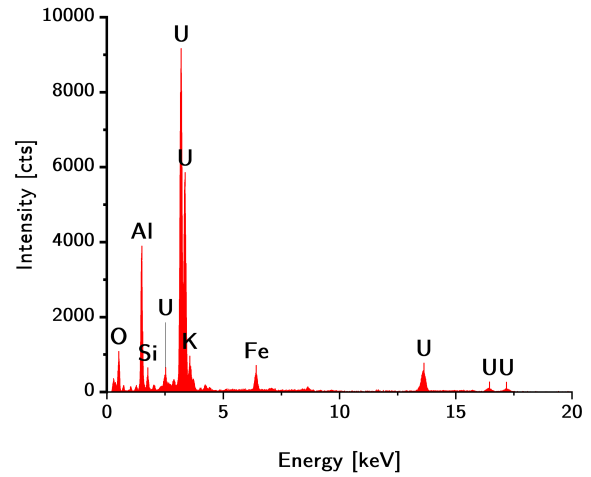
(a) SEM Image of BK-002 (BSE)
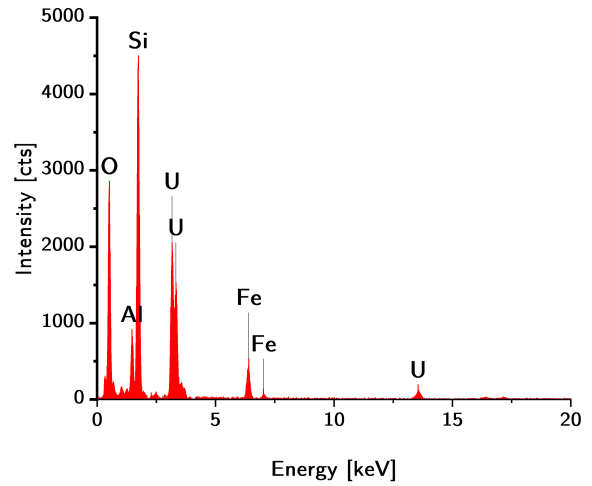
(b) EDS spectrum for BK-002

Fig. B.2 BK-002 (Viktoria) imaging and EDS analysis. The particle was found as part of an affiliated thesis[Hanemann 2019]
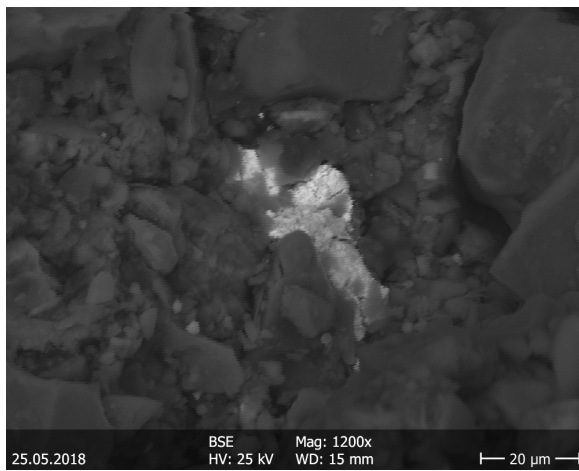
(a) SEM Image of BK-003 (BSE)
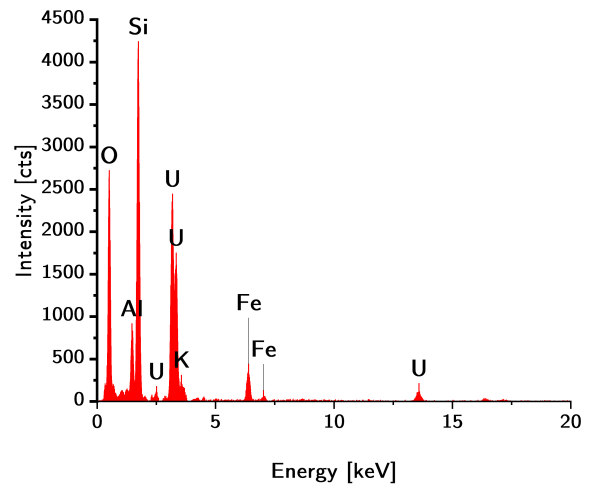
(b) EDS spectrum for BK-003

Fig. B.3 BK-003 (Wolfgang) imaging and EDS analysis

(a) SEM Image of BK-004 (BSE)

(b) EDS spectrum for BK-004
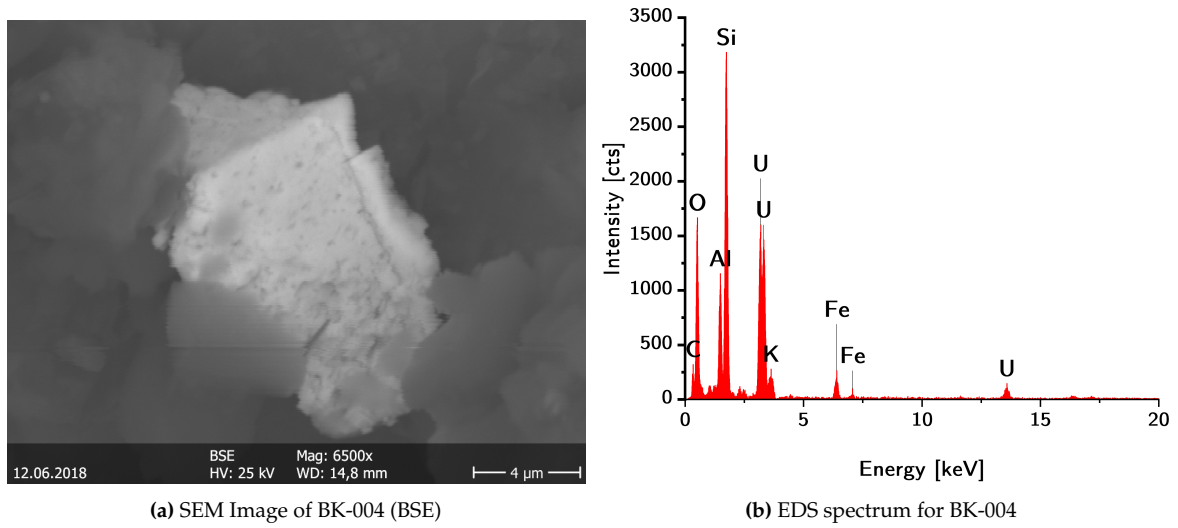
Fig. B.4 **BK-004 (Xenu) imaging and EDS analysis**

(a) SEM Image of BK-005 (BSE)

(b) EDS spectrum for BK-005
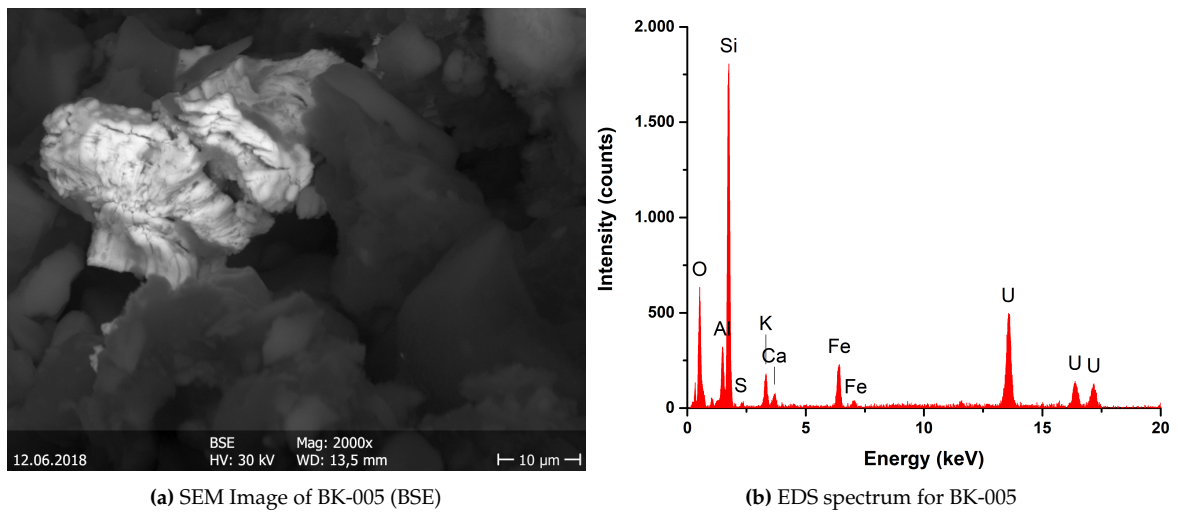
Fig. B.5 **BK-005 (Yuna) imaging and EDS analysis.**
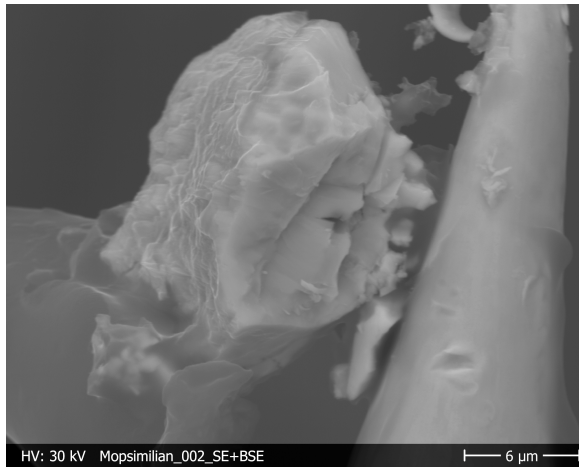
(a) SEM Image of BK-006 (SE+BSE overlay)
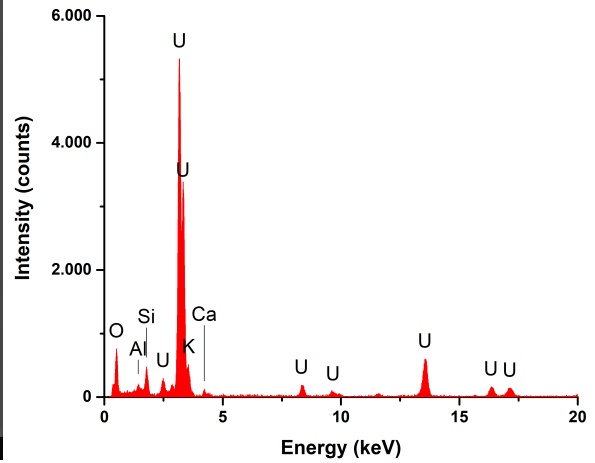
(b) EDS spectrum for BK-006

Fig. B.6   BK-006 (Mopsimilian) imaging and EDS analysis. The particle was found as part of an affiliated thesis[Hanemann 2019]
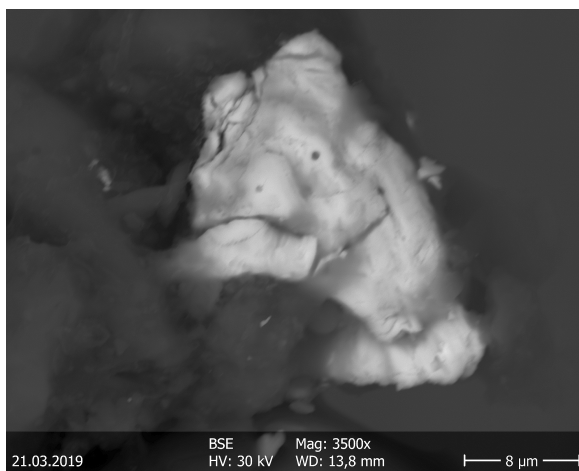
(a) SEM Image of BK-007 (BSE)
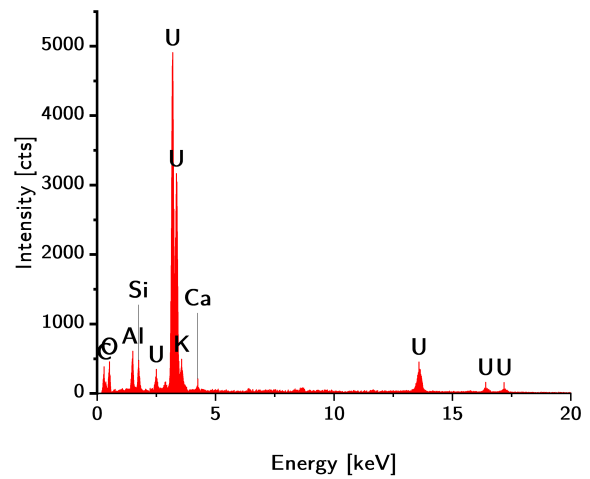
(b) EDS spectrum for BK-007

Fig. B.7   BK-007 (Lilith) imaging and EDS analysis. The particle was found as part of an affiliated thesis[Hanemann 2019]
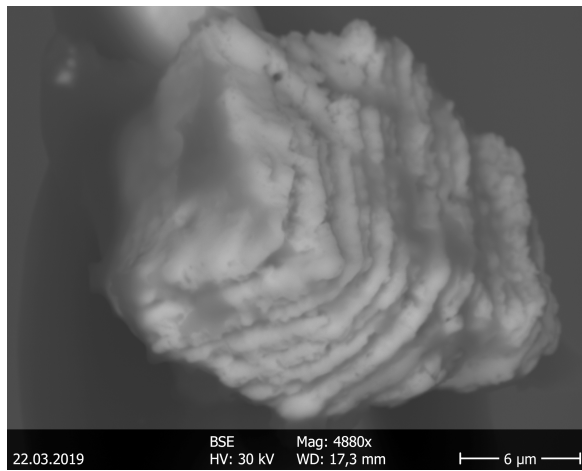
(a) SEM Image of BK-008 (BSE)
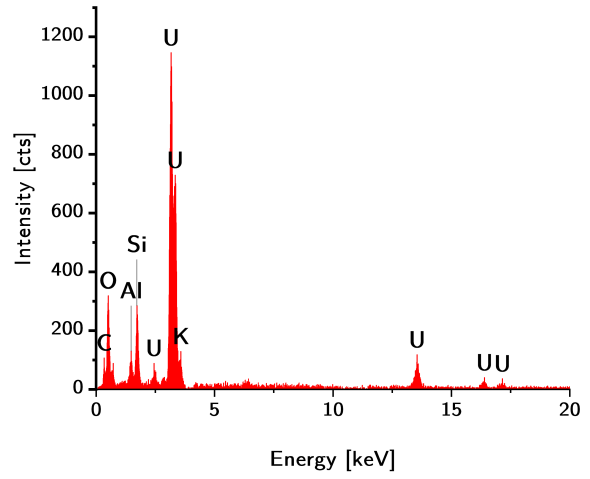
(b) EDS spectrum for BK-008

Fig. B.8 **BK-008 (Johanna) imaging and EDS analysis. The particle was found as part of an affiliated thesis**[Hanemann 2019]

# B.2 Cooling Pond (CP) Particles

(a) SEM Image of CP001 (BSE)

(b) EDS spectrum for CP001
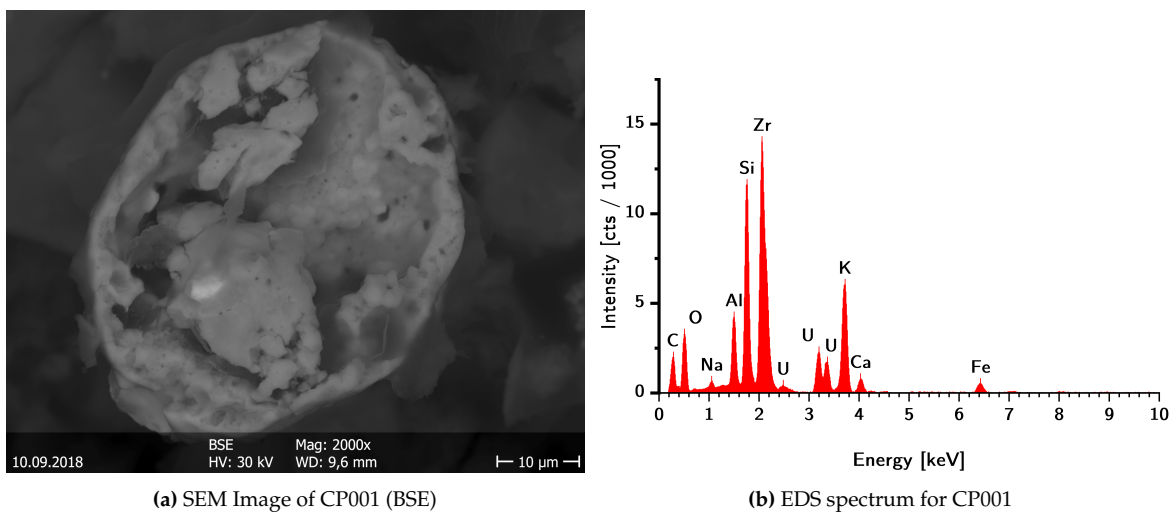
Fig. B.9   CP001 (Cate) imaging and EDS analysis

(a) SEM Image of CP-002 (BSE)

(b) EDS spectrum for CP-002
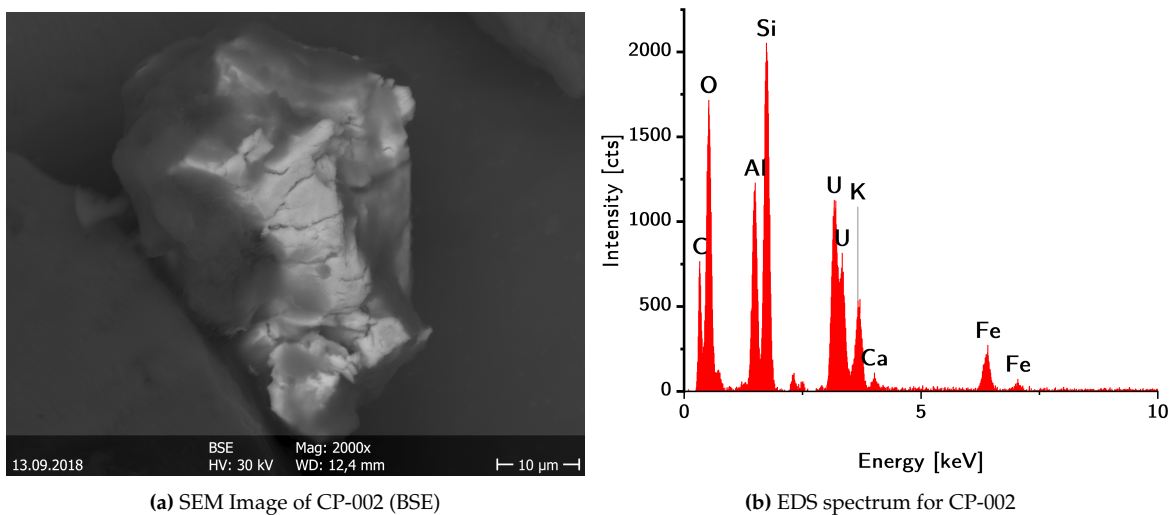
Fig. B.10   CP-002 (Dave) imaging and EDS analysis
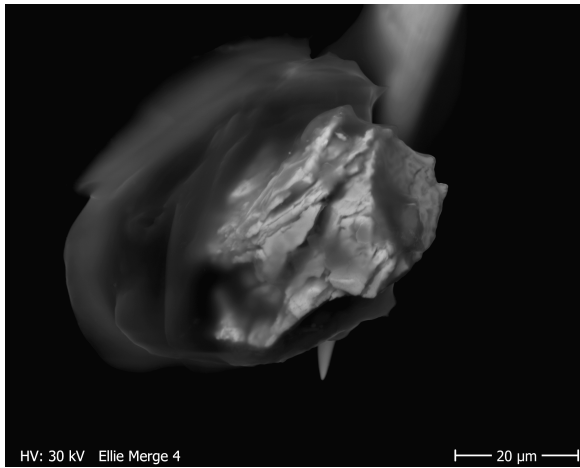
(a) SEM Image of CP-003 (SE+BSE overlay)
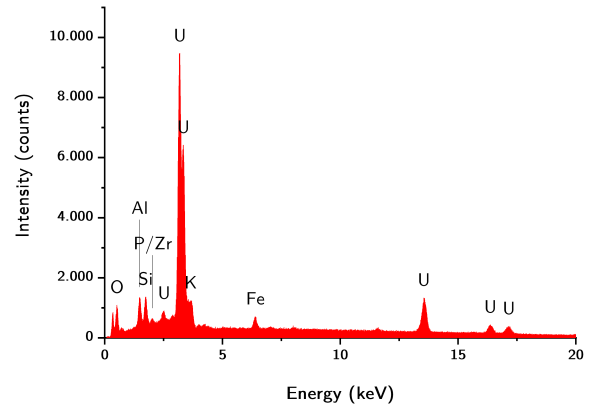
(b) EDS spectrum for CP-003

Fig. B.11 CP-003 (Ellie) imaging and EDS analysis
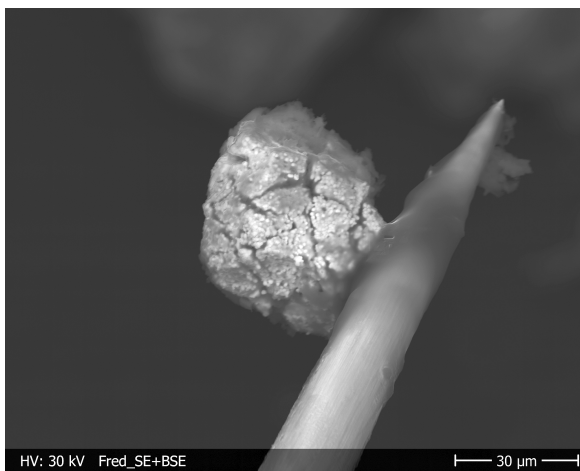
(a) SEM Image of CP-004 (SE+BSE overlay)
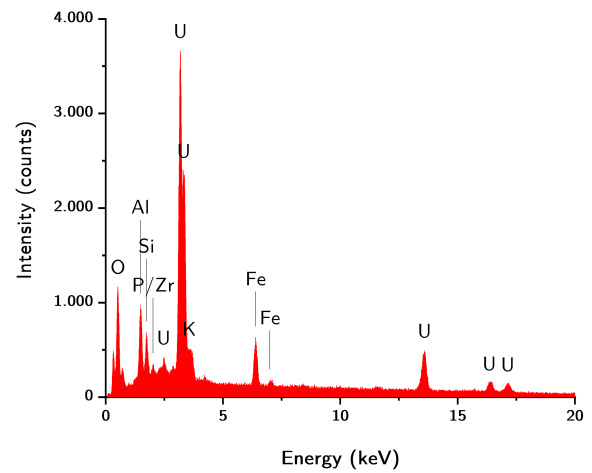
(b) EDS spectrum for CP-004

Fig. B.12 CP-004 (Fred) imaging and EDS analysis
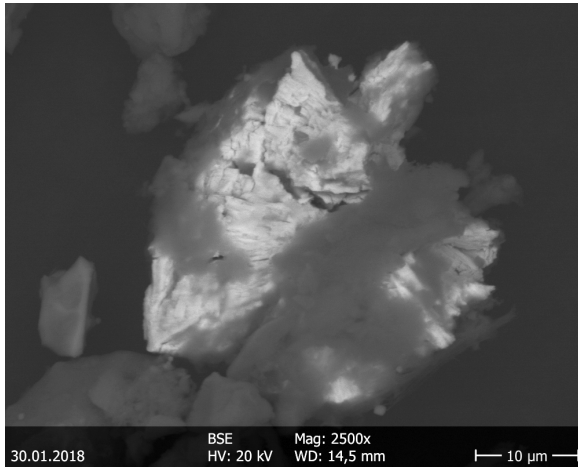
(a) SEM Image of CP-005 (BSE)
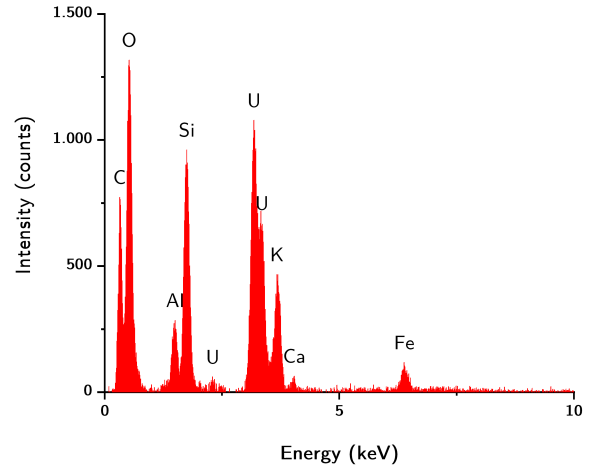
(b) EDS spectrum for CP-005

Fig. B.13   CP-005 (Georgia) imaging and EDS analysis
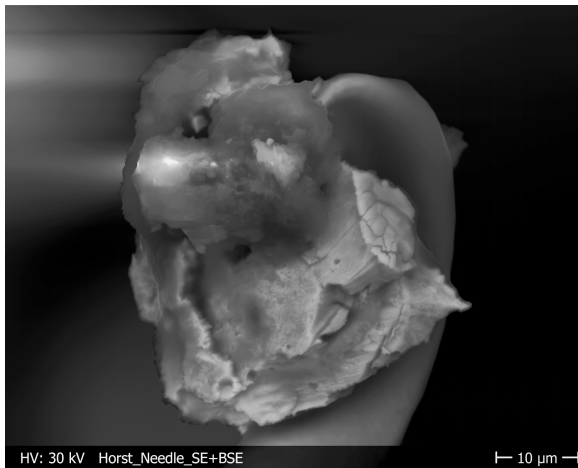
(a) SEM Image of CP-006 (SE+BSE overlay)
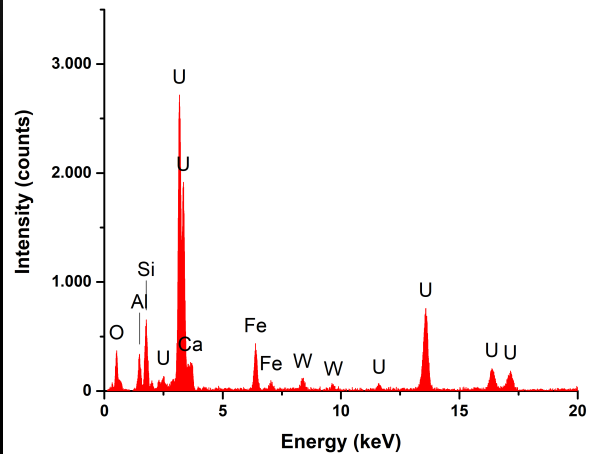
(b) EDS spectrum for CP-006

Fig. B.14   CP-006 (Horst) imaging and EDS analysis
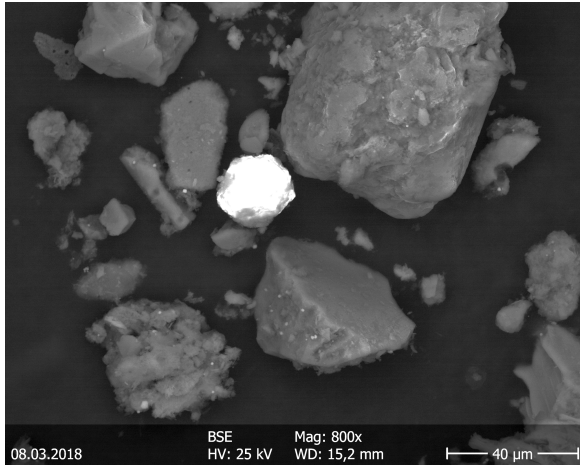
(a) SEM Image of CP-007 (BSE)
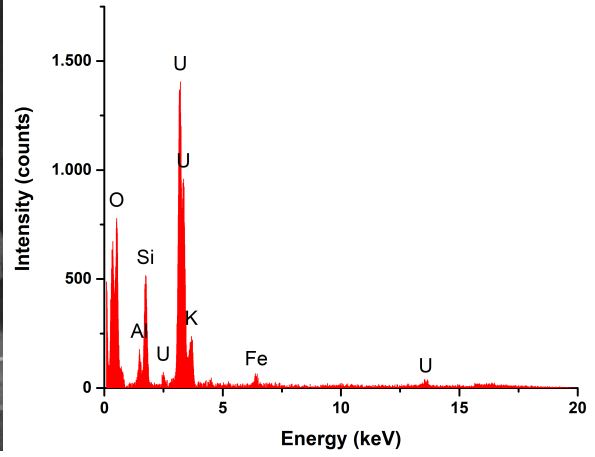
(b) EDS spectrum for CP-007

Fig. B.15 **CP-007 (Ida) imaging and EDS analysis**
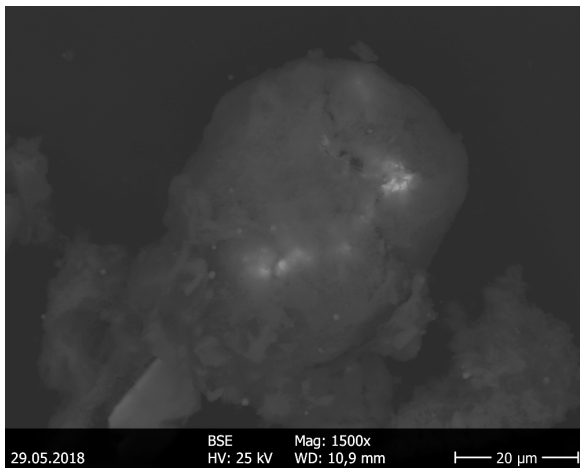
(a) SEM Image of CP-008 (BSE)
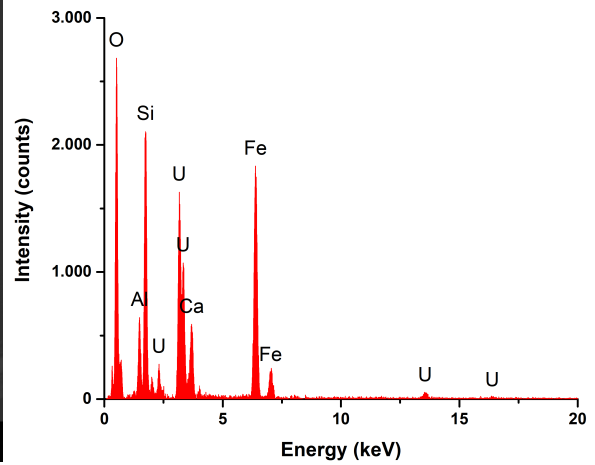
(b) EDS spectrum for CP-008

Fig. B.16 **CP-008 (James) imaging and EDS analysis**

(a) SEM Image of CP-009 (SE+BSE overlay)

(b) EDS spectrum for CP-009
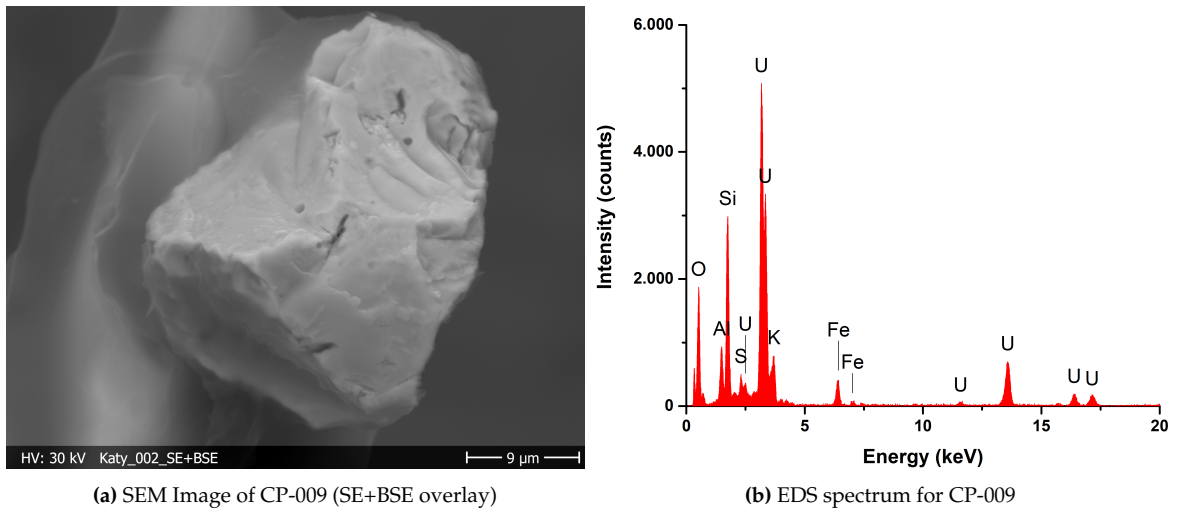
Fig. B.17 CP-009 (Katy) imaging and EDS analysis

(a) SEM Image of CP-010 (BSE)

(b) EDS spectrum for CP-010
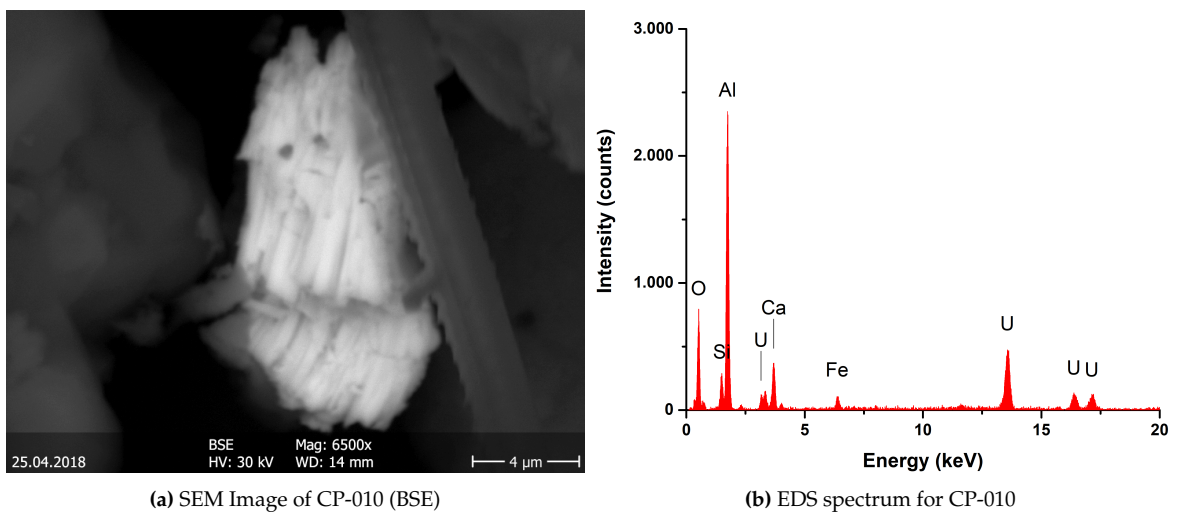
Fig. B.18 CP-010 (LittleGhost) imaging and EDS analysis. The particle was found as part of an affiliated thesis[Hanemann 2019]
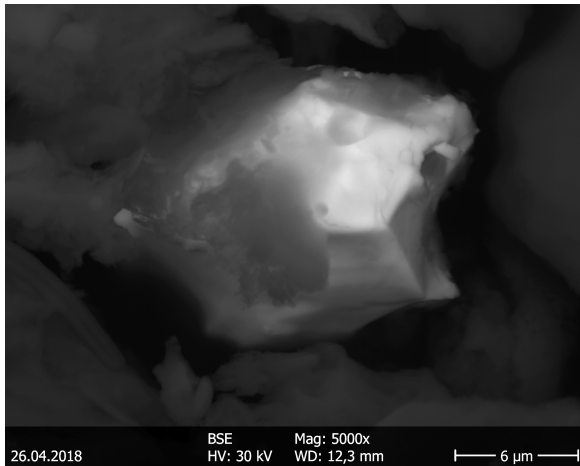
(a) SEM Image of CP-011 (BSE)
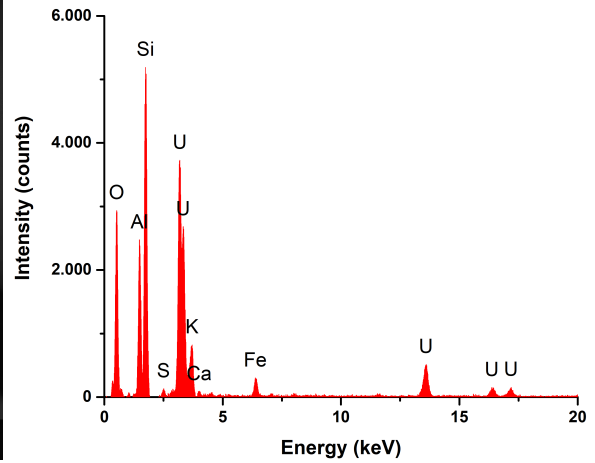
(b) EDS spectrum for CP-011

Fig. B.19   CP-011 (Mo) imaging and EDS analysis. The particle was found as part of an affiliated thesis[Leifermann 2018]
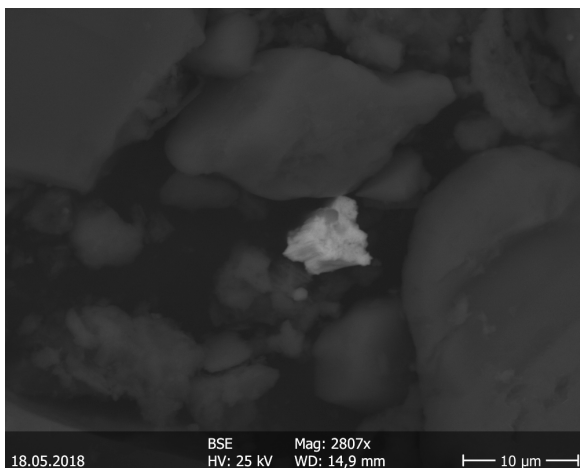
(a) SEM Image of CP-012 (BSE)
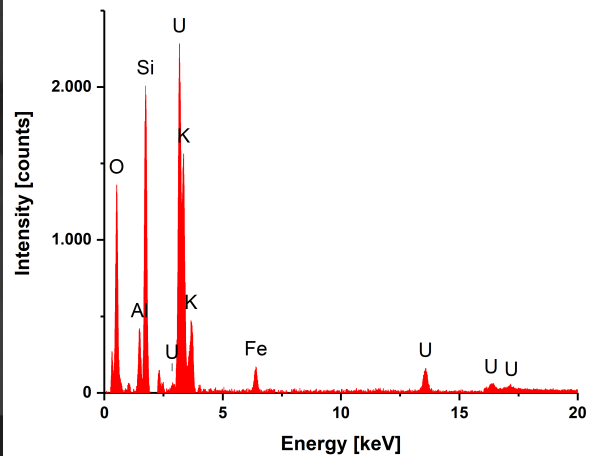
(b) EDS spectrum for CP-012

Fig. B.20   CP-012 (Quincy) imaging and EDS analysis. The particle was found as part of an affiliated thesis[Leifermann 2018]
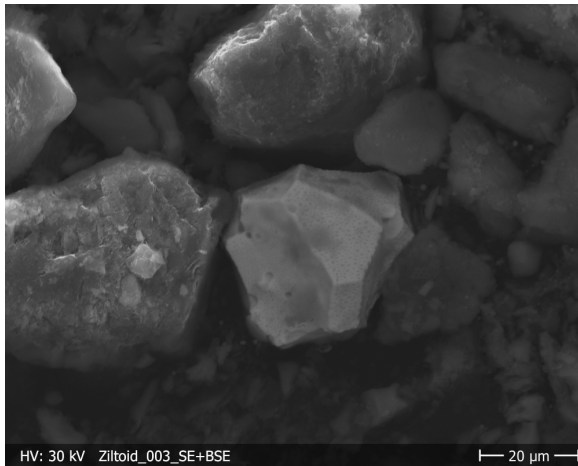
(a) SEM Image of CP-013 (SE+BSE overlay)
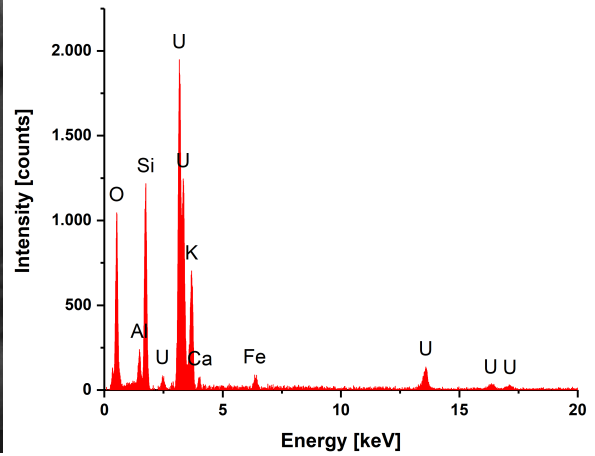
(b) EDS spectrum for CP-013

Fig. B.21   **CP-013 (Ziltoid) imaging and EDS analysis**
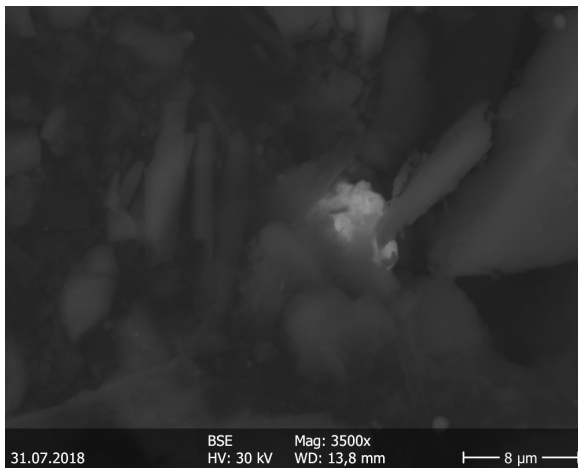
(a) SEM Image of CP-014 (BSE)
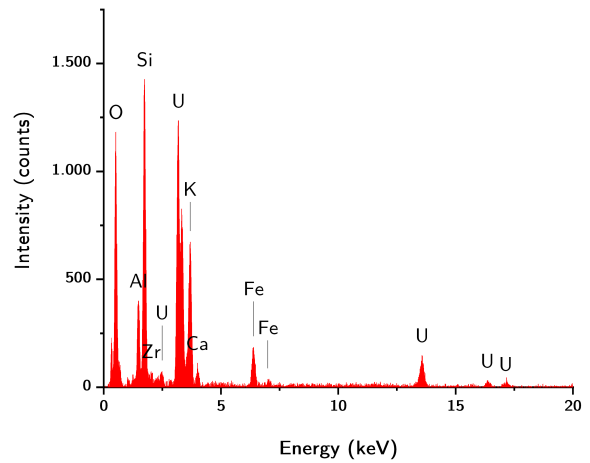
(b) EDS spectrum for CP-014

Fig. B.22   **CP-014 (Hauke) imaging and EDS analysis. The particle was found as part of an affiliated thesis**[Leifermann 2018]
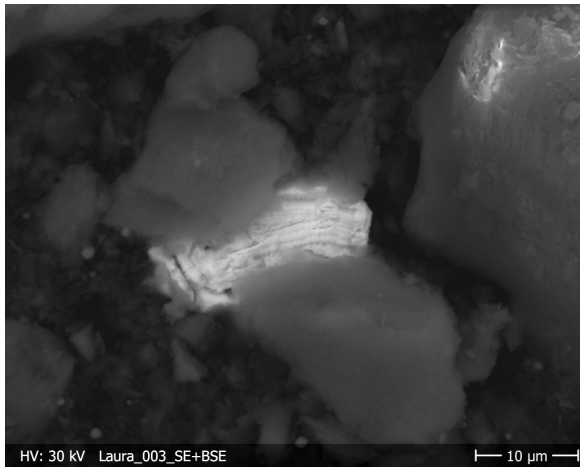
(a) SEM Image of CP-015 (SE+BSE overlay)
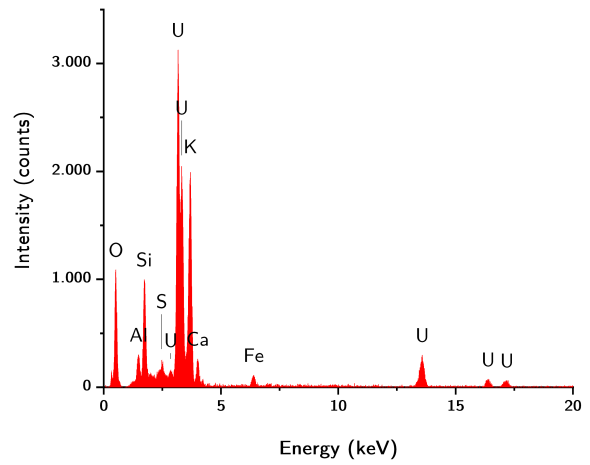
(b) EDS spectrum for CP-015

Fig. B.23 CP-015 (Laura) imaging and EDS analysis. The particle was found as part of an affiliated thesis[Leifermann 2018]
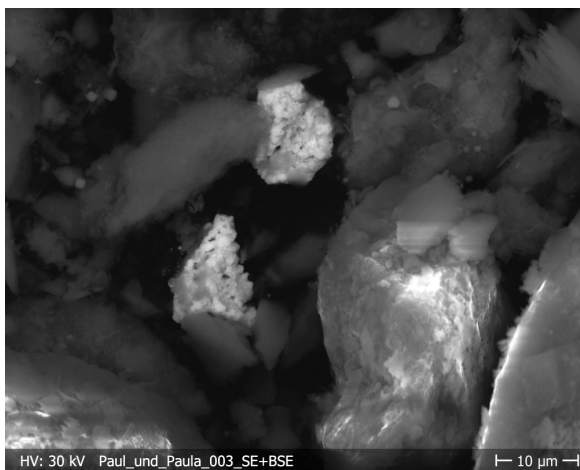
(a) SEM Image of CP-016 and CP-017 (SE+BSE overlay)
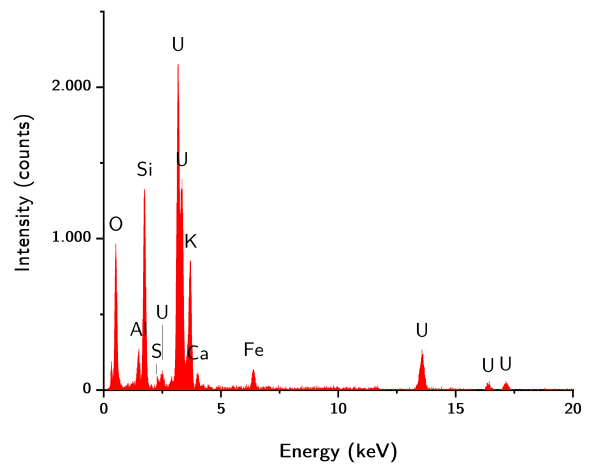
(b) EDS spectrum for CP-016 and CP-017

Fig. B.24 CP-016 (Paul) and CP-017 (Paula) imaging and EDS analysis. The particles were found as part of an affiliated thesis[Leifermann 2018]
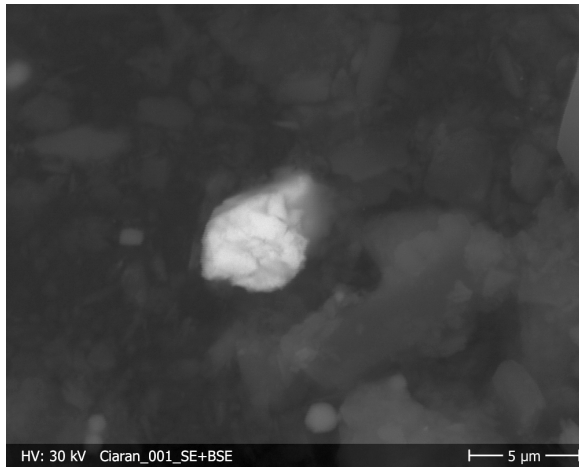
(a) SEM Image of CP-018 (SE+BSE overlay)
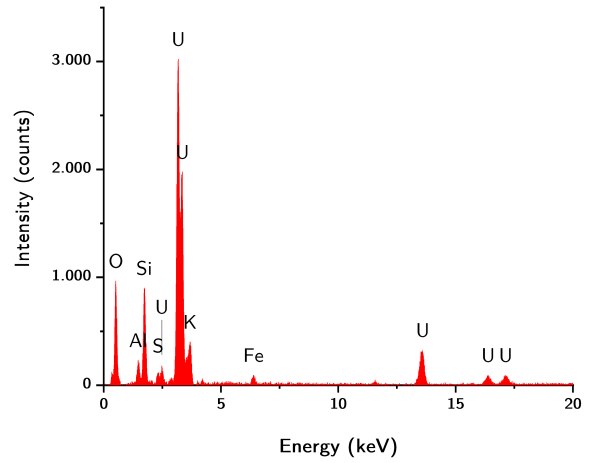
(b) EDS spectrum for CP-018

Fig. B.25   CP-018 (Ciaran) imaging and EDS analysis. The particle was found as part of an affiliated thesis[Leifermann 2018]

(a) SEM Image of CP-019 (SE+BSE overlay)
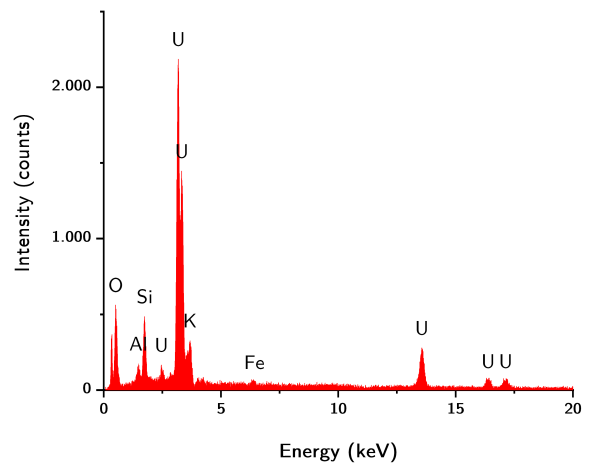
(b) EDS spectrum for CP-019

Fig. B.26   CP-019 (Balu) imaging and EDS analysis. The particle was found as part of an affiliated thesis[Leifermann 2018]
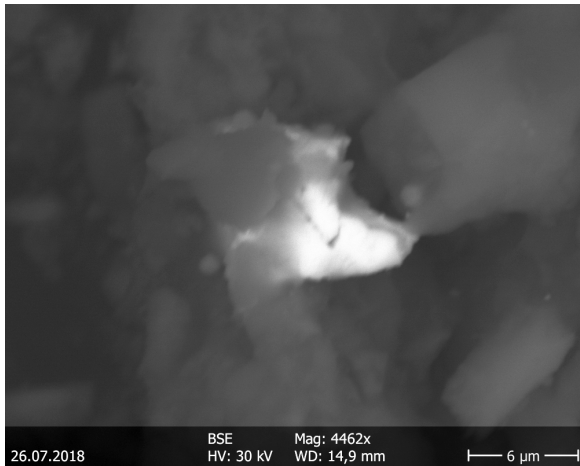
(a) SEM Image of CP-020 (BSE)
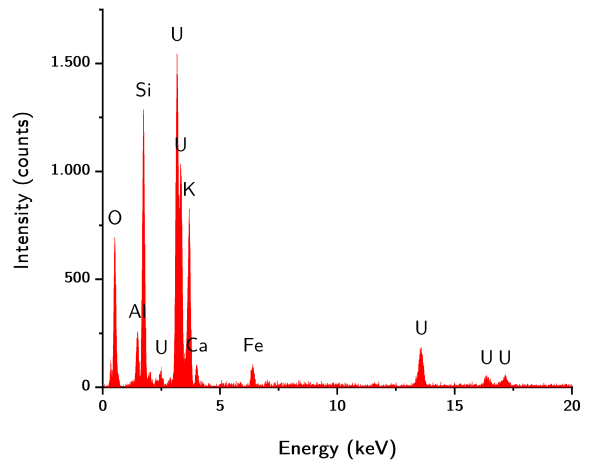
(b) EDS spectrum for CP-020

Fig. B.27 CP-020 (Siegnun) imaging and EDS analysis. The particle was found as part of an affiliated thesis[Leifermann 2018]
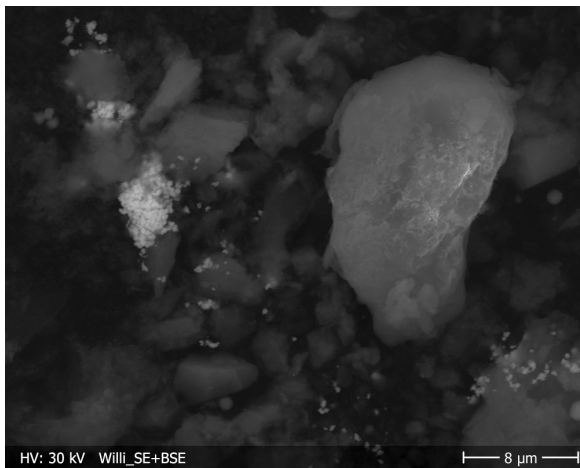
(a) SEM Image of CP-021 (SE+BSE overlay)
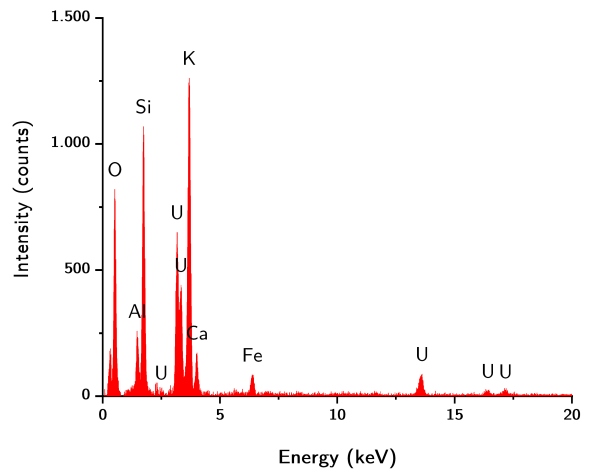
(b) EDS spectrum for CP-021

Fig. B.28 CP-021 (Willi) imaging and EDS analysis. The particle was found as part of an affiliated thesis[Leifermann 2018]
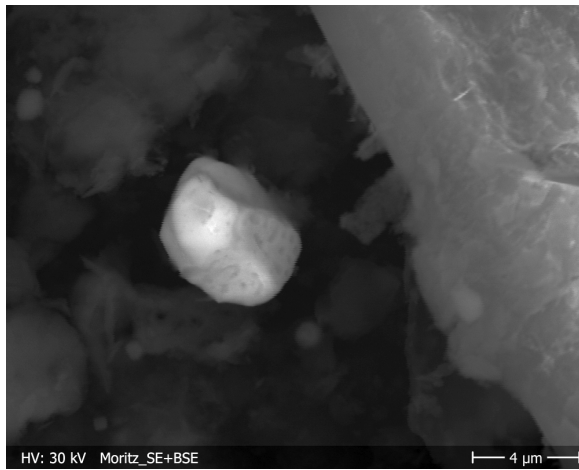
(a) SEM Image of CP-022 (SE+BSE overlay)
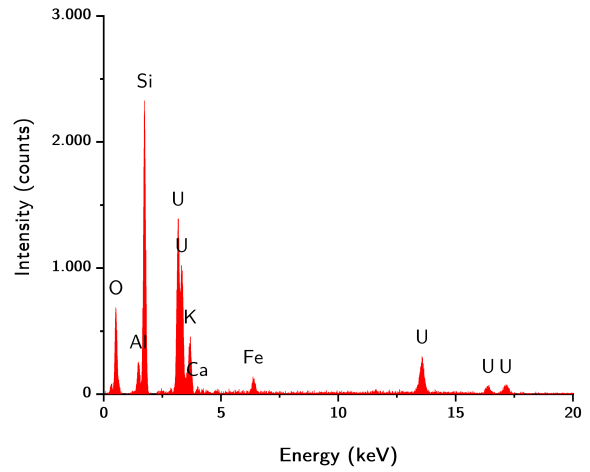
(b) EDS spectrum for CP-022

Fig. B.29 CP-022 (Moritz) imaging and EDS analysis. The particle was found as part of an affiliated thesis[Leifermann 2018]
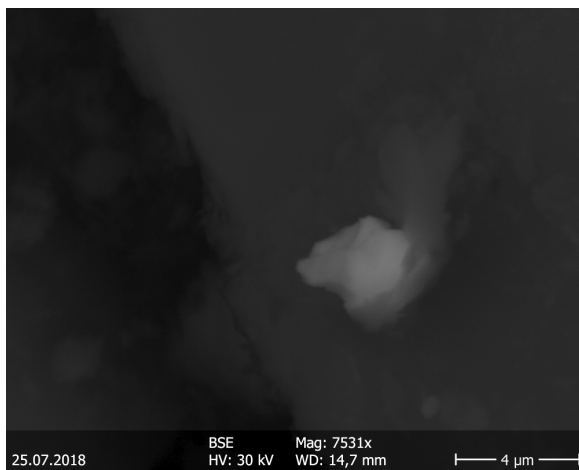
(a) SEM Image of CP-023 (BSE)
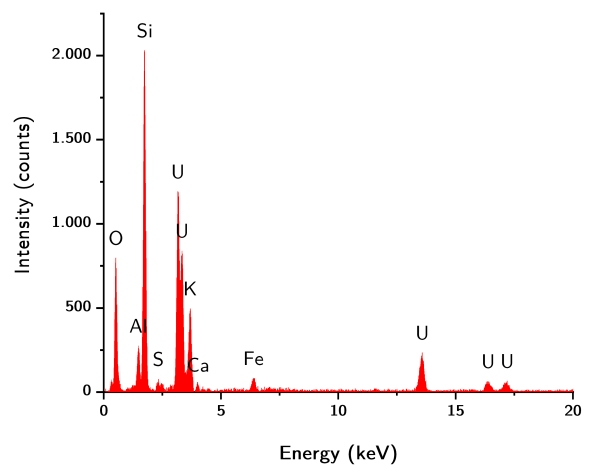
(b) EDS spectrum for CP-023

Fig. B.30 CP-023 (Lizzy) imaging and EDS analysis. The particle was found as part of an affiliated thesis[Leifermann 2018]
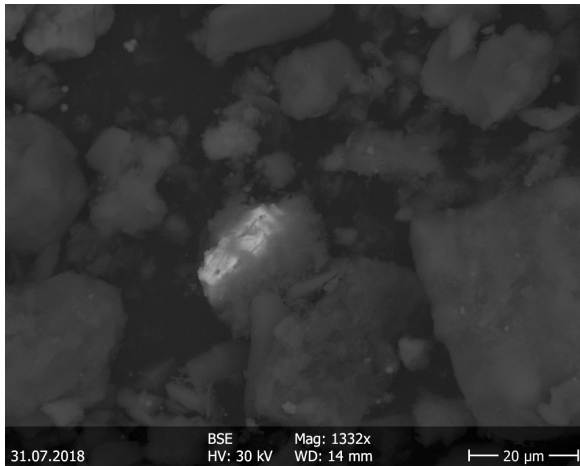
(a) SEM Image of CP-024 (BSE)
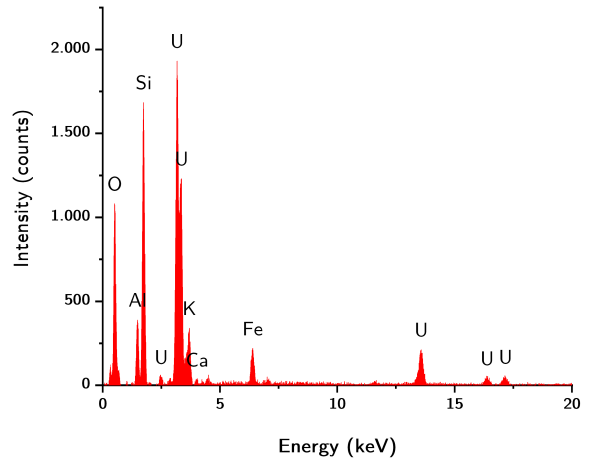
(b) EDS spectrum for CP-024

Fig. B.31   CP-024 (Rudi) imaging and EDS analysis. The particle was found as part of an affiliated thesis[Leifermann 2018]
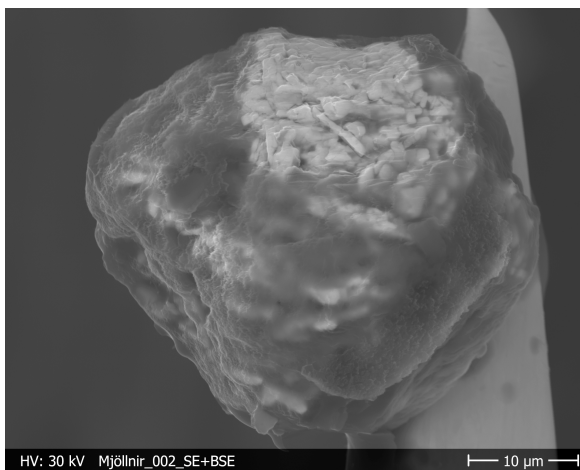
(a) SEM Image of CP-025 (SE+BSE overlay)
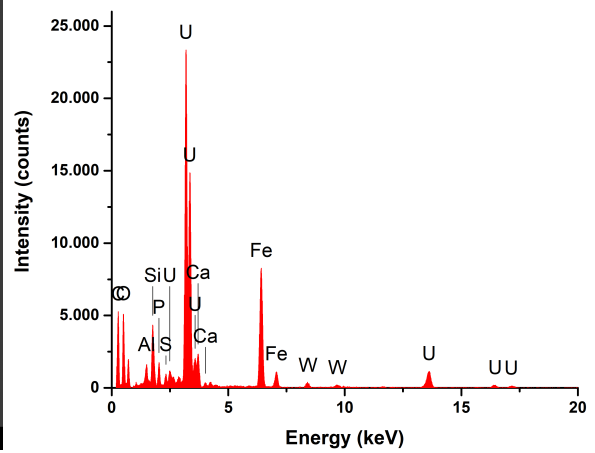
(b) EDS spectrum for CP-025

Fig. B.32   CP-025 (Mjoellnir) imaging and EDS analysis
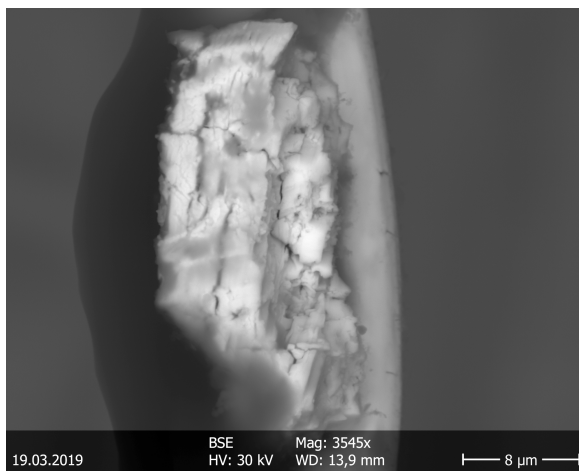
(a) SEM Image of CP-026 (BSE)

(b) EDS spectrum for CP-026

Fig. B.33 **CP-026 (Jörmungandr) imaging and EDS analysis.**

(a) SEM Image of CP-027 (SE+BSE overlay)
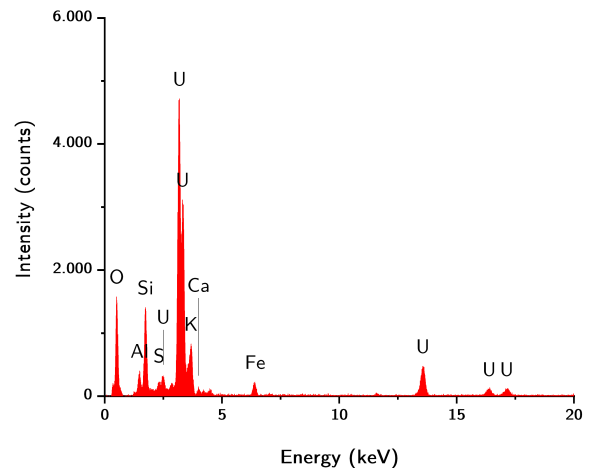
(b) EDS spectrum for CP-027

Fig. B.34 **CP-027 (Jakob) imaging and EDS analysis. The particle was found as part of an affiliated thesis**[Leifermann 2018]

B.3 Kopachi (KOP) Particles
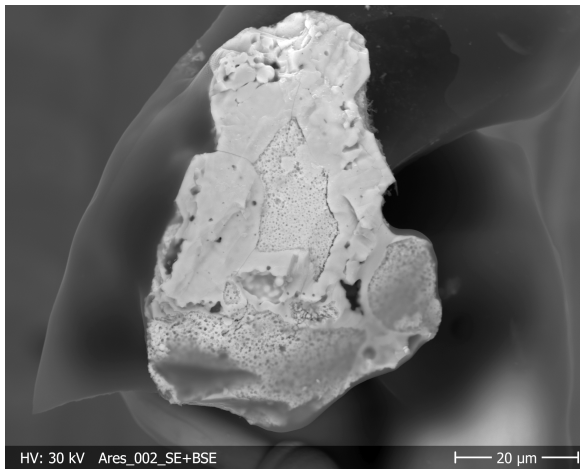
(a) SEM Image of KOP-001 (SE+BSE overlay)
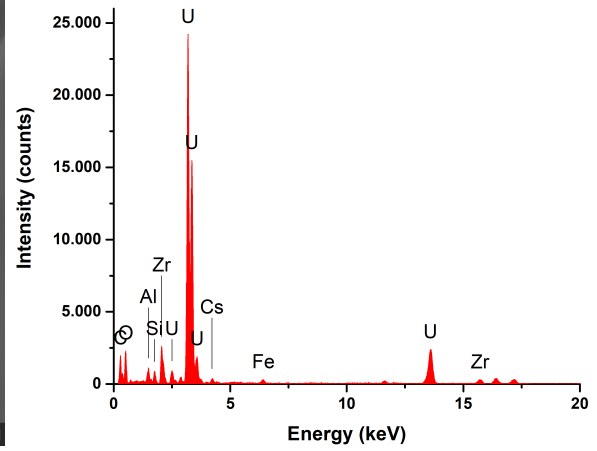
(b) EDS spectrum for KOP-001

Fig. B.35 KOP-001 (Ares) imaging and EDS analysis. The particle was also used within another thesis[Schulz 2020]
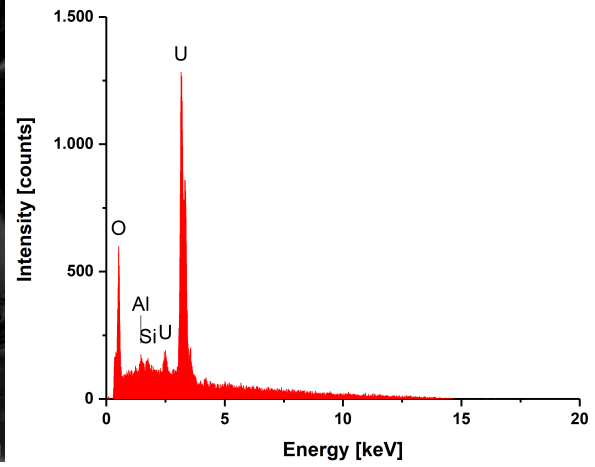

(a) SEM Image of KOP-002 (SE+BSE overlay)
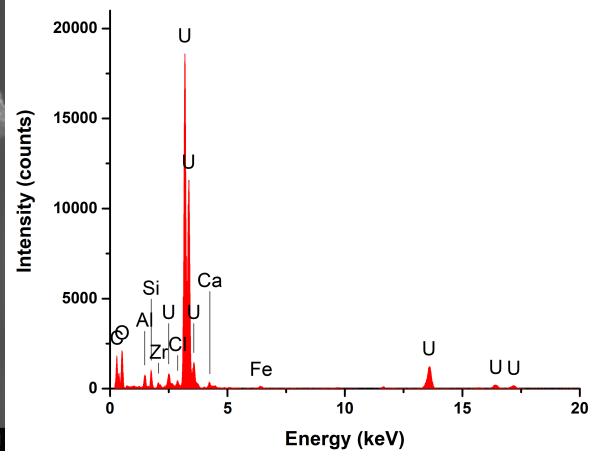
(b) EDS spectrum for KOP-002

Fig. B.36 KOP-002 (Bellerophon) imaging and EDS analysis. The particle was also used within another thesis[Schulz 2020]
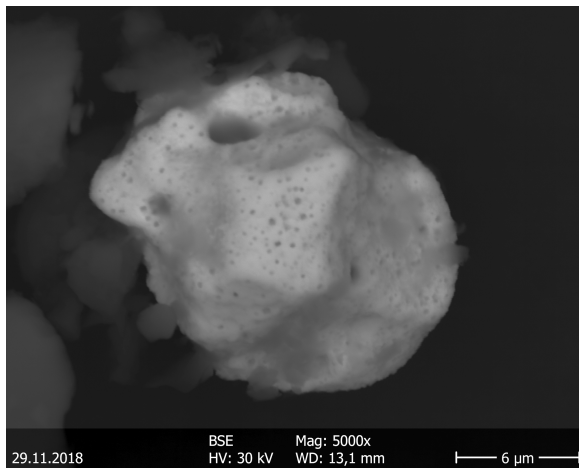
(a) SEM Image of KOP-003 (BSE)
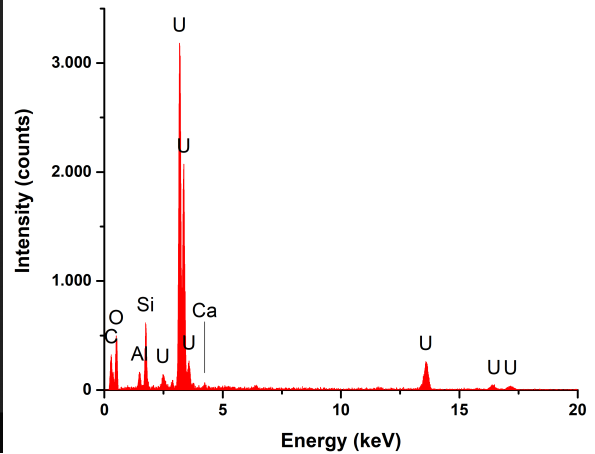
(b) EDS spectrum for KOP-003

Fig. B.37   KOP-003 (Chimaera) imaging and EDS analysis. The particle was also used within another thesis[Schulz 2020]
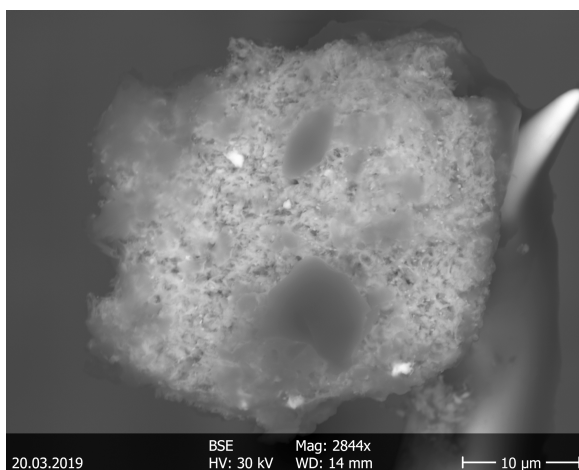
(a) SEM Image of KOP-004 (BSE)
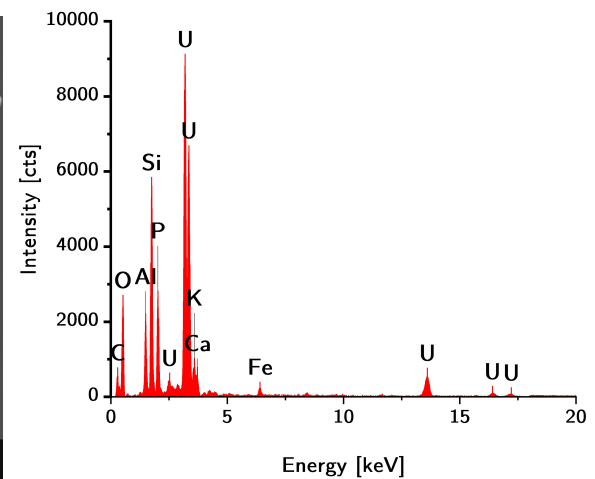
(b) EDS spectrum for KOP-004

Fig. B.38   KOP-004 (Dionysos) imaging and EDS analysis. The particle was also used within another thesis[Schulz 2020]
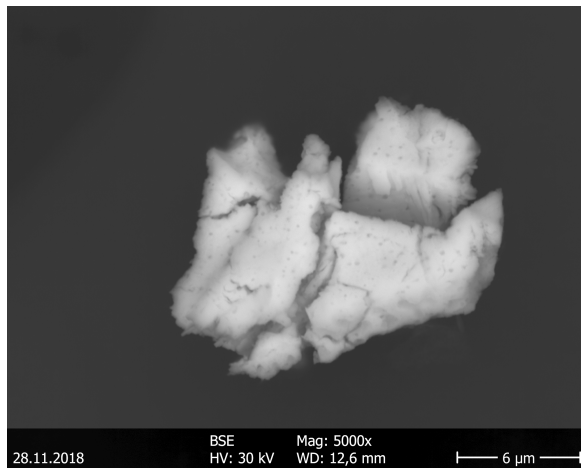
(a) SEM Image of KOP-005 (BSE)
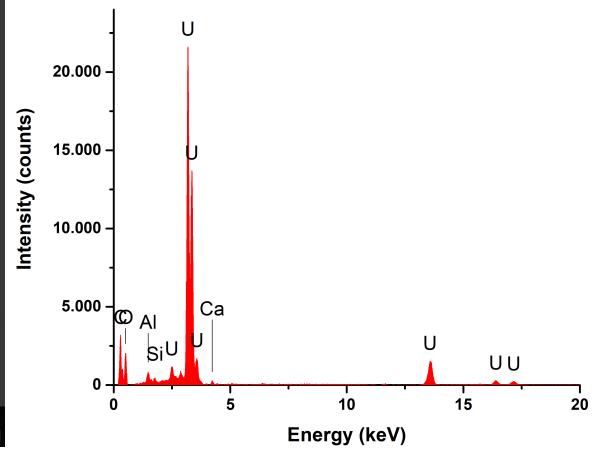
(b) EDS spectrum for KOP-005

Fig. B.39 KOP-005 (Eris) imaging and EDS analysis. The particle was also used within another thesis[Schulz 2020]
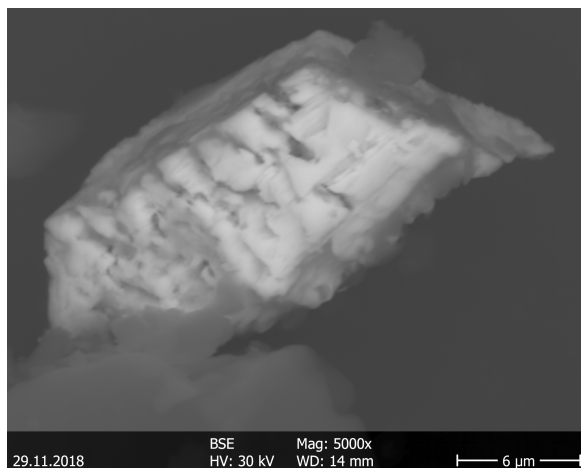
(a) SEM Image of KOP-006 (BSE)
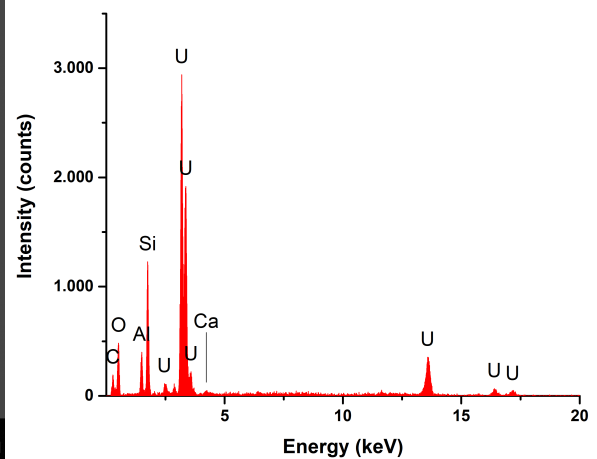
(b) EDS spectrum for KOP-006

Fig. B.40 KOP-006 (Faina) imaging and EDS analysis. The particle was also used within another thesis[Schulz 2020]
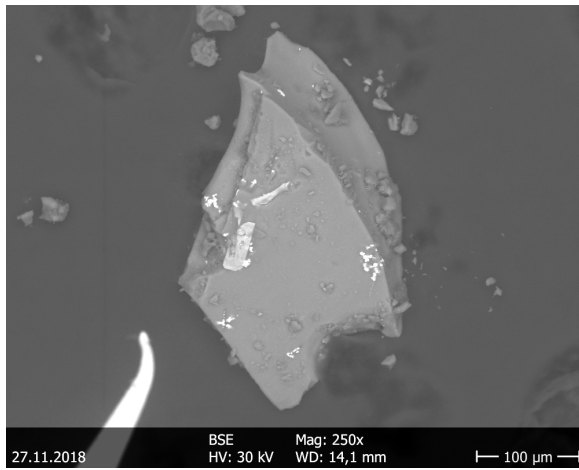
(a) SEM Image of KOP-007 (BSE)
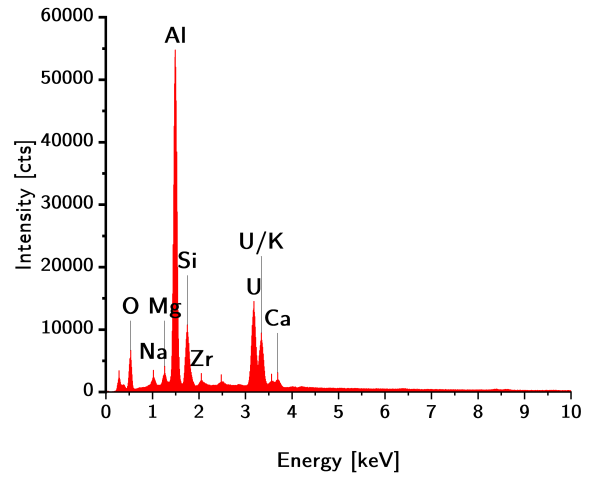
(b) EDS spectrum for KOP-007

Fig. B.41   KOP-007 (Gaia) imaging and EDS analysis. The particle was also used within another thesis[Schulz 2020]
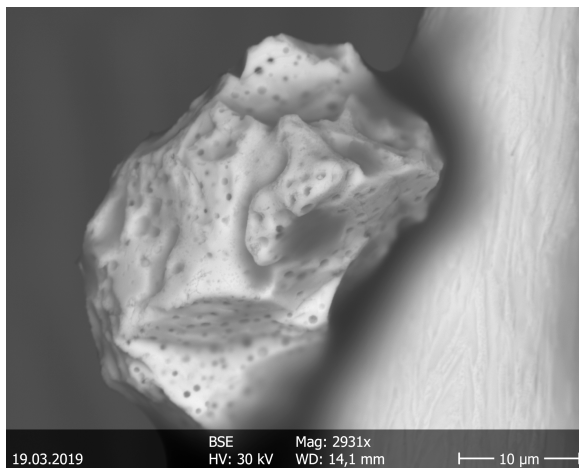
(a) SEM Image of KOP-008 (BSE)
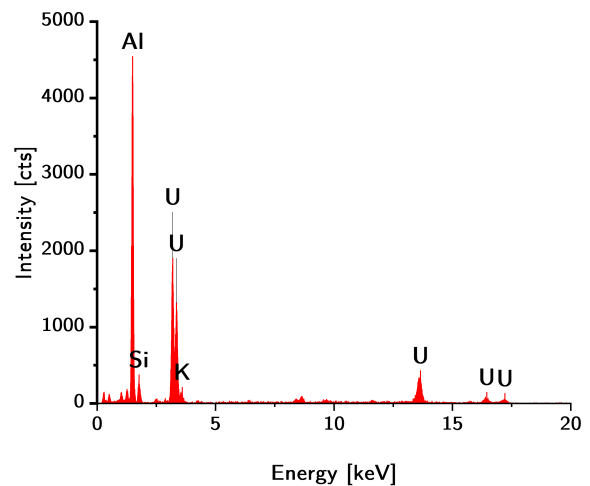
(b) EDS spectrum for KOP-008

Fig. B.42   KOP-008 (Herakles) imaging and EDS analysis. The particle was also used within another thesis[Schulz 2020]
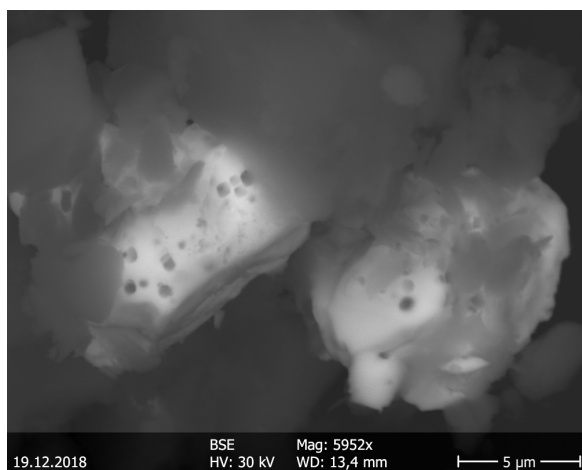
(a) SEM Image of KOP-009 (BSE)
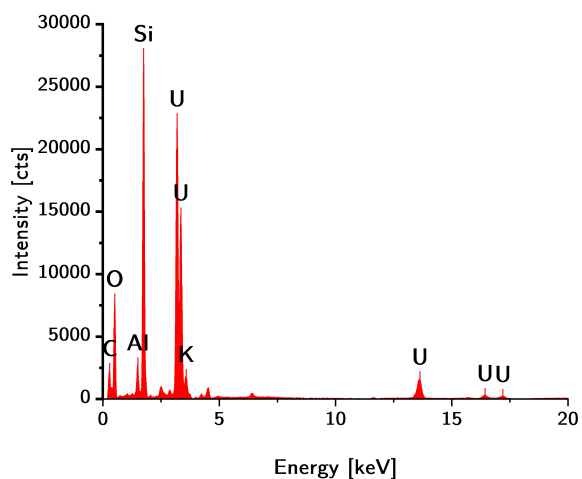
(b) EDS spectrum for KOP-009

Fig. B.43 KOP-009 (Iris) imaging and EDS analysis. The particle was also used within another thesis[Schulz 2020]
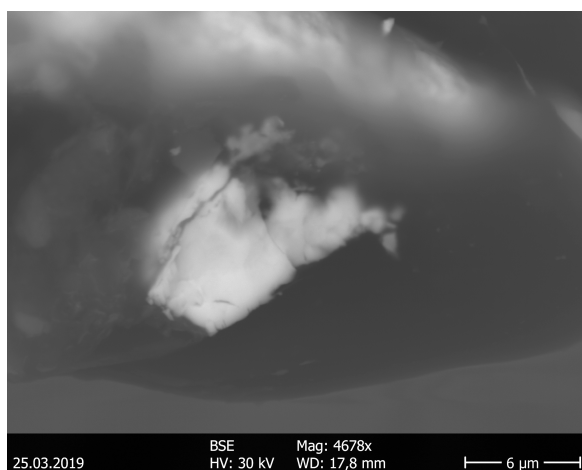
(a) SEM Image of KOP-00X (BSE)
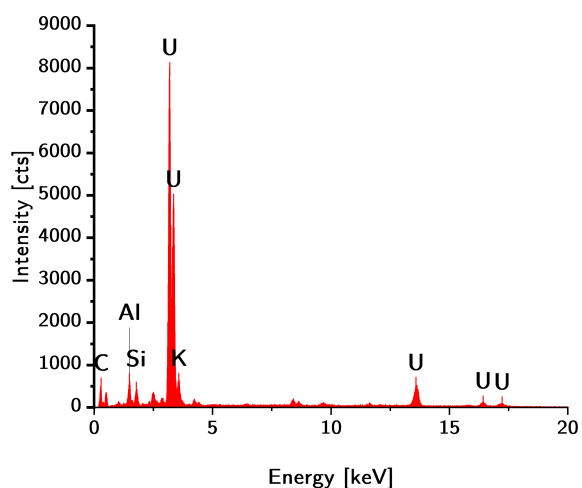
(b) EDS spectrum for KOP-00X

Fig. B.44 KOP-00X (Fragment) imaging and EDS analysis. The particle was also used within another thesis[Schulz 2020]
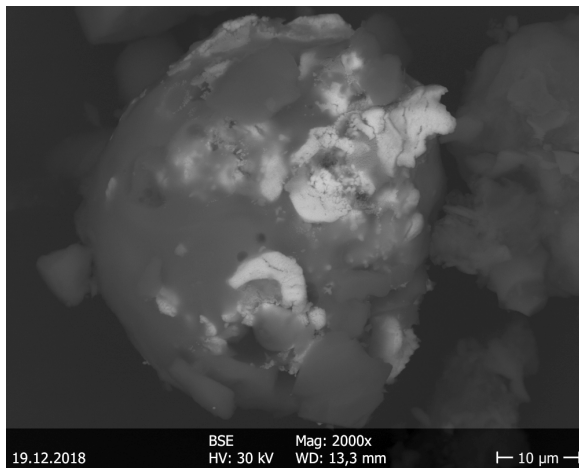
(a) SEM Image of KOP-010 (BSE)
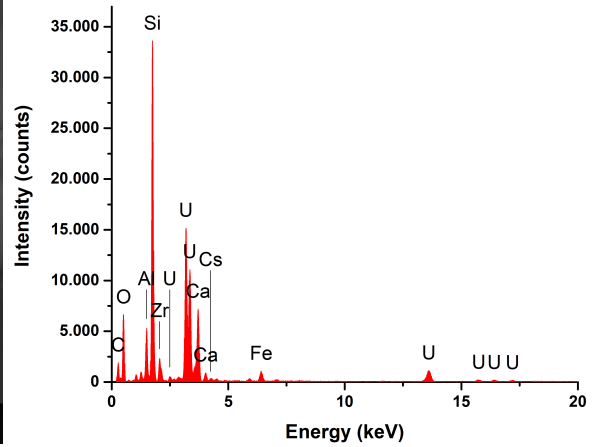
(b) EDS spectrum for KOP-010

Fig. B.45   KOP-010 (Japetos) imaging and EDS analysis. The particle was also used within another thesis[Schulz 2020]
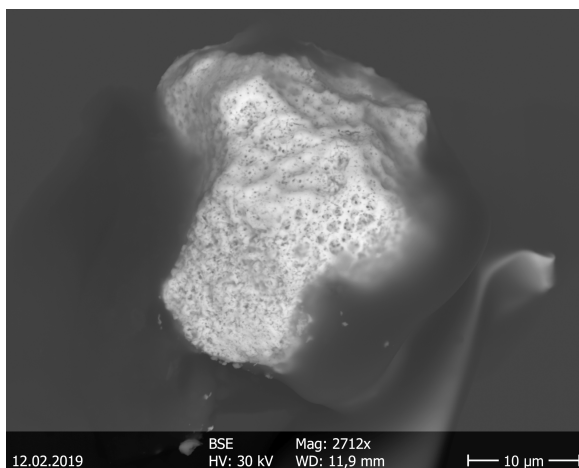
(a) SEM Image of KOP-011 (BSE)
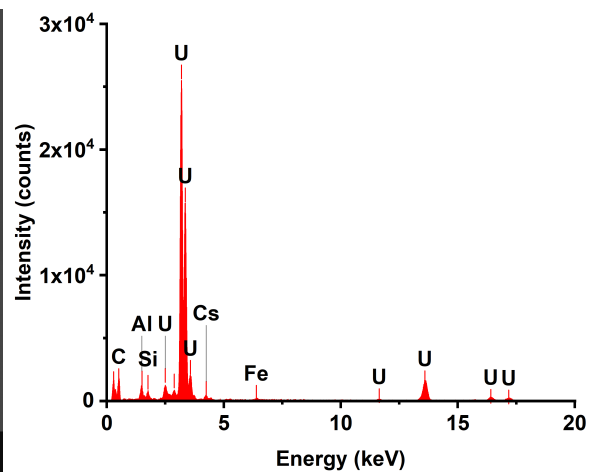
(b) EDS spectrum for KOP-011

Fig. B.46   KOP-011 (Kronos) imaging and EDS analysis. The particle was dissolved as part of this thesis

B.4 Red Forest (RW) Particles
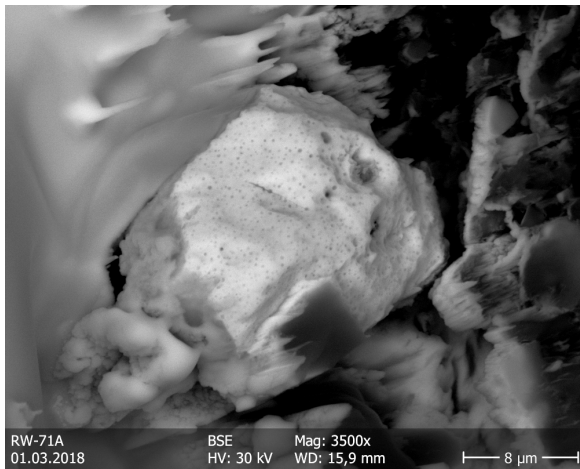
(a) SEM Image of RW-001 (BSE)

(b) EDS spectrum for RW-001

Fig. B.47   RW-001 (Bob) imaging and EDS analysis. The particle was found during another thesis[Hamann 2017] and used in further projects[Bosco 2020]
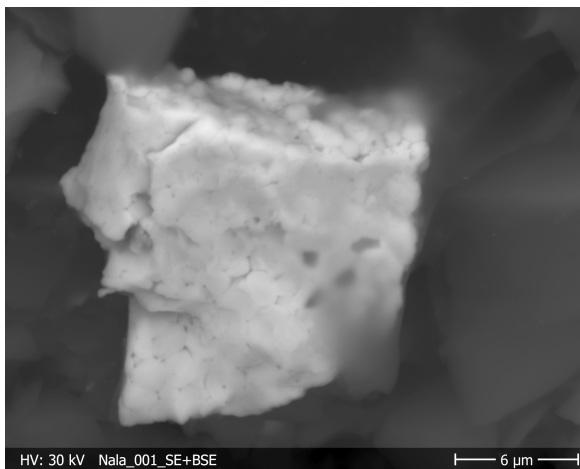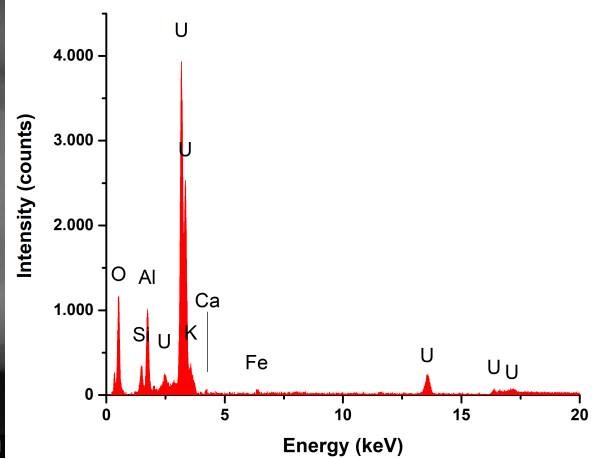

(a) SEM Image of RW-002 (SE+BSE overlay)
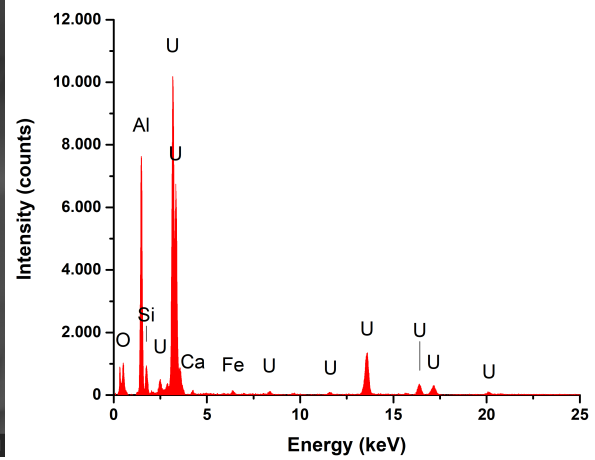
(b) EDS spectrum for RW-002

Fig. B.48   RW-002 (Nala) imaging and EDS analysis. The particle was found as part of an affiliated thesis[Leifermann 2018]
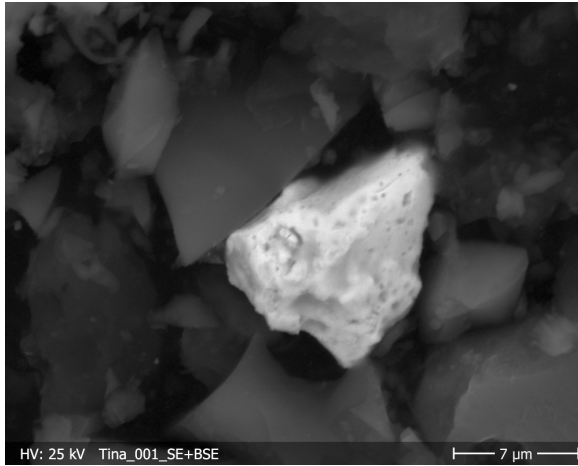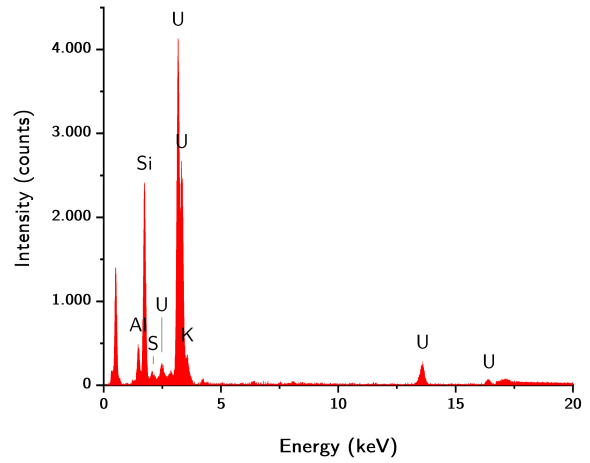
(a) SEM Image of RW-003 (SE+BSE overlay)
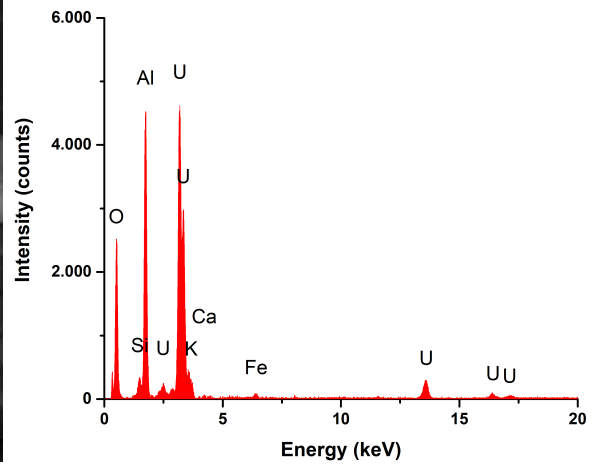
(b) EDS spectrum for RW-003

Fig. B.49 RW-003 (Olaf) imaging and EDS analysis. The particle was found as part of an affiliated thesis[Leifermann 2018]
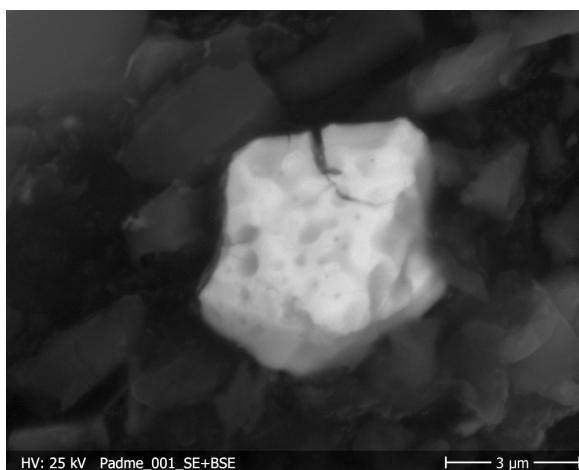
(a) SEM Image of RW-004 (SE+BSE overlay)
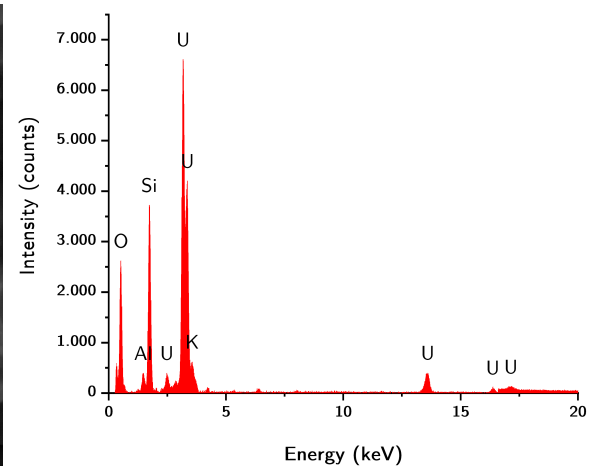
(b) EDS spectrum for RW-004

Fig. B.50 RW-004 (Padme) imaging and EDS analysis. The particle was found as part of an affiliated thesis[Leifermann 2018]
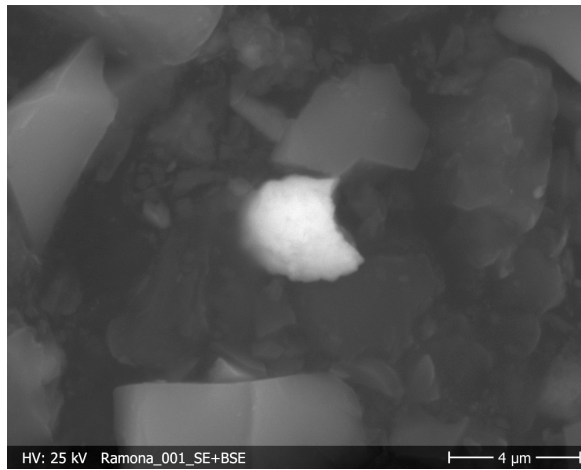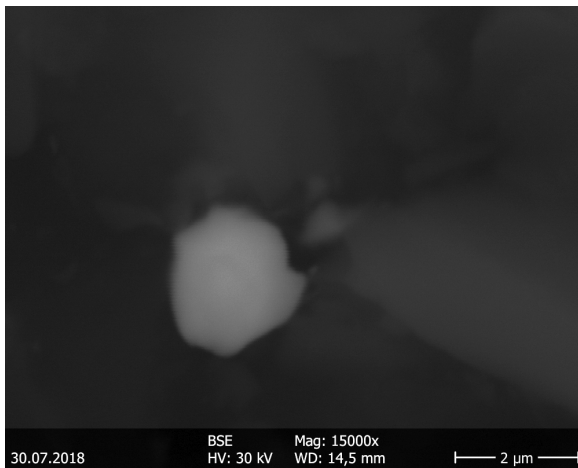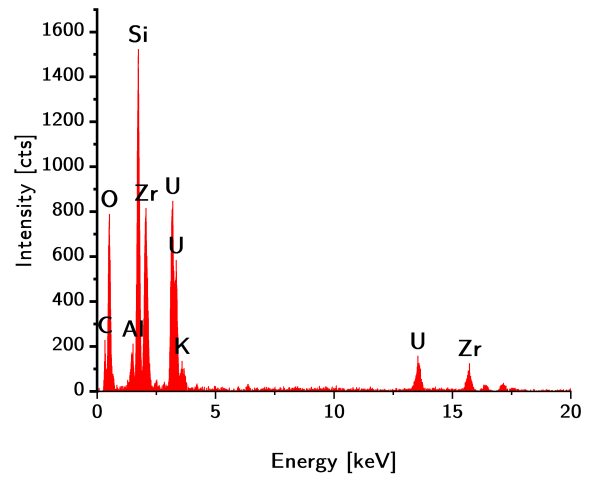
(a) SEM Image of RW-005 (SE+BSE overlay)
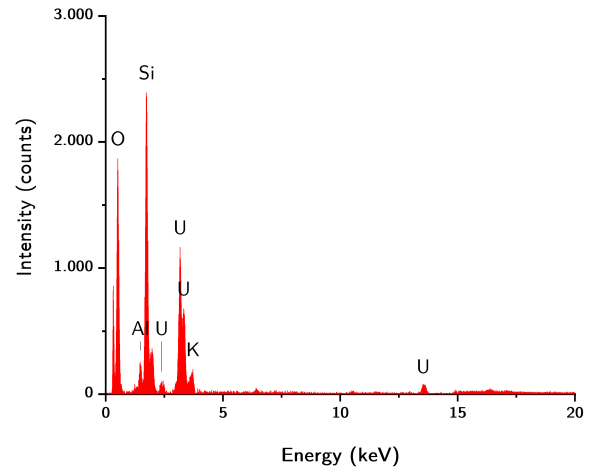
(b) EDS spectrum for RW-005

Fig. B.51 **RW-005 (Ramona) imaging and EDS analysis. The particle was found as part of an affiliated thesis**[Leifermann 2018]
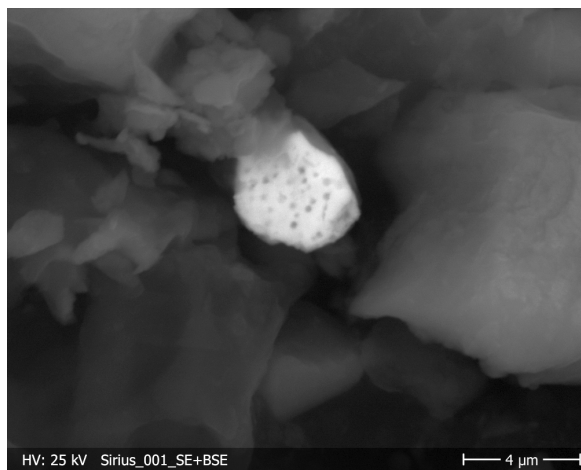
(a) SEM Image of RW-006 (SE+BSE overlay)

(b) EDS spectrum for RW-006

Fig. B.52 **RW-006 (Sirius) imaging and EDS analysis. The particle was found as part of an affiliated thesis**[Leifermann 2018]

(a) SEM Image of RW-007 (SE+BSE overlay)

(b) EDS spectrum for RW-007

Fig. B.53 RW-007 (Tina) imaging and EDS analysis. The particle was found as part of an affiliated thesis[Leifermann 2018]
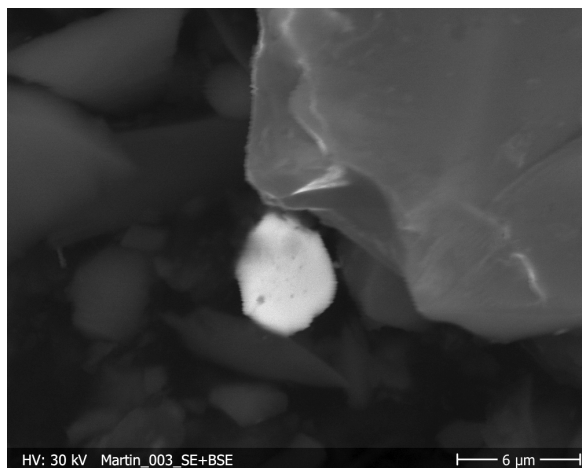

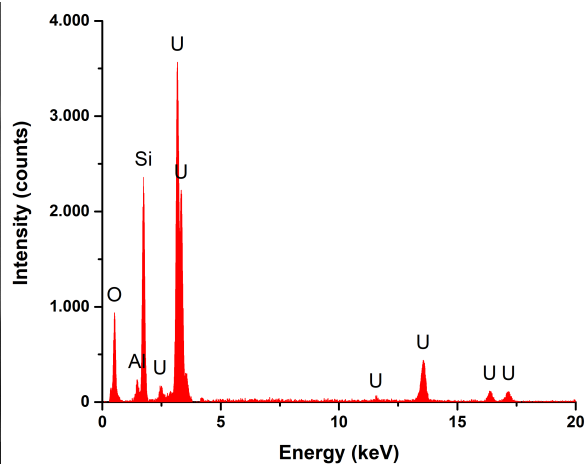**(a)** SEM Image of RW-008 (BSE)

(b) EDS spectrum for RW-008

Fig. B.54 RW-008 (Manuel) imaging and EDS analysis. The particle was found as part of an affiliated thesis[Leifermann 2018]
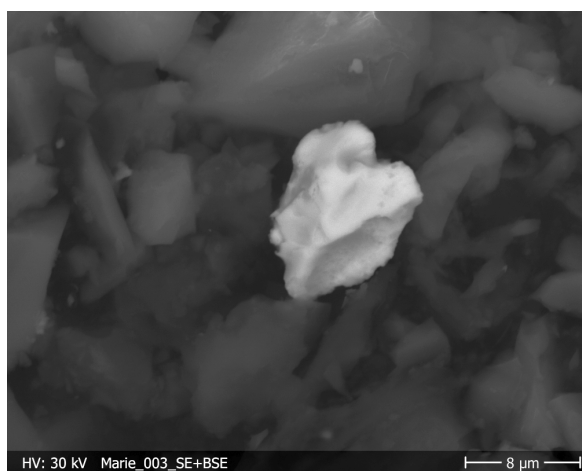
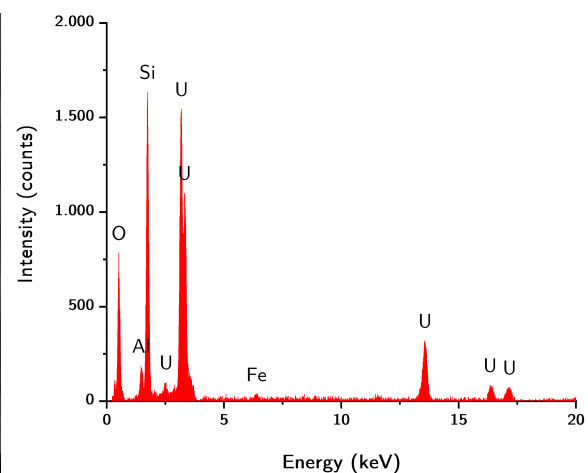**(a)** SEM Image of RW-009 (SE+BSE overlay)

(b) EDS spectrum for RW-009

Fig. B.55   RW-009 (Martin) imaging and EDS analysis. The particle was found as part of an affiliated thesis[Leifermann 2018]
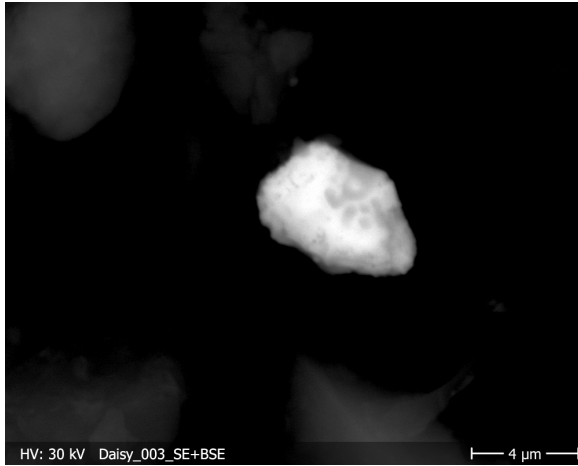

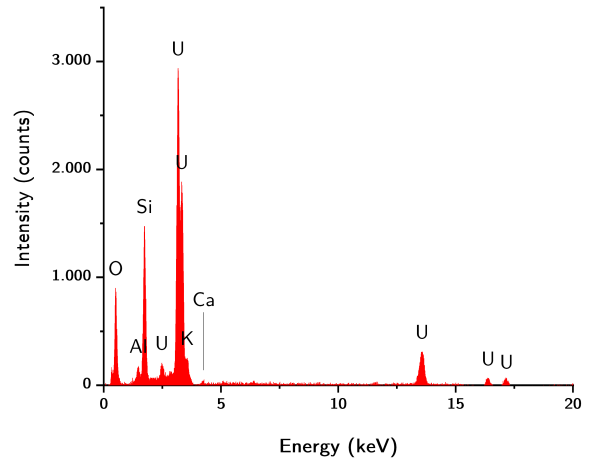**(a)** SEM Image of RW-010 (SE+BSE overlay)

(b) EDS spectrum for RW-010

Fig. B.56   RW-010 (Marie) imaging and EDS analysis. The particle was found as part of an affiliated thesis[Leifermann 2018]
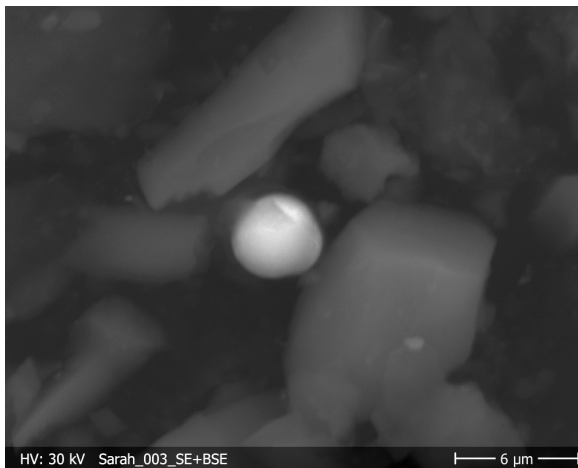
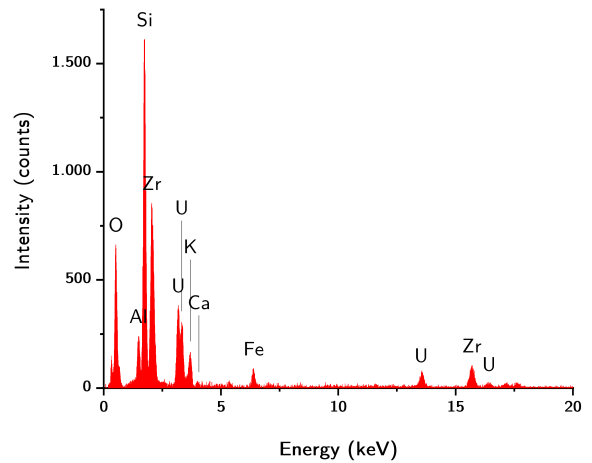**(a)** SEM Image of RW-011 (SE+BSE overlay)

(b) EDS spectrum for RW-011

Fig. B.57 RW-011 (Daisy) imaging and EDS analysis. The particle was found as part of an affiliated thesis[Leifermann 2018]

(a) SEM Image of RW-012 (SE+BSE overlay)

(b) EDS spectrum for RW-012

Fig. B.58 RW-012 (Sarah) imaging and EDS analysis. The particle was found as part of an affiliated thesis[Leifermann 2018]

B.5 Curriculum Vitae

Martin Weiß

Experience

02/2021 – today	**Project Manager**
	BGE Bundesgesellschaft für Endlagerung mbH, Peine
05/2016 – 09/2020	**Research Assistant**
	IRS, Leibniz University, Hanover
03/2013 – 09/2013	**Product Developer**
	Evonik Litarion AG, Marl
02/2009 – 09/2009	**Chemical Labworker**
	Bayer Schering Pharma AG, Bergkamen

Education

05/2016 – today	**PhD Candidate, Physics**
	IRS, Leibniz University, Hanover
	Thesis: *Extraction and Analysis of Nuclear Fuel Fragments from the Chernobyl Exclusion Zone*
10/2013 – 11/2015	**M. Sc. Analytical Chemistry**
	Leibniz University, Hanover
	Thesis: *Fabrication, Physical and Chemical Characterization of Multifunctional InorganicNanoparticles for Ultraviolet Light Filtration*
10/2009 – 02/2013	**B. Sc. Chemistry**
	Leibniz University, Hanover
09/2006 – 01/2009	**Chemical Labworker, professional training**
	Bayer Schering Pharma AG, Bergkamen
09/1997 – 06/2006	**Abitur**
	Städtisches Gymnasium, Bergkamen

B.6 List of publications

- Bosco, H.; Hamann, L.; Kneip, N.; Raiwa, M.; Weiss, M.; Wendt, K.; Walther, C. (2021). "New horizons in microparticle forensics: Actinide imaging and detection of 238 Pu and ^{242m}Am in hot particles". In: *Science Advances* 7, (44)

- Bosco, H.; Weiss, M.; Raiwa, M.; Walther, C.; Kneip, N.; Wendt, K. (2020). "Influence of the hyperfine structure on plutonium in resonant laser-SNMS". In: *Hyperfine Interactions* 241, (34)

- Lang, A.; Engelberg, D.; Walther, C.; Weiss, M.; Bosco, H.; Jenkins, A. Livens, F.; Law, G. (2019). "Cesium and Strontium Contamination of Nuclear Plant Stainless Steel: Implications for Decommissioning and Waste Minimization". In: *ACS Omega* 4, 11, pp. 14 420 – 14 429

- Lang, A.; Engelberg, D.; Smith, N.T.; Trivedi, D.; Horsfall, O.; Banford, A.; Martin, P. A.; Coffey, P.; Bower, W. R.; Walther, C.; Weiß, M.; Bosco, H.; Jenkins, A.; Law, G. T. W. (2018). "Analysis of contaminated nuclear plant steel by laser-induced breakdown spectroscopy". In: *Journal of Hazardous Materials* 345, pp. 114 — 122

- Cardillo, D.; Weiss, M.; Tehei, M.; Devers, T.; Rosenfeld, A.; Konstantinov, K. (2016). "Multifunctional Fe_2O_3/CeO_2 nanocomposites for free radical scavenging ultraviolet protection". In: *RSC Advances* 6, pp. 65 397 – 65 402

- Juestel, M.; Schwinger, A.; Weiss, M.; Binnewies, M. (2011). "Preparation of $LiFePO_4$ by Nozzle-Spray-Pyrolysis". In: *ECS Transactions* 33, (21)